DESIGNING REAL-TIME DIAGNOSTICS FOR SQUIRREL CAGE INDUCTION MOTORS

Anik Kumar Samanta

DESIGNING REAL-TIME DIAGNOSTICS FOR SQUIRREL CAGE INDUCTION MOTORS

Thesis submitted to
Indian Institute of Technology, Kharagpur
for the award of the degree

of

Master of Science (by Research)

by

Anik Kumar Samanta

under the guidance of

Professor Aurobinda Routray

ADVANCED TECHNOLOGY DEVELOPMENT CENTRE
INDIAN INSTITUTE OF TECHNOLOGY, KHARAGPUR
March 2016

CERTIFICATE OF APPROVAL

Certified that the thesis entitled **Designing Real-time Diagnostics for Squirrel Cage Induction Motors**, submitted by **Anik Kumar Samanta** to the Indian Institute of Technology, Kharagpur, for the award of the degree of Master of Science (by Research) has been accepted by the external examiners and that the student has successfully defended the thesis in the viva-voce examination held today.

Signature:
Name:
(Member of the DAC)

Signature:
Name:
(Member of the DAC)

Signature:
Name:
(Member of the DAC)

Signature:
Name:
(Supervisor)

Signature:
Name:
(External Examiner)

Signature:
Name:
(Chairman)

Advanced Technology Development Centre
Indian Institute of Technology, Kharagpur
Kharagpur, India 721302.

Certificate

This is to certify that this thesis entitled **Designing Real-time Diagnostics for Squirrel Cage Induction Motors** submitted by **Anik Kumar Samanta**, to the Indian Institute of Technology, Kharagpur, is a record of bona fide research work carried out under my supervision and is worthy of consideration for award of the degree of Master of Science (by Research) of the Institute.

Aurobinda Routray
Professor
Department of Electrical Engineering
Indian Institute of Technology, Kharagpur
India 721302.

I.I.T. Kharagpur
Date:

...in the loving memory of

Dida and Dadubhai for their love and inspiration

Declaration

I certify that

a. the work contained in the thesis is original and has been done by me under the guidance of my supervisors;

b. the work has not been submitted to any other institute for any other degree or diploma;

c. I have followed the guidelines provided by the Institute in preparing the thesis;

d. I have conformed to ethical norms and guidelines while writing the thesis;

e. whenever I have used materials (data, models, figures and text) from other sources, I have given due credit to them by citing them in the text of the thesis, and giving their details in the references, and taken permission from the copyright owners of the sources, whenever necessary.

Anik Kumar Samanta

Acknowledgment

This thesis marks the end of a long and eventful journey during which there were many people whom I would like to acknowledge for their encouragement and support. I am grateful to my supervisor, Prof. Aurobinda Routray, for giving me the opportunity to work under his supervision and also for his constant support throughout the research work. His advice and constructive criticism have helped the thesis take its present shape. I would like to thank the RDSO, Indian Railways, Lucknow for sponsoring the research work.

I would like to thank the members of the Department Academic Committee, Prof. P.K. Dutta, Prof. A. K. Deb, and Prof. Anoop C. S. for their suggestions and comments during the presentations and throughout the tenure of the work. I am thankful to the Head, Advanced Technology Development Centre, Head, Centre for Railway Research, and Head, Dept. of Electrical Engineering, IIT Kharagpur, for providing me the facilities to carry out my research work. I am grateful to Mr. Devasish Basu at CRR for the valuable time he spent for the discussions whose value to me is infinite.

It was a great opportunity for me to work with my co-researchers, Mr. Arunava Naha, and Mr. Ayan Mukherjee. I am grateful to them for their continuous inspiration and valuable suggestions. I would like to thank Arnab Biswas, Priyanka Priyadarsini Swain, Rajat Khetan, Soumya Ranjan Mohanty and V.S.S Aniket, for their effort. I would like to convey my heart-felt appreciation to Mr. Amiya Das Adhikari, and Mr. Prosenjit for their technical support for developing and packaging of the onboard system.

I would like to appreciate the help and support of all my colleagues of CRR Lab and RTES Lab. My special thanks to Anushree, Procheta, Soumi, Aritra, Arvind, Avik, Bibek, Ramnarayan, Sudipto, and Tanmoy, who inspired me in research and made my stay in the campus enjoyable and memorable. I am indebted to my school friends Abhijeet, Abhinandan, Ases, Anirban, Tamojit, and Preetam for their love, support and appreciation.

My deepest gratitude goes to my parents and other members of my family for their unflagging love, and support throughout my life. This thesis would not have been possible without their sacrifices, love, and support.

Abstract

Fail-safe operation of Squirrel Cage Induction Motor (SCIM) is crucial for many industries ranging from rolling mills, thermal power plants to railway locomotives. Faults in induction motor can manifest in different forms, hampering the normal functioning of the locomotive incurring behemoth losses. Predicting these defects at an early stage can drastically enhance the operation efficiency. This type of condition based predictive maintenance can result in lesser downtime and improved reliability.

In this thesis, an online condition monitoring system is developed to detect incipient induction motor faults, with particular emphasis on railway locomotives as the major application area. However, the diagnoser can be used for any SCIM. Spectral analysis of the stator current is central to the fault detection algorithm. The acquired current signal is preconditioned by removing the high-amplitude fundamental component using Extended Kalman Filter (EKF) and a second order signal model. Pre-conditioning of the input signal improves the detectability of the low amplitude fault frequency component under adverse loading conditions. An elegant Rayleigh quotient-based spectral estimator is designed specifically to detect and quantify weak SCIM faults. The accuracy of the proposed estimator was found to be comprehensive when compared with Fourier analyses and Multiple Signal Classifier (MUSIC) with its time complexity lower than MUSIC. Accurate relative-amplitude estimation capability and low complexity make this estimator appropriate for embedded applications. The slip and the supply frequency are found non-invasively from the stator current for forming adaptive fault frequency search bands required for the spectral estimation. Spectral estimation over small multiple bands reduced the computational burden extensively. A relation between the peak magnitude of the spectrum and the amplitude of constituent sinusoids is utilized to quantify the fault severity. As all the algorithms require only the single phase stator current, the reliability is increased, and the complexity and the cost of using additional sensors is reduced. This thesis primarily deals with detection of rotor faults of SCIMs like Broken End Ring (BER), Broken Rotor Bar (BRB), and Eccentricity (ECC) faults. Evaluation of threshold and detectability of faults under different conditions of load and fault severity are carried out with Empirical Cumulative Distribution Function (ECDF). The condition monitoring system has been tested in a lab

setup of 22 kW induction motor. It is found that BRB can be detected with a false alarm rate of 3% corresponding to a missed detection of 20%. ECC was detected with 3% missed detection without any false alarms. To test the fault detection algorithm with conditions that are difficult to emulate on the experimental motor, a Real-Time (RT) SCIM fault simulator is also developed. This simulator is mathematically based on the Coupled Circuit Model (CCM). Both the fault detector and the simulator are implemented on the hardware using Simulink Real-Time (SLRT) from Mathworks.

Keywords: Autocorrelation matrix, Broken rotor bar, Broken end ring, Closely spaced sinusoids, Couple Circuit Modeling, Extended Kalman filter, Eccentricity, Fault Detector, MCSA, MUSIC, Online Implementation, Rayleigh-quotient, Simulink Real-Time, Squirrel Cage Induction Motor

Contents

List of Abbreviations

AC	Alternating Current
ANN	Artificial Neural Network
BER	Broken End Ring
BIOS	Basic Input/Output System
BRB	Broken Rotor Bar
CCM	Coupled Circuit Modeling
CF	Central Frequency
DC	Direct Current
DFT	Discrete Fourier Transform
DOA	Direction of Arrival
DOS	Disk Operating System
DQ	Direct Quadrature
DSP	Digital Signal Processor
DTFT	Discrete Time Fourier Transform
ECDF	Empirical Cumulative Distribution Function
EKF	Extended Kalman Filter
ESPRIT	Estimation of Signal Parameters via Rotational Invariance Techniques
FEM	Finite Element Modeling
FFT	Fast Fourier Transform
FMM-CART	Fuzzy Min Max with Classification and Regression Tree
f_o	Fundamental Frequency
Fs	Sampling Frequency
IM	Induction Motor
IO	Input Output
L	Autocorrelation Matrix Size
MCSA	Motor Current Signature Analysis
MMF	Magneto Motive Force
MUSIC	Multiple Signal Classification
NI	National Instruments

PCI	Peripheral Component Interface
POR	Probability of Resolution
PSD	Power Spectral Density
RAM	Random Access Memory
RT	Real-Time
SCIM	Squirrel Cage Induction Motor
SLRT	SIMULINK Realtime
TM	Traction Motor
TSFEM	Time Step Finite Element Model
UMP	Unbalanced Magnetic Pull
USB	Universal Serial Bus
VFD	Variable Frequency Drive
w.r.t	with respect to

List of Symbols

f_{brb}	Fault frequency component for broken rotor bar
f_{ber}	Fault frequency component for broken end ring
f_{ecc}	Fault frequency component for eccentricity faults
f_o	Fundamental Supply frequency,
p	Number of pole pairs,
s	Slip of the machine
R	Number of rotor slots,
v	Order of the stator time harmonics that are present in the power supply driving the motor, ($v = \pm 1, \pm 3, ...$)
n_d	Variable for eccentricity faults classification
$x[n]$	nth sample of infinite order time series
n	Sample instance
N	Total length of finite sequence obtained from the infinite time-series. It also represents the number of FFT points
j	$\sqrt{-1}$
$O(\cdot)$	Order of complexity
r_{xx}	Autocorrelation sequence
ν	Additive white gaussian noise
σ^2	variance of noise
F_s	Sampling frequency
$X(\omega)$	DTFT sequence
$X[k]$	k point FFT sequence of $x[n]$
$P_x(\omega)$	power spectral density
$\mathbf{A}$	Complex source array matrix
$(\cdot)^*$	Complex conjugate
$(\cdot)^H$	Hermitian transpose of a matrix
$(\cdot)^T$	Transpose of a matrix
$\mathbf{I}$	Identity matrix
P	Number of sinusoids

s_i	Amplitude of ith sinusoid
φ_i	Complex and random phase of ith sinusoid
f	Frequency in hertz; search space
ω	Normalized frequency
T_s	Sampling period
$\mathbf{x}$	Vector of $x[n]$
$\mathbf{R_x}$	Autocorrelation matrix
$\mathbf{X}_\beta$	Data matrix
L	Size of the autocorrelation matrix
$\mathbf{A}$	Input manifold matrix
$\mathbf{s}$	Vector of complex amplitude and random phase of P sinusoids
$\mathbf{v}$	Vector of noise samples
v	Noise eigenvectors
$\mathbf{w}(\omega)$	Signal eigenvectors
σ	Eigenvalue
$\hat{h}(\omega)$	Estimated spectral magnitude of ω
$\mathbf{W}$	Search manifold matrix
ω_l	Lower limit of normalized frequency search space
ω_u	Upper limit of normalized frequency search space
$\gamma()$	Decision statistic for probability of resolution
ϕ	Angular position of the rotor w.r.t some stator reference
θ	Particular angular position along the stator inner surface
g_0^{-1}	Inverse air-gap function
L_0	Length of the stack
r_0	Average radius of air-gap
$N_i(\phi, \theta)$	Winding function. This is effectively the Magneto Motive Force (MMF) distribution along the air-gap for unit current in i.
A_o	Amplitude of the fundamental component
ω_o	Angular frequency of the fundamental component
ϕ_o	Phase of the fundamental component
ε_k	Additive zero mean gaussian noise with variance σ_v^2
$\hat{y}_k$	kth instance of the estimated signal
y_k	Measured signal
$\hat{x}_k$	kth instance of the estimated state
$\hat{x}_k^+$	Pre-measurement state estimate
$\hat{x}_k^+$	Post-measurement state estimate
K_k	kth instance of the Kalman gain
P_k	kth instance of the error covariance
P_k^-	Pre-measurement state estimate of the error covariance
P_k^+	Post-measurement state estimate of the error covariance

f_{mecc}	Fault frequency component for mixed eccentricity fault
$\mathbf{\Omega}_i$	Search manifold matrix for ith CF
ω_i^l	Lower limit of frequency search space for ith CF
ω_i^h	Higher limit of frequency search space for ith CF

List of Figures

List of Tables

CHAPTER 1

Introduction

1.1 Background

Squirrel Cage Induction Motors (SCIMs) are the primary motive force provider for any industry and railway transportation. The prevalent maintenance practice of SCIMs in most industries is based on periodic supervision and servicing. Periodic maintenance results in unnecessary expenses and operating equipment and components for suboptimal periods. In the worst case scenario, a component may get completely damaged before the time for its next scheduled maintenance arrive. The SCIM faults in their inception are incipient in nature. As a result, the effect of the fault does not affect the operations drastically. However, the sustained activity under incipient defects can lead to severe damage and abrupt stoppage of the operations. A way out to obviate from the periodic maintenance is by shifting to condition-based maintenance that would require the detection of incipient faults at an earlier stage. A diagnostic module with preemptive fault detection features is a critical and prudent necessity for condition monitoring of SCIMs. This module can improve the reliability and integrity of the SCIMs and aid in avoiding unwarranted downtime.

The advantages offered by AC drives and induction motors have changed the scenario with Indian Railways adopting AC induction motors in a big way. A locomotive engine employs a variety of SCIMs for operations ranging from providing tractive power to cooling and keeping the locomotive dust-free. Due to restricted availability of space in the locomotives, redundancies are nonexistent. Because of this, any outage of any of the machine drastically reduces the capability of the locomotive and can even completely disable it. Faults in the bearings, rotors and electrical faults like winding short circuit, occurring in the motors drastically affects the locomotive performance. It, therefore, becomes necessary

to have monitoring systems of the motors available in a locomotive that would be able to diagnose the health and fault levels of the motors.

Condition monitoring of inductor motor requires an extensive study of the different types of faults and the available detection methodologies. A fault is defined as the an unpermitted deviation of at least one characteristic property of the system from the acceptable, usual and standard condition [1]. Faults are incipient in nature, so even if there is a fault in the system, the system may operate as a normal system with subtle deviation in its states. Fault diagnosis consists of three different steps, 1. Fault detection, 2. Fault Isolation - localization or classification of the fault, and 3. Fault identification - determination of type, magnitude and cause of the fault. Failure is defined as the permanent interruption of the system's ability to perform the required functions, [1]. If faults are not detected and proper maintenance has not been taken, the faulty system leads to complete failure resulting in loss of productivity. Failure prognosis consists of early detection of incipient faults and predicting the remaining useful life before failure. In this research, an onboard and embedded condition monitoring system for SCIMs is envisioned for improving their reliability and reducing their cost of maintenance. The primary research issue is related to the detection of weak and incipient faults under various load conditions when the fault signatures are difficult to detect. The other areas are related to selection and placement of sensors, proper signal conditioning, detection of multiple combined defects, efficient online implementations, etc.

Faults in SCIMs can be broadly classified into rotor faults, stator faults, and bearing faults. Each fault class can further be subclassified as given below

i. Rotor Faults

- Broken Rotor Bar
- Broken End Ring
- Eccentricity Fault
  - Static Eccentricity
  - Dynamic Eccentricity
  - Mixed Eccentricity

ii. Bearing Faults

- Inner Raceway Fault
- Outer Raceway Fault
- Rolling Element Fault

iii. Stator Faults

- Inter turn short circuit

- Phase to phase short
- Phase to ground short

This thesis is mainly concerned with the class of rotor faults. A brief literature review about the different rotor faults along with the sensors and signals that are used is given below:

1.1.1 Broken Rotor Bar and Broken End Ring Faults

These faults are said to occur when due to stress or mechanical defect, the rotor bars or the end ring, which holds together the bars are damaged. Photographs to illustrate the occurrence of BRB of a 750 KW traction motor is shown in Fig. 1.1a. These damaged motors were found during the periodic maintenance in their respective maintenance sheds. The motor on the continual run with single BRB fault, develops multiple bar cracks, as found in Fig. 1.1b. Leading causes of these failures are attributed to manufacturing defects, unbalanced magnetic pull due to load transients and asymmetrical loading patterns. [2]. The occurrence of eccentricity related anomalies can also lead to unbalanced magnetic pull, which may result in BRB. This fault results in unbalancing of the rotor that causes unbalance in the motor magnetic field. The unbalanced magnetic field is decomposed into positive and negative sequence components. These positive and negative sequence components of the unbalanced magnetic field induce multiple fault frequency components on both side of the fundamental frequency given by [3, 4, 5, 2]

$$f_{brb} = f_{ber} = (1 \pm 2ks) f_o \tag{1.1}$$

Where s is the slip, k is any integer, and f_o is the supply frequency. According to [2], the lower side components are due to BRB and BER while the upper ones are for speed oscillations. It is also shown in [6], that the magnitude of the frequency component can quantify the severity of the fault. Other higher order components for BRB are given by [2]

$$f_{brb} = \left[\left(\frac{k_2}{p} \right) (1 - s) \pm s \right] f_o \tag{1.2}$$

where, the symbols have their usual meaning with k_2/p being any positive integer and p is the number of pole pairs. Initially, small cracks may develop in the structure, but with prolonged usage, these may develop into more severe defects and may eventually lead to multiple faults due to uneven thermal stress because of localized heating. If left undetected, this can result in stator-rotor rub. It is, therefore, of utmost importance, that these faults are detected in its inception. The multiple BRB fault considerably distorts the stator current and hence become conspicuously visible in the spectral signature. However, modulation of the stator current due to single broken bar is weak, [6]. Closely spaced components escalate the difficulty of its detection. The onset of BRB degrades the performance of the motor and results in modulated stator currents. Other consequences are torque pulsation

with reduced average torque, rotor speed pulsation with reduced speed, increased losses, decreased efficiency and excessive heating, etc. [7, 8]. Detecting weak faults in low load condition is of great interest to the research community. In this case, the fault components are very close to the supply frequency. As a result, detecting the fault component requires the fundamental to be suppressed adequately without affecting the closely spaced fault frequency. This is accomplished by using a sharp notch filter. However, there are implementation issues, which require the notch filter to be redesigned when there is a change of the fundamental frequency. Moreover, as the sidebands are very close to the fundamental in low load condition, there might arise conditions when the notch filter suppresses the sidebands. As a result, the central frequency of the notch filter should be able to track the fundamental frequency, and its cutoff bandwidth should be adaptive to the slip. In designing unsupervised embedded systems, designing notch filter with these characteristics can be inconvenient.

Jung et al. [9] gave an overview of a full system for implementation of an efficient multiple fault diagnosis system. This proposed system includes an optimum slip estimator, proper sample selector and a frequency auto-search unit. The algorithm was implemented on a DSP board with illustrative results. One of the major problem in detection of BRB is the false alarm caused by the load torque oscillations. New indicators of BRB, which are independent of load torque oscillations were proposed in [10, 11]. Spectral signatures occupying higher bands and independent of load torque oscillations can be found in [12]. Using slot harmonics as potential indicators of BRB was showcased in [13]. Flux [14], instantaneous power factor with phase [15] and air-gap torque [16] were used to mitigate the problems faced by MCSA due to the load torque. Intelligent use of familiar signal processing techniques for better resolution and computational efficiency were demonstrated by [17]. Techniques like frequency signal dimension order [18] and zooming [19] were used to modify the MUSIC algorithm to improve the resolution. Fault components of BRB are heavily dependent on the slip. Studies to make the fault indicators independent of the slip were presented in [20] using optimized time-frequency representations with hidden Markov models and Mahalanobis distance metric as classifiers. Using stator current envelopes as a feature for fault detection was presented in [21]. The amplitude of the fault-specific can quantify the severity of BRB and BER fault. Quantifying the number of broken bars from the current spectrum is shown in [22, 6]. In [23] Total Least Square ESPRIT (Estimation of Signal Parameters via Rotational Invariance Techniques) was used estimating the fault frequency components. Subspace based methods cannot estimate the amplitude of the fault components required for assessment of BRB fault. Simulated annealing algorithm was used to determine the amplitude and hence the fault severity in [23]. Using startup transients as a potential signature for detection of BRB was popularized with wavelet decomposition in [24]. In this paper, wavelet decomposition is used for detection of outer cage faults of double cage induction motors. In [25] ESPRIT with zooming technique was used for better resolution. The amplitude was estimated using least square estimation, which is equivalent

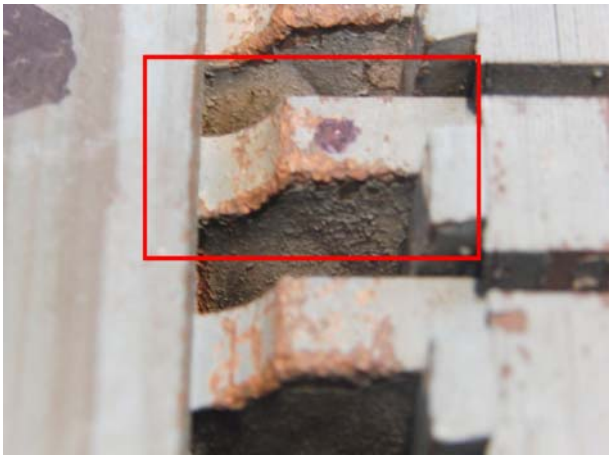

(a) Single BRB fault

(b) Multiple BRBfault

Figure 1.1: Reported BRB in different locosheds. Photo Courtesy: Indian Railways

to computing DFT (Discrete Fourier Transform) for a single frequency. Though efficient, this method is not suitable for finding the amplitude of closely spaced sinusoids [26]. Moreover, with regards to the development of a complete fault detection system, estimation of speed and the fundamental frequency are not discussed elaborately. For investigation of induction motor with BRB fault from stator current, the fundamental component needs to be suppressed adequately for the detection. Most of the research concerned in this area have used spectral estimation for fundamental frequency estimation followed by notch filtering for removing the fundamental. In low load condition, this can lead to suppression of the fault specific components also. Detection of faults in low load condition was accomplished by Hilbert modulus with FFT [27] and Hilbert modulus with ESPRIT [28]. The least slip reported are 0.2% and 0.33% respectively. Effect of simultaneous occurrence of

static eccentricity, BRB and speed ripples were studied analytically and experimentally in [29]. Analyzes with other additional conditions can be found in [30]. Detection of BRB in low load condition with load torque effect can be found in [31]. Here, the diagnosis was performed using continuous and discrete wavelet transform of startup transients. Though fault detection with startup transients is rich, more work is required with transients under load changes. [32] developed an empirical mode decomposition based method for direct, and inverter fed motors to detect BRB. In most of the works, the fault severity is determined for multiple bar breakages. In this thesis, a single bar is broken in different levels to emulate weaker and incipient BRB faults.

1.1.2 Eccentricity Faults

Eccentricity related faults occur when there is an uneven air-gap between the stator and the rotor, [2]. A substantial value of eccentricity can result in an unbalanced magnetic pull that in turn can result in stator-rotor rub or even BRB fault. Similar to the BRB fault, eccentricity fault also creates unbalance in the magnetic field and as a consequence, fault frequency components are induced in the motor armature current. The Frequency components due to this class of fault are given by [2, 33]

$$f_{ecc} = \left[(kR \pm n_d) \frac{(1-s)}{p} \pm v \right] f_o \tag{1.3}$$

Where R is the number of rotor slots. v is the order of the stator time harmonics that are present in the power supply driving the motor, ($v = \pm 1, \pm 3, ...$), and n_d is the variable depending on which eccentricity related faults can be classified as given below.

i. *Static Eccentricity* - Under this condition, the position of the minimum radial air gap remains constant, caused due to ovality of the stator or imperfect positioning of the rotor. Mathematically $n_d = 0$ in (1.3). Static eccentricity fault is illustrated in Fig. 1.2a. It is observed that, in this case, the axis of rotation does not coincide with stator axis but is same as the rotor axis. As a result, a non-uniform stationary air-gap is created, which does not rotate with the rotor.

ii. *Dynamic Eccentricity* - In case of dynamic eccentricity the axis of rotation does not coincide with the axis of the rotor. However, the axis of rotation and the stator axis are same, and the position of the minimal air gap rotates with the rotor. Mathematically, frequency components can be modeled by putting $n_d = 1, 2, 3, ...$ in (1.3). This phenomenon can be visualized in Fig. 1.2b. This misalignment is caused by several factors such as bearing wear, misalignment, bent rotor shaft, and mechanical resonance due to the oscillation of shaft speed.

iii. *Mixed Eccentricity* - In reality, both the static and dynamic eccentricities tend to coexist in a motor. This fact was found to be true for all the motors that were under

this study. When they exist together, the condition is known as the mixed eccentricity. In this case, none of the three centers coincides with each other as illustrated in Fig. 1.2c.

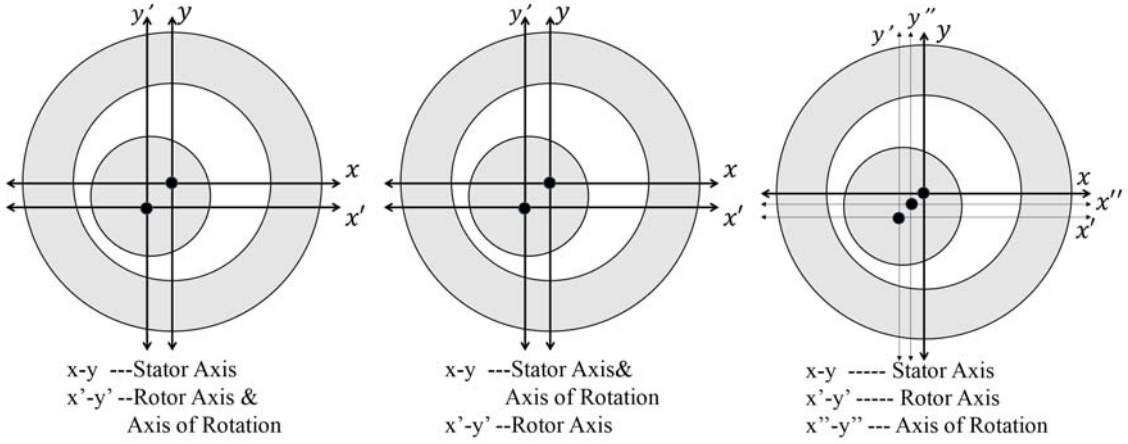

(a) Static eccentricity (b) Dynamic eccentricity (c) Mixed eccentricity

Figure 1.2: Illustration of different eccentricity faults

With increasing eccentricity, the resulting unbalanced forces known as the Unbalanced Magnetic Pull (UMP) can cause stator-to-rotor rub, which can damage the stator and the rotor [2]. At times, the eccentricities in the rotor are tolerated to some extent as a natural manufacturing defect as it cannot entirely be done away with, especially for heavy rotors causing a steady UMP in one direction. This might result in the development of some degree of dynamic eccentricity. Unless detected early, these effects slowly develop into stator or rotor rub, causing a major breakdown of the motor. As a standard practice in the industrial use, air gap eccentricity up to about 10% is permissible [2, 34]. However, manufacturers keep the total eccentricity level even lower to minimize UMP as well as to reduce vibration and noise. The occurrence of air-gap eccentricity results in an asymmetrical stator and rotor circuit inductances as well as degradation of motor performances.

For most of the works, the load torque is considered to be constant. In case of varying load torque, the spectral components produced by the load overlaps with the faults associated with BRB and eccentricity. Schoen et al. in 1995, discussed this effect in [35]. It was also proposed, that the fault component can be distinguished when the load characteristic is known. Identifying dynamic eccentricity components from load-torque oscillation was successful using Wigner distribution in [36] and with instantaneous active and reactive power in [15]. Rotor slot harmonic and eccentricity related faults components are available only for a particular combination of number of rotor slots and the number of fundamental

pole pair as established in [37, 33] and the relation is given by

$$R = 2p[3(m \pm q) \pm r] \pm k \tag{1.4}$$

where, $(m \pm q) = 0, 1, 2, 3, ...$, $r = 0, 1$ and $k = 1, 2$.

Low-frequency components for motors not adhering to this combination can be diagnosed for eccentricity faults by

$$f_{mixed} = |f \pm k f_r| \tag{1.5}$$

where, $f_r = (1 - s)f_o/p$ and k is any integer. In [37] it is shown how this component can be used for sensorless speed estimation method, which has been utilized in this thesis for valid estimation of speed using the inherent mixed eccentricity component. Stator current is inherently non-stationary in nature due to non-uniform load torque and variable supply frequency. In this case, time-frequency based fault detection methods are a necessity. Time-frequency analysis with wavelet packet decomposition [38] and Gabor wavelets [39] are available. Low-amplitude fault components in the vicinity of the fundamental supply frequency are very difficult to distinguish. [40, 15, 41] have used the instantaneous power to circumvent this problem. The Power signal is derived by modulating the supply voltage with the current signal. As a result, the fundamental component is shifted and separated from the fault components. This method requires a high-voltage sensor, that is costly for embedded solutions with low-voltage acquisition modules. Detection of faults with complex apparent power analysis was carried out in [42]. Knight and Bertini in [43] and Nandi et al. in [44] have developed setups for systematic and rigorous experimentation of eccentricity and bearing faults. For experiments with SCIMs connected with drives can be found in [34, 45, 46]. Use of Artificial Neural Networks (ANN) for fault classification based on thresholding were presented in [34]. These methods require the features to be extracted from the motor running under different operating conditions for proper training of the network. Other method based on ANN can be found in [47]. Use of Fuzzy Min-Max with Classification and Regression Tree (FMM-CART) for detection of eccentricity can be found in [48]. Detection of eccentricity with the terminal voltage switched off [44] and under standstill condition with pulsating input from the drive [45] are also famous. Condition monitoring of SCIM with eccentricity fault with online implementation is shown in [49]. Practical quantification and safe operating condition of the motor under various load with eccentricity fault were discussed in [50]. Instead of using current and voltage signatures, a Rogowski coil was used for analysis of the external magnetic field for eccentricity fault in [51]

Effect of slotting on mixed eccentricity with experimental validation was carried out in [52] with a dual-stator winding SCIM. Finite element model based detection of mixed eccentricity was accomplished in [53] by comparing the spectrum of a healthy simulated

model with the faulty motor. Effect of load variation [54], magnetic saturation [41] and stator inductance fluctuation [55] on static and dynamic eccentricity with Time Step Finite Element Model (TSFEM) and modified winding function model of SCIM are also available. Dorrell in [56] studied the effect of rotor flux, the number of bars and saturation on source and characteristic of UMP for static and dynamic eccentricity.

The frequency components obtained from literature is tabulated in Table 1.1.

Table 1.1: Theoretical fault frequency components, with $p = 2$

Sl. No.	Fault	R	Spectral Signature	
1	BRB/BER	NA	$(1-2s)f_o$	$(1+2s)f_o$
			$(1-4s)f_o$	$(1+4s)f_o$
2	Static Eccentricity	28	$(13-14s)\,f_0$	$(15-14s)\,f_0$
			$(11-14s)\,f_0$	$(17-14s)\,f_0$
			$(9-14s)\,f_0$	$(19-14s)\,f_0$
		40	$(19-20s)\,f_0$	$(21-20s)\,f_0$
			$(17-20s)\,f_0$	$(23-20s)\,f_0$
			$(15-20s)\,f_0$	$(25-20s)\,f_0$
		41	$(39-41s)\,f_0/2$	$(43-41s)\,f_0/2$
			$(35-41s)\,f_0/2$	$(47-41s)\,f_0/2$
			$(31-41s)\,f_0/2$	$(51-41s)\,f_0/2$
3	Dynamic Eccentricity	28	$(25-27s)\,f_0/2$	$(29-27s)\,f_0/2$
			$(21-27s)\,f_0/2$	$(33-27s)\,f_0/2$
			$(27-29s)\,f_0/2$	$(31-29s)\,f_0/2$
			$(25-29s)\,f_0/2$	$(33-29s)\,f_0/2$
		40	$(39-41s)\,f_0/2$	$(43-41s)\,f_0/2$
			$(37-41s)\,f_0/2$	$(45-41s)\,f_0/2$
			$(37-39s)\,f_0/2$	$(41-39s)\,f_0/2$
			$(33-39s)\,f_0/2$	$(45-39s)\,f_0/2$
		41	$(20-21s)\,f_0$	$(22-21s)\,f_0$
			$(18-21s)\,f_0$	$(24-21s)\,f_0$
			$(19-20s)\,f_0$	$(21-20s)\,f_0$
			$(17-20s)\,f_0$	$(23-20s)\,f_0$
4	Mixed Eccentricity	NA	$(1+s)\,f_o/2$	$(3-s)\,f_o/2$

1.1.3 Signals and Sensing Techniques for Fault Detection

Fault detection of SCIM demands detection of faults well in advance while the motor is still operational to avoid unscheduled maintenance and prolonged downtime. Fault detection can be accomplished by analyzing a variety of signals from the motor like

i. *Vibration signal* is one of the most popularly sensed signals for fault detection of

mechanical subsystems [57, 58]. Most of the anomalies of a motor like BRB [59, 60], eccentricity [57], inter-turn short circuit [58, 61, 62, 63], and bearing [58, 64, 65] faults can be detected using vibration. One of the major drawback is the effective placement of sensors. Additionally, it requires an elaborate instrumentation arrangement for proper working and is very costly and fragile.

ii. *Magnetic fields* for fault detection of SCIMs deals with the acquisition of magnetic flux with a search coil wound around one of the stator tooth [14, 51]. This method needs compound sensor arrangement and fixations for each motor. Search coil based fault diagnosis requires the installation of pick-up coils at appropriate places to capture the flux pattern near stator slots or on the frame of the motor. It is not always feasible to use search coils on all machines to monitor the fault modulated flux signal. It is also difficult to locate the best position of the search coils to capture the signal modulated by the faults efficiently. Moreover, static and dynamic characteristics of the search coil might interfere with the detection procedure.

iii. *Supply voltage modulation* is also used effectively for detection of SCIM faults as shown by [66]. However, the major disadvantage lies in the fact that the sensor has to be attached to either of the supply or motor terminals. In cases like that of the locomotive systems, most of the motor terminals are out of reach and acquiring high voltage signals can pose a safety issue. For an instance, the terminal voltage of a 750 kW traction motor may reach to 2.5 kV at rated speed. Also for a motor driven by Variable Frequency Drive (VFD), it is very difficult to detect the voltage modulation.

iv. *Active-reactive power analysis* [67, 15] was popularized due to its effectiveness for analyzing the motor under time varying loads, and its ability to distinguish between rotor fault and load torque oscillations. However, acquiring voltage signals for this method is challenging.

v. *Acoustic signals* were the earliest known signs utilized by human to detect the fault in a system. In case of a motor, acoustic signal were employed by [57] to detect rotor eccentricity. Though potent for a single motor, the problem escalates when multiple motors operate in tandem. Detection and isolation of faults from multiple sources within an enclosed environment like the locomotive engine is an arduous task.

vi. *Thermal field analysis* [68] and *Thermal imaging* [69], although used widely used for fault detection in various heavy industries, are not very familiar in the case of induction motors. Thermal field analysis is a model based approach, where the temperature distribution and the heat loss are found in terms of the electromagnetic field. Further details can be found in [70]. Thermal imaging is based on finding the temperature distribution using thermal imaging technologies.

Extracting fault-significant information from thermal images is complicated due to the outer metallic cover of motors. However, It can be used for detection of the stator and the bearing related failures.

vii. *Current signal* [37, 71, 72, 9, 17, 73, 27, 6, 74, 39, 25] is most widely used for motor fault detection due to multiple reasons. Most of the motor faults can be detected from current, the methods are independent of motor parameters and acquiring current signal is non-invasive due to the availability of clamp-type Hall sensors. These sensors are clamped around the cable for sensing and need not be placed on the motor or the terminals. Fault detection methods concerned with stator current came to be known as Motor Current Signature Analysis (MCSA). A marked disadvantage of MCSA is that it is only valid for the motor operating under steady state condition, or the acquired signals are statistically stationary. Although, this problem can be circumvented with time-frequency analysis tools. However, spectral analysis of the stator current is the most popular technique [2].

Most of the embedded design strategies in recent past were limited to Field Programmable Gate Array (FPGA) and Digital Signal Processor (DSP) based systems. A brief overview of some of the systems are given below:

Khan et al. in [75] implemented an online wavelet-based SCIM fault detection system. Texas Instrument's board with 32bit floating point processor, TMS320C31 was used for this development. [76] have identified BRB by the online application of a detection algorithm on a DSP commercial board, TMS320F28335. Hardware development with a low-cost FPGA-based online system for BRB detection was demonstrated in [77]. The detection scheme is based on the Discrete Wavelet Transform (DWT) of the startup current to identify fault during motor startup. XC3S200 Spartan-3 FPGA from Xilinx was used for online implementation. [78] have reported the development of an FPGA-based special purpose System-on-a-Chip (SoC) solution for online detection of half BRB fault in SCIM. This method used both current and the 3-axis vibration signal to improve the detectability under various loading conditions. XC3S500E Spartan-3 FPGA from Xilinx is used for online implementation. [79] have implemented another FPGA based online system to detect induction machine faults. The system works based on the Entropy and Fuzzy Inference to detect multiple combined SCIM faults. FPGA Cyclone-II EP2C35F672C6 from Altera is used for online implementation.

1.2 Motivation and Objective

The absence of proper condition monitoring systems in industries like the Indian Railways is the major motivation for this study. Some of the issues in designing such a system along with the objective for this research is provided below:

i. Online condition based monitoring as opposed to scheduled monitoring and maintenance of SCIMs can be advantageous in many ways. Periodic maintenance might be sometimes unnecessary, and sometimes the motor may be sufficiently damaged before any maintenance is carried out. This maintenance procedure results in high cost and loss of valuable human labor. An embedded online system for assessment of the conditions of an SCIM to avoid unnecessary periodic maintenance is the primary aim of this research.

ii. Experiments with large induction motor with the required loading arrangement are very difficult to conduct under laboratory condition. Emulating a combination of faults as well as faults under various physical conditions like variable loading for generating fault signatures is essential for testing the fault diagnosis system. Conducting these studies with the experimental motor can be detrimental to its health and is unsafe to be operated with faults. Operating SCIMs with fault can damage the motor permanently, is costly and have safety related issues. For this reason, development of an SCIM fault simulator is essential, that can simulate different faults under various physical conditions.

iii. Condition monitoring of SCIMs require accurate identification and quantification of fault specific frequency component. The fault components are of a small magnitude and very close to other significantly larger components thus making its detection and identification difficult. Subspace-based methods like MUSIC can circumvent this problem. However, subspace-based methods require model order information, cannot quantify the degree of fault and are computationally intensive. Hence, development of a high-resolution low-complexity spectral estimator suitable for detection and quantification of induction motor fault is paramount.

iv. Most of the faults are initiated from an incipient stage. It is always advantageous to detect these condition in their inception when the fault is weak. A weak fault does not significantly affects the operations, and its signature is also feeble. Efficient signal conditioning strategies are needed to detect these faults. Extended Kalman Filter (EKF) based methods have shown promising results to this end.

1.3 Organization of the Thesis

The thesis is organized as follows:

Chapter 1: *Introduction* - This is the introductory chapter and it presents the existing literature for fault diagnosis. It gives an overview of sensors, systems and algorithms used for detection of BRB and eccentricity faults. This chapter ends with a discussion of the

motivation and objective of this research.

Chapter 2: *Development of the Proposed Spectral Estimator* - Presents the Rayleigh quotient-based spectral estimator with its derivation and evaluates the performance of the spectral estimator and compares it with MUSIC and DFT. This chapter also derives the relation for determination of accurate amplitude from the spectral peaks.

Chapter 3: *Development of the Real-time SCIM Fault Simulator* - Presents an insight into the development of the RT SCIM fault simulator with simulation results of different faults with varying degrees of the defect, under various conditions of loading.

Chapter 4: *Induction Motor Weak Fault Detection Algorithm* - Discusses the fault detection system with full analysis of the faults emulated on the experimental setup. This chapter thoroughly discusses the different subsystems of the fault assessor like signal conditioning, slip and fundamental frequency estimation, and determination of thresholds which are vital for successful detection of faults.

Chapter 5: *Embedded System Development for Online Fault Diagnosis* - Presents the embedded system development schemes for single fault detection, multiple fault detection, spectral estimation, and fault simulation.

Chapter 6: *Conclusion and Future Directions* - Presents the contribution and concluding remarks of the thesis along with the future research directions.

CHAPTER 2

Development of the Proposed Spectral Estimator

It is well established that spectral analysis of the stator current is one of the most reliable methods of detecting SCIM faults. The classical problem of detecting low-amplitude sinusoids in noise has gained prominence in the recent years for MCSA-based fault detection. Most of the fault frequency components have feeble magnitude and are very close to other significant components in the frequency spectra. Moreover, these components are motor slip dependent. As a result, the location of the components changes with time. It, therefore, accentuates the need for developing spectral estimators that can detect closely-spaced low-amplitude sinusoids in noise with the least number of samples. For the detection of BRB fault, the situation is more complicated because the fault frequency components are in close vicinity of the fundamental. The amplitude of the fault frequency component is a measure of the severity of a fault. It is advantageous if the spectral estimator can reliably determine the sinusoidal amplitude at various frequency component on the spectrum. For online fault monitoring, the spectral estimator will run on an embedded platform. Online and embedded applications require the algorithm to have low computational complexity. The aim of this chapter is to develop a spectral estimator with the following properties:

- Resolve closely spaced sinusoids.
- Detect low amplitude sinusoids buried under noise.
- Determine the accurate amplitude of constituent sinusoids.

- Low computational complexity

The proposed spectral estimator will be used for offline as well as online fault analysis of the motor for both the simulator as well as the experimental setup. The Performance of a spectral estimator can be judged by its resolving power and its accuracy in detecting them. In this chapter, the resolving power is determined through the Probability of Resolution (POR) and its accuracy is established through error estimates simulated under various conditions. A general framework for the hardware implementation of the spectral estimator will be discussed in chapter 5.

2.1 The Signal Model

The signal is assumed to have the following model:

$$x[n] = \sum_{i=1}^{P} s_i e^{j(\omega_i n + \varphi_i)} + \nu[n]; n = 0, 1, \cdots \tag{2.1}$$

Where $x[n]$ is the n-th instant of the input signal and is considered to be complex exponential with additive white Gaussian noise $\nu[n]$. P is the number of sinusoids. Each sinusoid has an amplitude s_i , with random phase φ_i, and normalized frequency ω_i, given by $2\pi f_i T_s$. T_s is the sampling period. An experiment was conducted with a test signal obtained from (2.1) to demonstrate the resolving power of each estimator with 1024 frequency points. For this experiment, four real sinusoidal signals with unity amplitude and frequencies of [45, 50, 51, 60] Hz was used. Sampling frequency was kept at 1000 Hz. A brief overview of the different spectral estimator prevalent in fault detection are given below:

2.2 Discrete Fourier Transform

Any finite energy stationary signal can be represented by a linear combination of complex exponentials. The representation of the signal in terms of spectrum of coefficients is accomplished with Discrete Time Fourier Transform (DTFT) of a discrete time-series $x[n]$ and is given by

$$X(\omega) = \sum_{n=0}^{N-1} x[n] e^{-j\omega n} \tag{2.2}$$

Now, in this method the frequency components are distributed over a continuous spectral band that is not suitable for digital implementation and computation. As a result, Discrete Fourier Transform (DFT) was formulated. In this method, the frequency is represented as a function of an integer k. For a finite time series $x[n]$ of length N, the N-point DFT is

given by

$$X[k] = \sum_{n=0}^{N-1} x[n] e^{-j\frac{2\pi kn}{N}} \tag{2.3}$$

DFT has a computational complexity of $O(N^2)$. Computational complexity of DFT was reduced to $O(Nlog_2N)$ with a class of algorithms commonly known as Fast Fourier Transform (FFT). Spectrum with FFT implementation is shown in Fig. 2.1.

2.3 Power Spectral Density

Power spectral density is defined as the Fourier transform of the autocorrelation sequence r_{xx}. It is given by

$$P_x(\omega) = \sum_{k=-\infty}^{\infty} r_{xx}(k) e^{-jk\omega} \tag{2.4}$$

where the autocorrelation sequence, $r_{xx}(k) = \lim_{N\to\infty} \frac{1}{N} \sum_{n=0}^{N-1} x(n+k)x^*(n)$. There are different ways of estimating power spectrum. One such traditional method is Welch's method of averaging periodograms for better accuracy as shown in Fig. 2.2.

2.4 Subspace Based Spectral Estimators

The methods discussed above are not suitable for signals where the sinusoids are closely spaced, or there is a considerable amount of noise. In these scenarios, subspace-based methods are used. Subspace-based methods utilize the property of orthogonality of noise and signal eigenvectors of the signal autocorrelation matrix. These methods can be classified as signal and noise subspace-based methods. Signal subspace-based methods or principal component-based methods use eigenvectors that lie in the signal subspace for their computations. Whereas, the noise subspace-based methods or minor component analysis are based on the noise eigenvectors. Most of the recent studies on fault detection have mainly concentrated on the noise subspace-based methods. Two popular methods are MUSIC and ESPRIT. Out of these, we will discuss MUSIC with some details. MUSIC was developed to find the direction of arrival (DOA) of two closely spaced sources in radar technology and array signal processing. MUSIC was found to be very efficient in resolving closely spaced sinusoids for fault detection of induction motors. In recent years, most of the research in this domain was carried out with signal sources impinging on an array of sensors and the problem is to find the DOA of the signals arising from these sources. The Output of the array sensors is considered as the input signal for the spectral analysis.

For mathematical simplicity and to maintain a similar structure with the existing works, the model in (2.1) is represented by a finite order sequence in a vector-matrix form. The order of this sequence is determined by the autocorrelation matrix size (L) which results in truncation of the infinite order time-series into finite order samples. The finite vector $\mathbf{x}$ of $x[n]$ is given by

$$\mathbf{x} = \mathbf{A}\mathbf{s} + \mathbf{v} \tag{2.5}$$

where $\mathbf{s} \in \mathbb{C}^{p\times 1}$ is the vector of P complex amplitudes with random phase

$$\mathbf{s} = [s_1 e^{j\varphi_1}, s_2 e^{j\varphi_2}, ..., s_p e^{j\varphi_P}]^T \tag{2.6}$$

and $\mathbf{A} \in \mathbb{C}^{L\times P}$ is the complex source array matrix given by

$$\mathbf{A} = [a(\omega_1), a(\omega_2), ..., a(\omega_p)] \tag{2.7}$$

where $a(\omega_i) = [1, e^{jw_i}, ..., e^{j\omega_i(L-1)}]^T$ The noise vector $\mathbf{v}$ is given by

$$\mathbf{v} = [\nu(1), \nu(2), ..., \nu(n)]^T \tag{2.8}$$

The covariance of the input signal is given by

$$\begin{aligned} \mathbf{R_x} &= E[\mathbf{x}\mathbf{x}^\mathbf{H}] + \sigma^2\mathbf{I} \\ &= \mathbf{A}E[\mathbf{s}\mathbf{s}^\mathbf{H}]\mathbf{A}^\mathbf{H} + \sigma^2\mathbf{I} \\ &= \mathbf{A}\mathbf{R_s}\mathbf{A}^\mathbf{H} + \sigma^2\mathbf{I} \end{aligned} \tag{2.9}$$

Where, σ^2 is the variance of the noise and $\mathbf{I}$ is the $L \times L$ identity matrix. Here, L is the size of the autocorrelation matrix. The largest P eigenvalues of $\mathbf{R_x}$ represent the P sinusoidal components present in the signal, while the other $m = L - P$ eigenvalues represent the noise. Similarly, the eigenvectors corresponding to the P eigenvalues belongs to the signal subspace, whereas the rest, represented by v belongs to the noise subspace. The spectral peaks of MUSIC are estimated by

$$\hat{h}(\omega) = \frac{1}{\sum_{i=1}^{m} |\mathbf{w}(\omega)^T v_i|^2} \tag{2.10}$$

where $\mathbf{w}(\omega) = \begin{bmatrix} e^{j\omega\cdot 0} & e^{j\omega} & \cdots & e^{j\omega\cdot(L-1)} \end{bmatrix}^H$, $\omega = 2\pi f/F_s$. Where $f \in [0, F_s/2]$, and, therefore, $\omega \in [0, \pi]$. It is observed from Fig. 2.3 that MUSIC is able to resolve the closely spaced frequency components whereas, FFT and PSD are not successful in doing so. MUSIC

is known as a high-resolution spectral estimator as it can resolve sinusoids that are closer than their Fourier limit given by F_s/L. It is also observed that MUSIC has a very smooth spectrum. As a result, false detection of sinusoids due to spurious peaks is very low as compared to the other methods. Initially, FFT and PSD were used as spectral estimators for SCIM fault detection due to their simple implementation. However, these estimators are unable to resolve closely spaced sinusoids, which is crucial for the detection of weak faults under low load condition. MUSIC can detect the low-magnitude fault components. However, high computational complexity and accurate knowledge about the number of sinusoids in the input signal are the major drawbacks of MUSIC. The spectrum obtained with MUSIC with the test signal is shown in Fig. 2.3.

2.5 The proposed Spectral Estimator

In recent years, methods such as MUSIC [17] and ESPRIT [25] have surpassed the classical method of the power spectrum by leap and bounds through it robustness and resolution capacity for fault detection of SCIMs. However, eigen decomposition of the autocorrelation matrix in MUSIC makes it difficult for embedded and RT applications. In this work, successful implementation of MUSIC in RT environment was accomplished, although with limitations of accuracy and sampling frequency. In this chapter a Rayleigh quotient-based spectral estimator is proposed. The proposed spectral estimator can resolve closely spaced sinusoids, with lower computational complexity compared to MUSIC. The proposed method can also estimate the relative amplitude of constituent sinusoids accurately unlike MUSIC.

This method, as opposed to MUSIC, requires only a vector-matrix multiplication instead of eigenvalue decomposition followed by the multiplication. Also, information about the number of sinusoids is not needed, which is critical for the accuracy of MUSIC. A brief description of the algorithm is given below:

2.5.1 Formation of Autocorrelation Matrix

For estimating the true autocorrelation matrix ($\mathbf{R}_x$), the data matrix ($\mathbf{X}_\beta$) is formed [80] without any interleaved samples.

$$\mathbf{X}_\beta = \begin{bmatrix} x(0) & \cdots & x(L-1) \\ \cdot & \cdots & \cdot \\ x(L-1) & \cdots & x(2L-2) \end{bmatrix} \tag{2.11}$$

Assuming the process to be ergodic, $\mathbf{R}_x$ is given by

$$\hat{\mathbf{R}}_x = \frac{1}{L}\{\mathbf{X}_\beta^H \cdot \mathbf{X}_\beta\} \tag{2.12}$$

If $\mathbf{A}$ is a symmetric matrix with eigenvector $\mathbf{v}$, then there exist a corresponding eigenvalue (σ), which can be approximated using the theory of Rayleigh quotients ([81], Pg. 301-304) as

$$\sigma = \frac{\mathbf{v}^H \mathbf{A}\mathbf{v}}{\mathbf{v}^H \mathbf{v}} \tag{2.13}$$

As $\hat{\mathbf{R}}_x$ is a symmetric matrix and $\mathbf{w}(\omega)$ is the eigenvector ([82], Pg. 452), then, the presence of a sinusoid at ω will contribute to a peak, $\hat{h}(\omega)$ which is the eigenvalue corresponding to the eigenvector $\mathbf{w}(\omega)$.

$$\hat{h}(\omega) = \frac{\mathbf{w}(\omega)^H \hat{\mathbf{R}}_x \mathbf{w}(\omega)}{\mathbf{w}(\omega)^H \mathbf{w}(\omega)} \tag{2.14}$$

where, $\mathbf{w}(\omega) = \begin{bmatrix} e^{j\omega\cdot 0} & e^{j\omega} & \cdots & e^{j\omega\cdot(L-1)} \end{bmatrix}^H$ and $\mathbf{w}(\omega)^H \mathbf{w}(\omega) = L$. The approximated eigenvalue is related to the amplitude of the sinusoid present in the input signal.

2.5.2 Mathematical Derivation

Putting the estimate of (2.12) in (2.14) gives

$$\hat{h}(\omega) = \frac{1}{L^2} \left[\left(\mathbf{X}_\beta \mathbf{w}(\omega) \right)^H \cdot \left(\mathbf{X}_\beta \mathbf{w}(\omega) \right) \right] \tag{2.15}$$

The product in (2.15) can be decomposed as given below:

$$\mathbf{X}_\beta \cdot \mathbf{w}(\omega) = \begin{bmatrix} \sum_{i=0}^{L-1} x(i) e^{-j\omega i} & \cdots & \sum_{i=0}^{L-1} x(i+L-1) e^{-j\omega i} \end{bmatrix}^T \tag{2.16}$$

Now, with the assumption that

$$X_q(\omega) = \sum_{r=0}^{L-1} x(r+q) e^{-j\omega r} \tag{2.17}$$

and using this in (2.16) it is obtained that

$$X_\beta \cdot \mathbf{w}(\omega) = \begin{bmatrix} X_0(\omega) & \cdots & X_{L-1}(\omega) \end{bmatrix}^T \tag{2.18}$$

putting the value of $X_\beta \cdot \mathbf{w}(\omega)$ in (2.15) gives

$$\hat{h}(\omega) = \frac{1}{L^2} \begin{bmatrix} X_0^*(\omega) & \cdots & X_{L-1}^*(\omega) \end{bmatrix} \cdot \begin{bmatrix} X_0(\omega) & \cdots & X_{L-1}(\omega) \end{bmatrix}^T \tag{2.19}$$

Simplifying the above, we get

$$\hat{h}(\omega) = \frac{1}{L^2} \sum_{i=0}^{L-1} |X_i(\omega)|^2 \tag{2.20}$$

Now taking square of the absolute value on both sides in (2.17) and putting this value in (2.20) we get

$$\hat{h}(\omega) = \frac{1}{L^2} \sum_{i=0}^{L-1} \left| \sum_{v=0}^{L-1} x(v+i) e^{-j\omega \cdot v} \right|^2 \tag{2.21}$$

Fig. 2.4 shows the spectrum obtained with the proposed spectral estimator. It is observed from Fig. 2.1 and Fig. 2.2 that FFT and PSD are unable to resolve the closely spaced sinusoids. It is also seen that the location and the magnitude of the detected frequency components are not reliable. With MUSIC and the proposed methods, the frequency components are resolved as exhibited by Fig. 2.3 and Fig. 2.4. Moreover, it is observed from Fig. 2.4 that the peak spectral magnitude is uniform as the input sinusoids were of equal magnitude. This fact is important, as it will be shown how these peaks are related to the amplitude of the constituent sinusoids in subsequent sections.

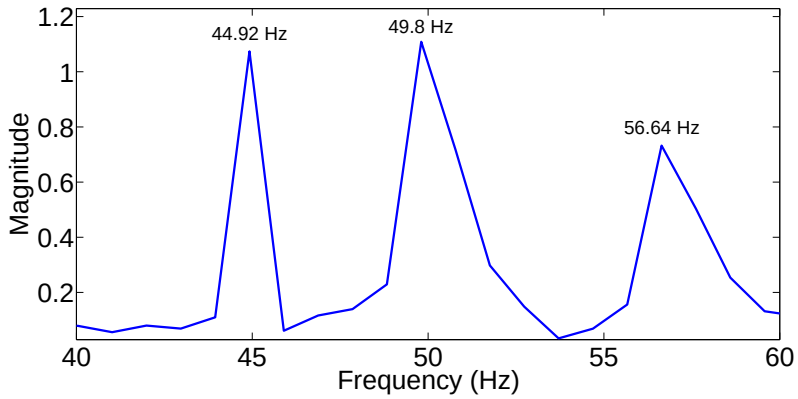

Figure 2.1: 1024 point FFT of the synthetic signal

2.6 Evaluation of the Proposed Spectral Estimator with Probability of Resolution

Resolvability of the closely spaced sinusoid is considered a vital benchmark for determining the efficiency of high-resolution spectral estimation algorithms [83]. Computational complexity and the associated execution time are the performance indices used for evaluation

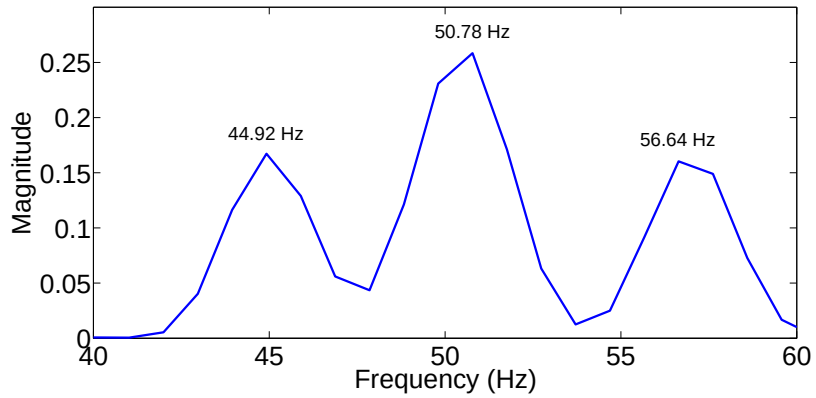

Figure 2.2: 1024 point PSD of the synthetic signal

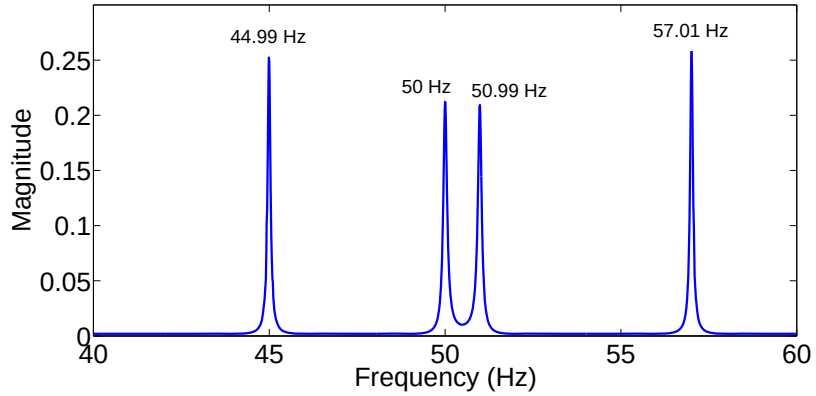

Figure 2.3: MUSIC applied to the synthetic signal

of spectral estimators. The Performance of the spectral estimator in terms of its resolution capability is evaluated statistically by POR. The resolution of a spectral estimator depends on a variety of indices. In this thesis, the POR for the proposed spectral estimator is statistically evaluated in terms of its autocorrelation matrix size, the sampling frequency, and the noise variance. The event of successful resolvability of two sinusoids (with frequencies f_1 and f_2) is determined by the decision statistic, $\gamma(f_1, f_2)$ in (2.22). The event of resolution is illustrated in Fig. 2.5. All the experiments were conducted on HP Z420 Workstation, having 2.80 GHz Intel Xeon CPU E5-1603 processor, 16 GB RAM, and 64-bit Windows 7 operating system. The simulations were carried out with MATLAB R2014a.

$$\gamma(f_1, f_2) \triangleq h(f_m) - \frac{1}{2}\{h(f_1) + h(f_2)\} < 0 \tag{2.22}$$

where $f_m = \frac{1}{2}(f_1 + f_2)$ and $h(f_i)$ is the magnitude of the ith peak in the spectrum.

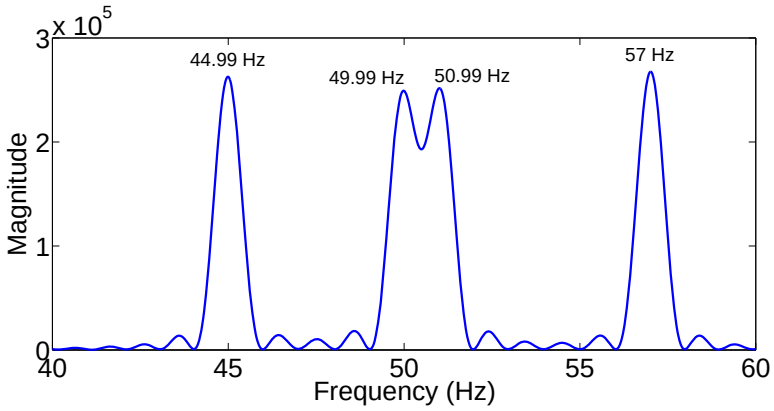

Figure 2.4: The proposed method applied to the synthetic signal

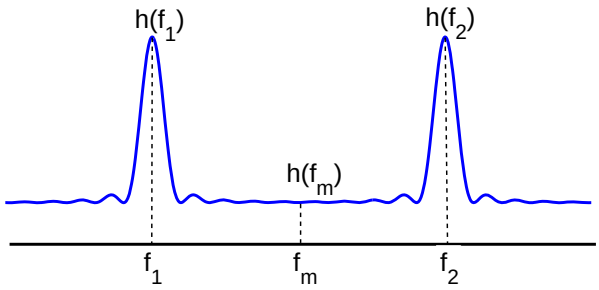

Figure 2.5: Spectral Peaks

2.6.1 Dependence on Autocorrelation Matrix Size

For accurately resolving two closely spaced sinusoids, a minimum size of the autocorrelation matrix needs to be set. However, increasing the matrix size increases the computational burden as evident from Fig. 2.6. For this experiment, 100 trials were carried out to find the execution time for each L.It is also evident from this figure that the proposed spectral estimator has a much lower time complexity for a particular L when compared to MUSIC.

The minimum size of the autocorrelation matrix required for resolving two sinusoids was determined statistically using the principle of POR. The POR for various matrix sizes with different noise variance is shown in Fig. 2.7. In this experiment, two sinusoids with unity magnitude and a frequency difference of 1 Hz were considered. The sampling rate of 1000 samples/sec was taken. It is evident from this figure that an autocorrelation matrix size of $L = 970$ is sufficient to resolve two sinusoids of equal magnitude with a frequency difference of 1 Hz for a worst case scenario of 0 dB SNR.

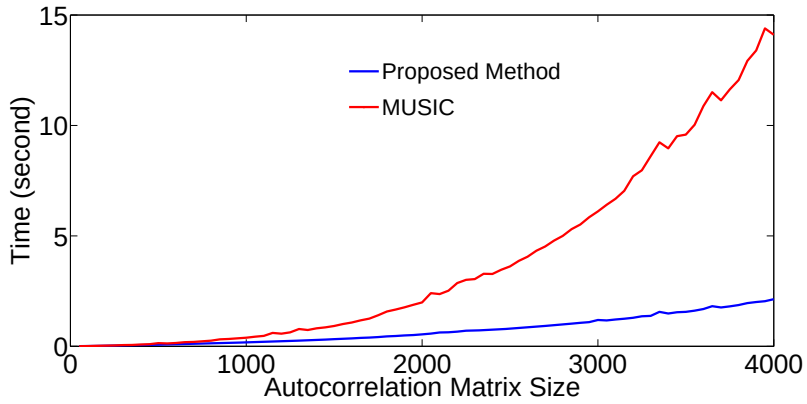

Figure 2.6: Execution time required for MUSIC and the proposed method for various autocorrelation matrix size (L)

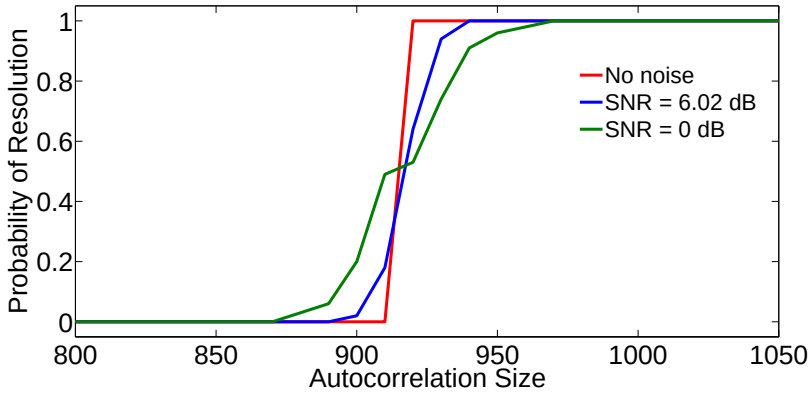

Figure 2.7: POR for different Autocorrelation matrix size (L) with noise variance as the parameter for the proposed spectral estimator

2.6.2 Dependence on Sampling Frequency

Fault detection of induction motors requires the input signal to be sampled by a variety of sampling rates. Faults like broken rotor bar, broken end ring, mixed eccentricity and estimation of speed requires low sampling rates as compared to faults of static and dynamic eccentricity. Sampling rate plays a significant role in the resolvability of closely spaced sinusoids. With increasing sampling frequency, the resolution performance of a spectral estimator drops drastically as observed in Fig. 2.8. For this experiment, the sampling frequency was varied for different values of L. The POR was determined over 100 trials for each F_s. Sinusoidal components with a difference of 1 Hz was taken. The amplitude of each sinusoid was taken to be unity.

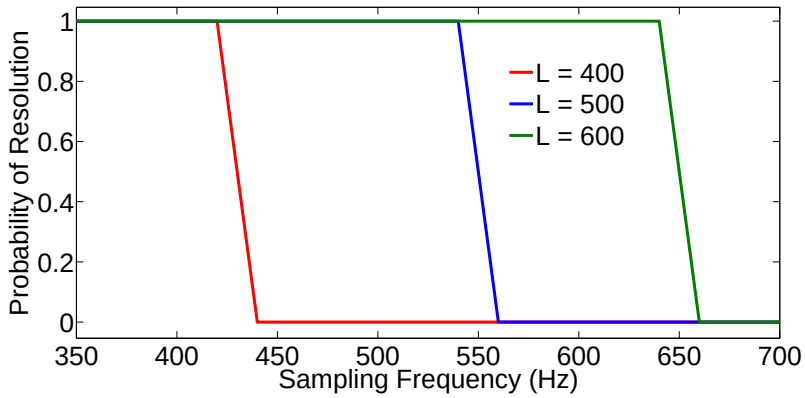

Figure 2.8: POR for different sampling sate (F_s) with autocorrelation matrix (L) as the parameter for the proposed spectral estimator

2.6.3 Robustness of the Spectral Estimator

Noise plays a crucial role in resolving two sinusoids and also in the estimation of the amplitude. It is observed in Fig. 2.9 that with an input SNR of -5dB, two sinusoids with equal magnitude can be resolved if the ratio of F_s/L is maintained. For this experiment, the SNR was varied from -15 dB to 15 dB and L was chosen as 1000 and F_s was 1000 Hz.

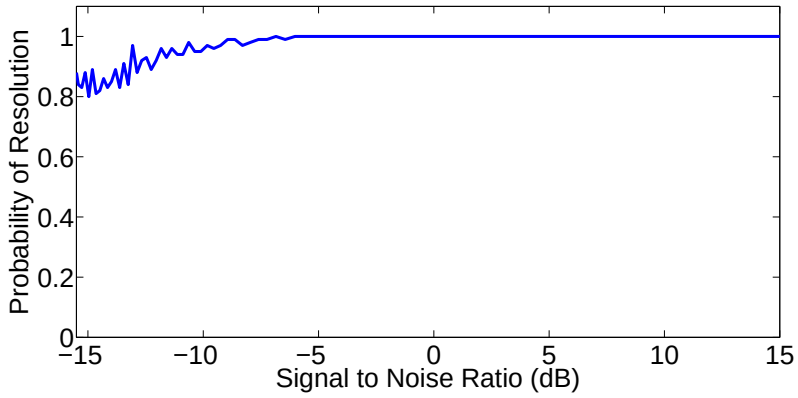

Figure 2.9: Effect of noise on Resolution with POR

2.7 Evaluation and Comparisons of Frequency Estimation Accuracy

It is essential for spectral estimators to provide an accurate estimate of the location of a frequency component on the frequency spectra. In case of fault detection algorithms, an

error may lead to inaccurate estimation and assessment of the motor condition. In this section, experiments are performed to compare the robustness of the location estimate for DFT, MUSIC, and the proposed method. In Fig. 2.10a mean square error between the input sinusoidal frequency and the location of the peak obtained from the spectrum is evaluated by 100 trials for each L. The value of L was incremented in steps of 10. F_s for this experiment was fixed at 1000 samples/s and an SNR of 0 dB was selected. In Fig. 2.10b mean square error is evaluated with different Signal to Noise Ratio (SNR) levels for 100 trials each. F_s for this experiment was also fixed at 1000 samples/s and the L was set to 500. A single sinusoid of 50 Hz and unity magnitude was used for both the experiments. From Fig. 2.10a it can be inferred, that although DFT is an efficient method, its use in fault detection should be limited to applications with longer time samples. The proposed method is also error prone with lower values of L, but its performance is comparable to that of MUSIC. From Fig. 2.10b, it is clear that the performance of the proposed spectral estimator in a noisy environment is quite robust and is comparable to that of MUSIC.

2.8 Estimation of Accurate Amplitude

In this section, a brief mathematical derivation is presented to demonstrate how the proposed spectral estimator is used to estimate the amplitude of the frequency components present in the input signal. The same signal model (2.1) is used for this derivation. It is assumed that the input signal consists of only a single component given by

$$x[n] = s_k e^{j(\omega_k n + \varphi_k)} \tag{2.23}$$

Using the value of $x[n]$ in (2.21) we get

$$\hat{h}(\omega_k) = \frac{1}{L^2} \sum_{i=0}^{L-1} \left| \sum_{v=0}^{L-1} s_k e^{j\omega_k (v+i)} e^{j\phi_k} e^{-j\omega_k v} \right|^2 \tag{2.24}$$

$$\begin{aligned} &= \tfrac{1}{L^2} \sum_{i=0}^{L-1} \left| s_k e^{j\omega_k i} e^{j\phi_k} \sum_{v=0}^{L-1} 1 \right|^2 \\ &= \tfrac{1}{L^2} \sum_{i=0}^{L-1} s_k^2 L^2 \\ &= L s_k^2 \sum_{i=0}^{L-1} 1 \\ &= L s_k^2 \end{aligned} \tag{2.25}$$

Therefore, estimate of the amplitude of the sinusoid at ω_k is given by

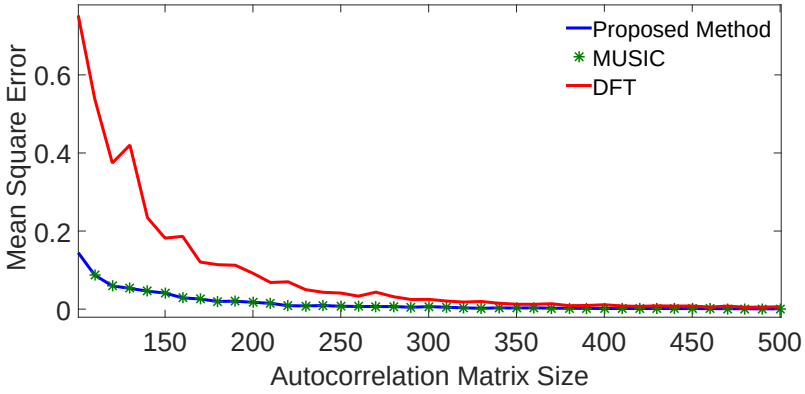

(a) Location error w.r.t Autocorrelation Matrix Size

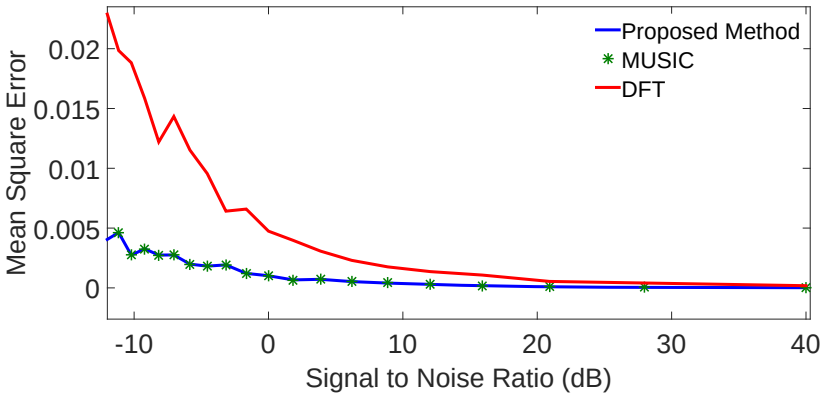

(b) Location error w.r.t SNR

Figure 2.10: Evaluation of location error of spectral estimator

$$\hat{s}_k = \sqrt{\frac{\hat{h}(\omega_k)}{L}} \tag{2.26}$$

Fig. 4.3 shows the accuracy of the proposed spectral estimator for determining sinusoidal amplitude. For this trial, a single sinusoid of 50Hz with varying amplitude was taken, and its spectral estimation is conducted. Subsequently, the peak is detected and using (2.26); the sinusoidal amplitude is estimated. For this experiment, the amplitude was varied from 0.1 unit to 10 units in steps of 0.1. Additive white Gaussian noise with a variance of one unit is also added to this input signal. As a result, the input signal SNR increases with the increasing amplitude for this experiment. It is observed that the peak amplitude is estimated with very low estimation error when compared to the input amplitude.

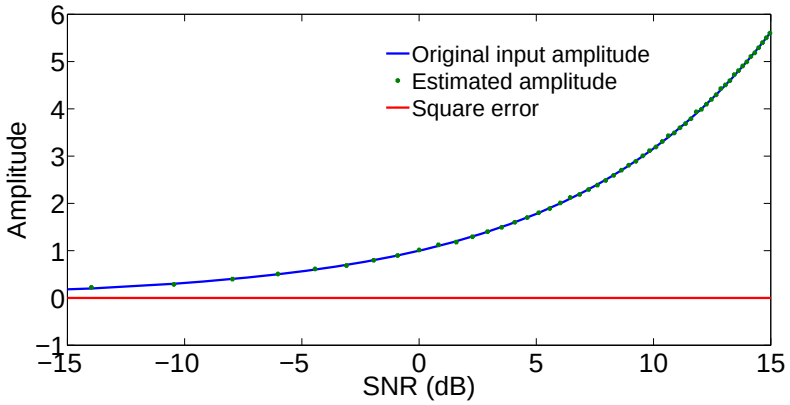

Figure 2.11: Estimation of amplitude

2.9 Effect of Windowing on the Proposed Spectral Estimator

Finite and abrupt windowing of data results in oscillations in the frequency domain resulting in spectral leakages and false peaks that can cause false alarms. This phenomenon is known as Gibbs oscillations ([84], Pg. 491-495). This was also observed in case of the proposed spectral estimator. Using a non-rectangular window with tapered ends can solve this issue. However, this is achieved at the expense of the wider and diminished lobe as is evident from Fig. 2.12. In this thesis, a Chebyshev window was used uniformly for all the experiments.

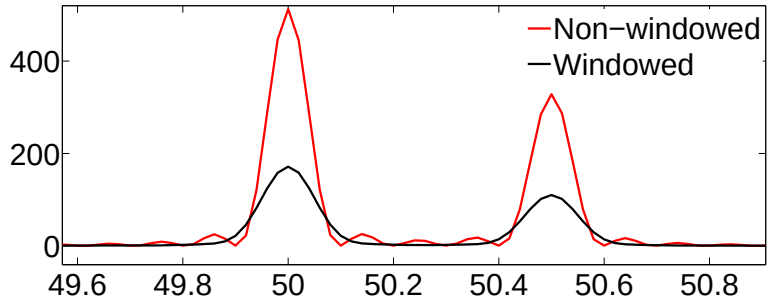

Figure 2.12: Effect of windowing in reducing Gibbs oscillations

2.10 Summary

In this chapter, a novel Rayleigh quotient-based spectral estimator is proposed. The spectral estimator can estimate fault frequency components with very high accuracy in noisy environment and has a lower computational complexity than methods that require Eigenvalue decomposition like MUSIC. It can estimate the magnitude of fault frequencies accurately unlike subspace-based methods like MUSIC, ESPRIT, etc. Spurious peaks are avoided as

the estimator doesn't require the information about the number of sinusoids. This decreases the chance of false-alarms and missed detections. Different performance indices of the spectral estimator are evaluated with POR. Along with this, the accuracy of the method is also compared with MUSIC and the classical method of DFT. It was found that the accuracy of the proposed method is comparable to MUSIC and its computational complexity is also much than MUSIC. Additionally, amplitude of sinusoidal components are estimated accurately with this method. Taking the advantages into consideration, this method is found more suitable for fault detection. To further improve the resolution capacity, a method of frequency band shifting followed by re-sampling for spectral analysis popularly known as 'zooming' technique can also be adopted.

CHAPTER 3

Development of the Real-time SCIM Fault Simulator

Fault modeling is essential for testing the developed condition monitoring system of the SCIMs. This helps in generating conditions that are difficult to emulate in experimental setup and hence can be used to test and validate the fault detector under different operating conditions. The aim of this chapter is to design a Real-Time (RT) fault simulator of the induction motor from existing mathematical models instead of concentrating on developing the mathematical model itself. In this chapter, a brief introduction to the modeling technique is followed by its RT implementation. The simulator is validated using frequency domain signature analysis of the stator current. The frequency domain analysis is carried out with the spectral estimator proposed in the previous chapter.

3.1 Modeling Technique

An SCIM can be mathematically modeled by three methodologies. These techniques can be briefly classified into:

i. The simplified **DQ Axis model**. This model was initially developed for RT simulation. It finds its application in the estimation of speed and fundamental frequency. In this method, it is assumed that the windings are sinusoidally distributed. As a result, dynamic simulation with arbitrary winding is not possible.

ii. Detailed modeling through **Coupled Circuit Modeling (CCM)** technique finds its application in modeling of faults that are not possible in the DQ axis model. This

method is implemented in RT environment for dynamic simulation of different rotor faults of the SCIM.

iii. **Finite Element Modeling (FEM)** is the most accurate technique, but its RT implementation is challenging.

For developing the RT simulator, modeling was carried out with CCM technique and was developed in SIMULINK. Various faults that arise in an actual motor under different operating conditions can be incorporated in this model. This modeling technique is based on winding function approach that can be used for any arbitrary winding layout. The parameters of the motor are derived from geometry and the winding arrangement. An embedded platform is developed for implementation of the fault simulator. This platform is loaded with the DOS based RT kernel from Mathworks popularly knows as Simulink Real-time (SLRT). The mathematical model is developed in SIMULINK and an executable code is generated from it. Once generated, the executable code was run on a RT platform. Different fault signatures were produced for all the faults with the motor running under different operating conditions.

RT simulation models for BRB, BER, and eccentricity faults have been developed, implemented and verified with the standard motor signature. The model is found to be fully functional for all the three type of eccentricity faults: the static, the dynamic and the mixed conditions. Spectral analysis of the stator current is carried out to verify the models. A brief overview of CCM techniques [85] is given below.

It is assumed that the motor has m stator circuits and n rotor bars. The model of the induction motor can be described by the following relations in matrix-vector format.

$$\begin{aligned} V_s &= R_s I_s + \tfrac{d\Lambda_s}{dt} \\ \Lambda_s &= L_{ss} I_s + L_{sr} I_r \\ V_r &= R_r I_r + \tfrac{d\Lambda_r}{dt} = 0 \\ \Lambda_r &= L_{rs} I_s + L_{rr} I_r \end{aligned} \tag{3.1}$$

where V_s is the supply voltage vector, I_s is the stator current vector, and I_r is the rotor current vector. Λ_s is the stator flux and Λ_r is the rotor flux. L_{ss} is the stator self inductance, L_{rr} is the rotor self inductance, and L_{sr} and L_{rs} are the stator-rotor and rotor-stator mutual inductances. Also,

$$\begin{aligned} I_s &= [i_{s1}, i_{s2}, i_{s3}, ..., i_{sm}]^T \\ I_r &= [i_{r1}, i_{r2}, i_{r3}, ..., i_{rn}]^T \\ V_s &= [v_{s1}, v_{s2}, v_{s3}, ..., v_{sm}]^T \end{aligned} \tag{3.2}$$

where i_{si}, i_{ri}, v_{si} represents the ith phase stator current, the rotor current of the ith bar, and ith phase supply voltage respectively. The inductances are calculated with the winding

functions [86, 87, 88]. According to the winding theory, the mutual inductance between windings i and j is given by

$$L_{ij}(\phi) = \mu_0 L_0 r_0 \int_0^{2\pi} g_0^{-1}(\phi,\theta) N_i(\phi,\theta) N_j(\phi,\theta) d\theta \tag{3.3}$$

where, ϕ is the angular position of the rotor w.r.t a stator reference, θ is a particular angular position along the stator inner surface, g_0^{-1} is the inverse air-gap function, L_0 is length of the stack, r_0 is the average radius of air-gap and $N_i(\phi,\theta)$ is the winding function. This is effectively the Magneto Motive Force (MMF) distribution along the air-gap for a unit current in i.

3.2 Implementation of the Real-Time SCIM Simulator

The motor model is designed with one mother program that automatically executes all its sub-models at runtime. During the compilation stage, the initialization process is initiated by the host computer in the non-RT environment. It requires the motor parameters (given in Table 3.1) to be provided as input along with the type of fault(s) present. In this stage, the inductance and resistance matrices containing all fault information are calculated from different sub-models with the given initial condition. A general block diagram of the system is shown in Fig. 3.1. This block diagram can be considered as the top most level of abstraction of the simulator.

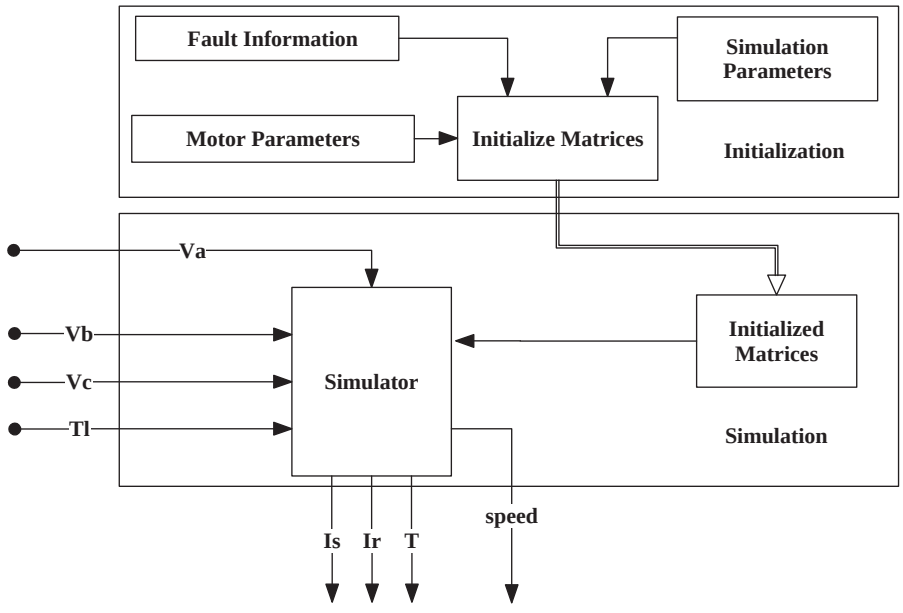

Figure 3.1: Top most level of abstraction for designing the realtime simulator

Table 3.1: Technical specification and parameters of the simulated Induction Motor

Sl. No.	Parameter	Value
1	Power	11 kW
2	No. of Phases	3
3	Supply Voltage	230v
4	No. of Rotor Bars	40
5	No. of stator slots	48
6	No. of pole pairs	2
7	Length of stack	0.11
8	No. of stator winding turns	28
9	No. of coils per phase per pole pair	4
10	Average air gap radius	0.0008
11	Stator resistance per phase	1.75
12	Resistance of each rotor bar	3.1×10^{-5}
13	Resistance of each end ring	2.2×10^{-6}
14	Lls	0.0064
15	Inertia	0.0754
16	B	0.001
17	Lbr	9.5×10^{-10}
18	Ler	1.8×10^{-10}
19	Angle of Skewing	$\pi/6$
20	Slot Opening	$\pi/86$

The motor model involves creating 3D matrices in the initializing stage and accessing them in the simulation phase. Global data store memory blocks were used for this purpose. Once all the matrices are computed, an executable with the required parameters and matrices are transferred to the target computer for RT execution. The simulation stage sub-model is generic in nature and independent of the presence of any faults.

RT simulation involves integration. Individual approximation models are present in the literature [87]. Instead of numerical integration, the integrand of the approximation model was solved analytically, and a simple algebraic equation is formulated. During execution, this algebraic function is solved with input parameters instead of numerical integration. Simulated data were recorded in the target computer and were accessed by the host machine for validation using MATLAB. Stator current for different fault conditions were recorded and then their frequency spectrum is evaluated. A simulation time step size of 0.0001 seconds was used for the RT simulation. This is required for proper simulation of the eccentricity related faults as the signatures of these faults appear in the higher band. A brief overview of the algorithm is provided in Algorithm 1. Initially, both the initialization and simulation of the algorithm was carried out with SIMULINK model. The initialization involves complex computations as it generates different inductance matrices and their

derivatives for computing the flux. Using SIMULINK for this model limited the geometrical step-size to 1/10. Currently, the initialization is carried using MATLAB scripts. This led to much smaller geometrical step-sizes in the order of $2\pi/800$ for the RT simulation.

Algorithm 1 Real-Time SCIM Fault Simulator

```
Start
Read Data  ▷ /*This file provides the mechanical design and electrical properties of the
           motor. It also contains the information about the fault to be simulated
Start Initialization
Fix geometrical step size, θ = 0 : 0.1 : 2π
if Eccentricity present then
    Compute L_rr,L_rs,L_sr,L_ss for each θ index of motor with eccentricity.
else
    Compute L_rr,L_rs,L_sr,L_ss for each θ index of motor without eccentricity.
end if
if BRB and BER present then
    Modify L_rr,L_rs,L_sr,R_rr for each θ index for BRB.
end if
Declare and initialize k and set θ[k] = 0, i[k] = 0
End Initialization
Start Simulation
Set simulation time (t_final), sample time (Ts)=0.0001
while t ≺ t_final do
    Calculate V_s(t), Λ_s(t), and Λ_r(t) using (3.1)
    Compute I_s(t), θ(t), T_e(t)
    t = t + Ts
end while
End
```

From the schematic diagram of Fig. 3.1 it is observed that all the input and output interfaces are handled by the primary motor model. This model is simulated with the required parameters under healthy and various faulty conditions. Fault specific harmonics in the spectrum of the stator current is used to verify the presence of different frequency components that are characteristic of a particular fault. The data is stored at a rate of 10000 samples/s. A screenshot from the target running in RT with healthy motor is shown in Fig. 3.2.

3.3 Validation of the Proposed Fault Simulator

Spectral analysis of the stator with proposed spectral estimator (discussed in Chapter 2) is carried out for validation of the simulator. The stator current signal, along with speed and the generated torque are stored. The mean value of speed is used for calculating the slip. The slip is eventually used for searching in specific frequency bands for fault signatures. The spectral signature thus obtained is validated with the theoretical values obtained from

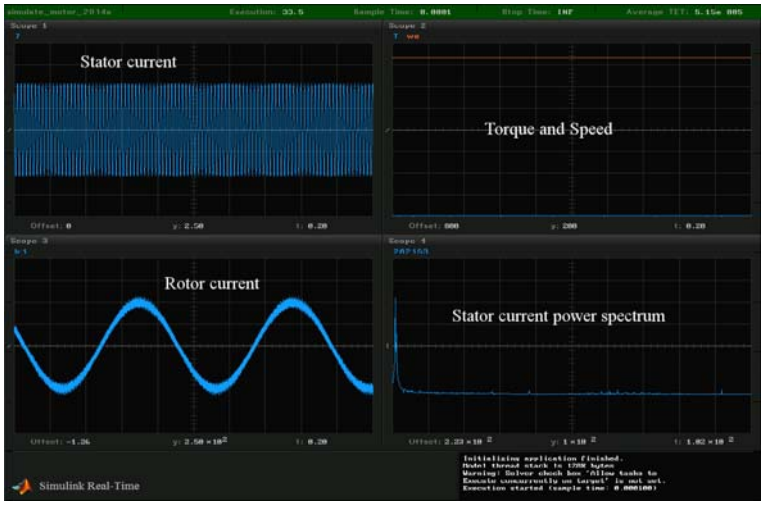

Figure 3.2: SLRT target screen of simulation of a healthy motor

the literature that were discussed in Chapter 1. Some of the frequency components that are used for this purpose is given in Table 1.1. For the faults that have the frequency components in the lower bands as in BRB, BER, and mixed eccentricity, the data is down-sampled by a factor of 50 units for better resolution. The effective sample rate comes down to 200 samples/s. The search space is fixed between 45 Hz to 55 Hz for BRB and BER faults. Whereas, for mixed eccentricity fault, the search band is fixed between 25 Hz to 27 Hz. For static and dynamic eccentricity, the down-sampling rate is restricted to 4 units. As a result, the effective sampling rate is 2500 samples/s. The search space is fixed between 600 Hz to 1200 Hz for static and dynamic eccentricity. The value of L is set to 2048 units for all situations.

Fig. 3.4 shows the stator current, speed, and the stator current spectrum of a healthy motor, w.r.t BRB, and BER faults for three different loads. It can be seen from the start-up current characteristics, that, the simulated motor replicates the real motor. It is to be noted that the simulated motor is direct online started with three phase input. As a result, the steady state value is reached very fast. The stator spectrum is used to draw a comparison between the fault cases. It is observed, how the settling time of speed varies with that of the load. Fig. 3.5 shows the motor characteristics for the motor with BER, BRB, and double BRB faults running with 2.8% load. It is observed that the fault give rise to its specific components even under light loads. Although, it is not very prominent for the BER fault due to the presence of other prominent components. In Fig. 3.4, the healthy motor gave frequency peaks in the observed band, but the components are not concerned with this class of faults and the magnitude is also very small when compared to the faulty simulated motor running with the same load. The simulator has successfully simulated the case of increased level of fault with increased spectral magnitude as observed in the 'double BRB' case. The

magnitude of the fault component in the stator current spectrum increases with increased loading. Fig. 3.6 shows the effect of increased loading on the simulated motor with BRB and BER faults. It is observed that the fault components move away from the fundamental component due to increased loading and there is an increase in magnitude of fault specific frequency components. From the stator current, it is found how it is modulated in the presence of a fault.

Successful simulation of the a motor with eccentricity fault depends on the accurate evaluation of different inductances. The Presence of eccentricity faults modifies the inductances. Fig. 3.7 shows the change in the mutual inductance between stator phase 'A' and rotor bar one with different faults for one complete rotation.

Simulation of the motor without eccentricity are presented in Fig. 3.8 - Fig. 3.10 to differentiate between healthy and faulty cases. Simulation of faulty and healthy motors for eccentricity were carried out with two classes of motor having different rotor bars (R) while keeping the other parameters same. This leads to the simulation of situations described by (1.4). Fault signatures of mixed eccentricity fault manifests in a low and a high frequency band. As a result, simulation results of eccentricity are ascertained by observing these bands. Fig. 3.8 presents the high-frequency components with $R = 40$, running under different loads. Fig. 3.9 shows the high-frequency components with $R = 41$, with separate loads. Changing the value of R from 40 to 41 results in additional peaks in the spectrum. It is also seen, that, the quantity as well as the magnitude of the frequency components decrease with increased loading for both the simulated motors. This phenomenon is more prominent with $R = 41$. Fig. 3.10 shows the low-frequency spectrum of a healthy motor with different rotor bars and load. It is observed from this figure, that, the spectral peaks are confined to low-amplitude regimes and is lowest for $R = 41$. The visible peaks in the spectrum do not abide by the eccentricity condition given by (1.5) due to the absence of mixed eccentricity.

Fig. 3.11 - Fig. 3.13 presents the results for the simulated motor running under different conditions of static eccentricity fault. Fig. 3.11 demonstrates the stator current, the speed, and the spectrum of the stator current for the motor simulated with 40% static eccentricity, $R = 40$, and 2.8% load. Similarly, Fig. 3.12 shows the results for the motor running with 10% static eccentricity, $R = 41$, and 2.8% load. Fig. 3.13 exhibits the high frequency spectrum for the motor with $R = 41$, and 40% static eccentricity under different loading conditions. With 10% eccentricity, the faults components are not distinguishable for $R = 41$. Similarly, for the motor with $R = 40$ and 40% eccentricity, the components are not distinguishable from the healthy case. This conforms to the conditions reported in [2]. In case of the motor with $R = 41$ and 40% eccentricity, there are visible components related to eccentricity fault. It is also observed, that, these components are suppressed with increased loading. Fig. 3.14 - Fig. 3.16 presents the results for the simulated motor running under different conditions of dynamic eccentricity faults. Fig. 3.14 shows the stator current, the speed, and the spectrum of the stator current for the motor simulated with 40% dynamic

eccentricity, $R = 40$, and 2.8% load. Similarly, Fig. 3.15 demonstrates the results for the motor running with 10% dynamic eccentricity, $R = 41$, and 2.8% load. Fig. 3.16 exhibits the high-frequency spectrum for the motor with $R = 41$, and 40% dynamic eccentricity under different loading conditions.

It is to be noted, that, the high-frequency component of these two faults are prominent only under light load conditions and are difficult to isolate from the healthy case under such conditions. The only discriminating factors are light changes in magnitude and location of frequency components. With $R = 41$, the appearance of the low-magnitude components can distinguish but only under very light load conditions.

Mixed eccentricity faults give rise to additional low-frequency components as defined by (1.5) in the stator current spectrum other than the high-frequency components attributed to static and dynamic eccentricity. These components are only present when both static and dynamic faults are present. Fig. 3.17 shows the stator current, low-frequency components, and the high-frequency components for the motor with $R = 40$, 10% static and 10% dynamic eccentricity, operating under 2.8% load. Fig. 3.18 presents the stator current, low-frequency components, and the high-frequency components for the motor with $R = 41$, 10% static and 10% dynamic eccentricity, and 2.8% load. When compared to the healthy motor stator current spectrum, it is observed that the low-frequency components can distinguish between the healthy and faulty cases very easily. Whereas, the high frequency components have a minuscule difference. Fig. 3.19 exhibits the low-frequency components for a motor with $R = 41$, and 25% static and 40% dynamic eccentricity with different loads. The peak frequency conforms to (1.5), and its magnitude decreases with increasing load.

A screenshot from the target running in RT with a faulty motor is shown in Fig. 3.3.

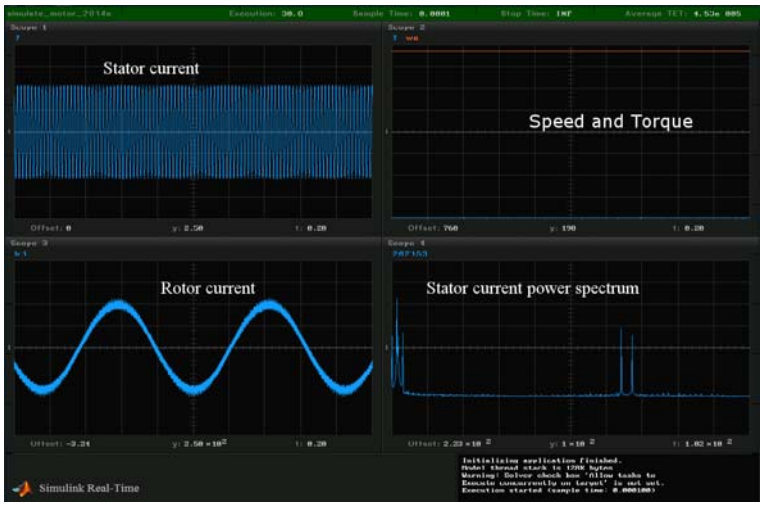

Figure 3.3: SLRT target screen of a faulty model, running with single BRB

3.4 Summary

This chapter dealt with the development of an RT SCIM fault simulator. This simulator was implemented on a hardware, and various parameters were recorded for the analysis. The spectral estimator developed in Chapter 2 was utilized for determining the fault frequency features of the motor simulated with different faults. These features were found to be in agreement with the theoretical components. It was also shown, how the magnitude of the fault components depend on the loading and the degree of the fault present. Inherently, motors contain some amount of mixed eccentricity fault, and the low-frequency component is found to be most suitable for detection of eccentricity faults. Moreover, the low-frequency component can discriminate between healthy and faulty cases with high accuracy due to large variation in the magnitude of the fault components. However, this component is suitable only for motors with mixed eccentricity conforming the the designated rotor bar and pole pair relation. Using the analog output of the simulator, any of its available signal can be sent to the condition monitoring system. This is useful for RT testing and validation of the fault-condition monitoring system.

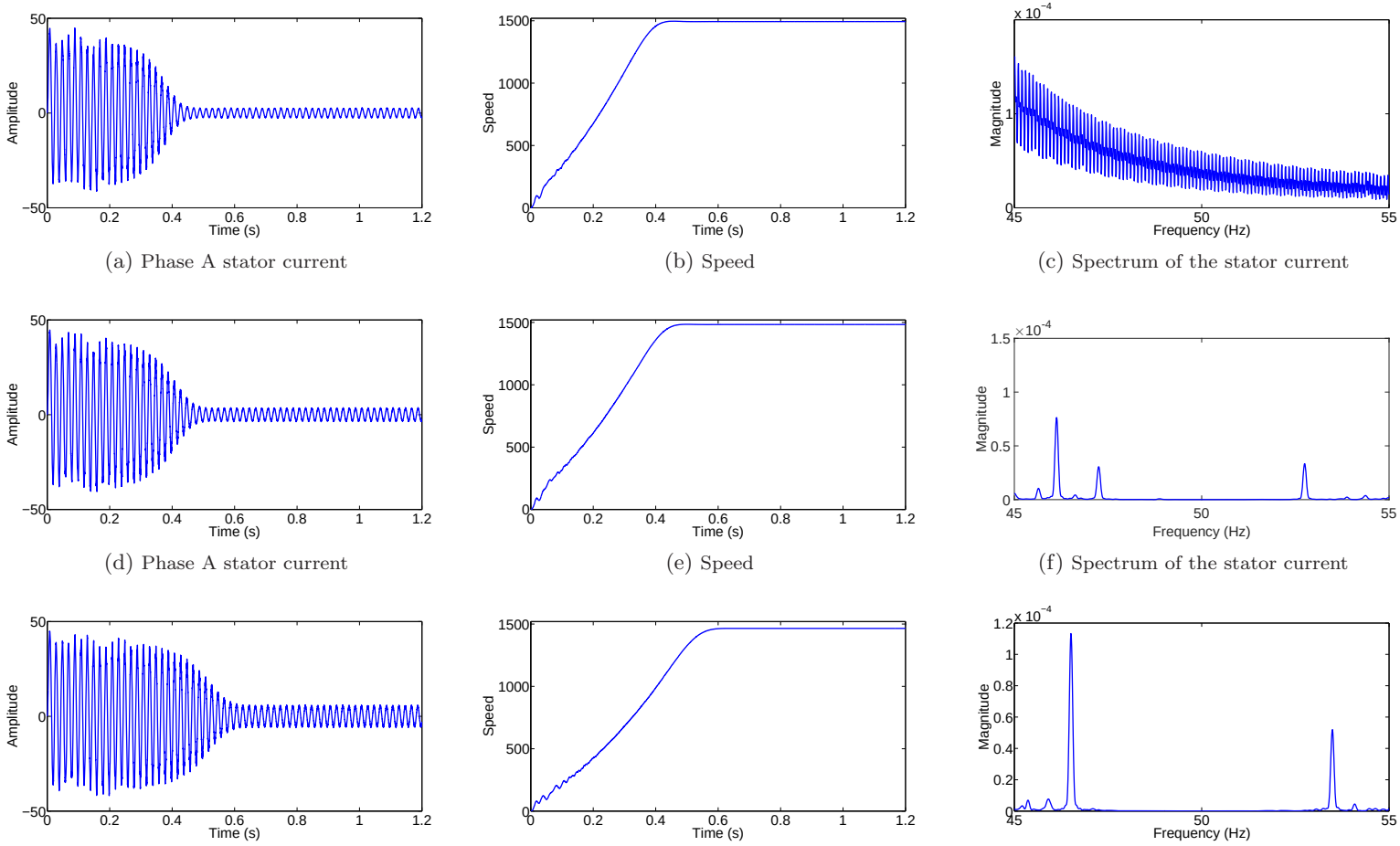

(a) Phase A stator current (b) Speed (c) Spectrum of the stator current

(d) Phase A stator current (e) Speed (f) Spectrum of the stator current

(g) Phase A stator current (h) Speed (i) Spectrum of the stator current

Figure 3.4: Healthy Motor running with (a)-(c) 2.84% load, (d)-(f) 7.05% load, and (g)-(i)13.94% load

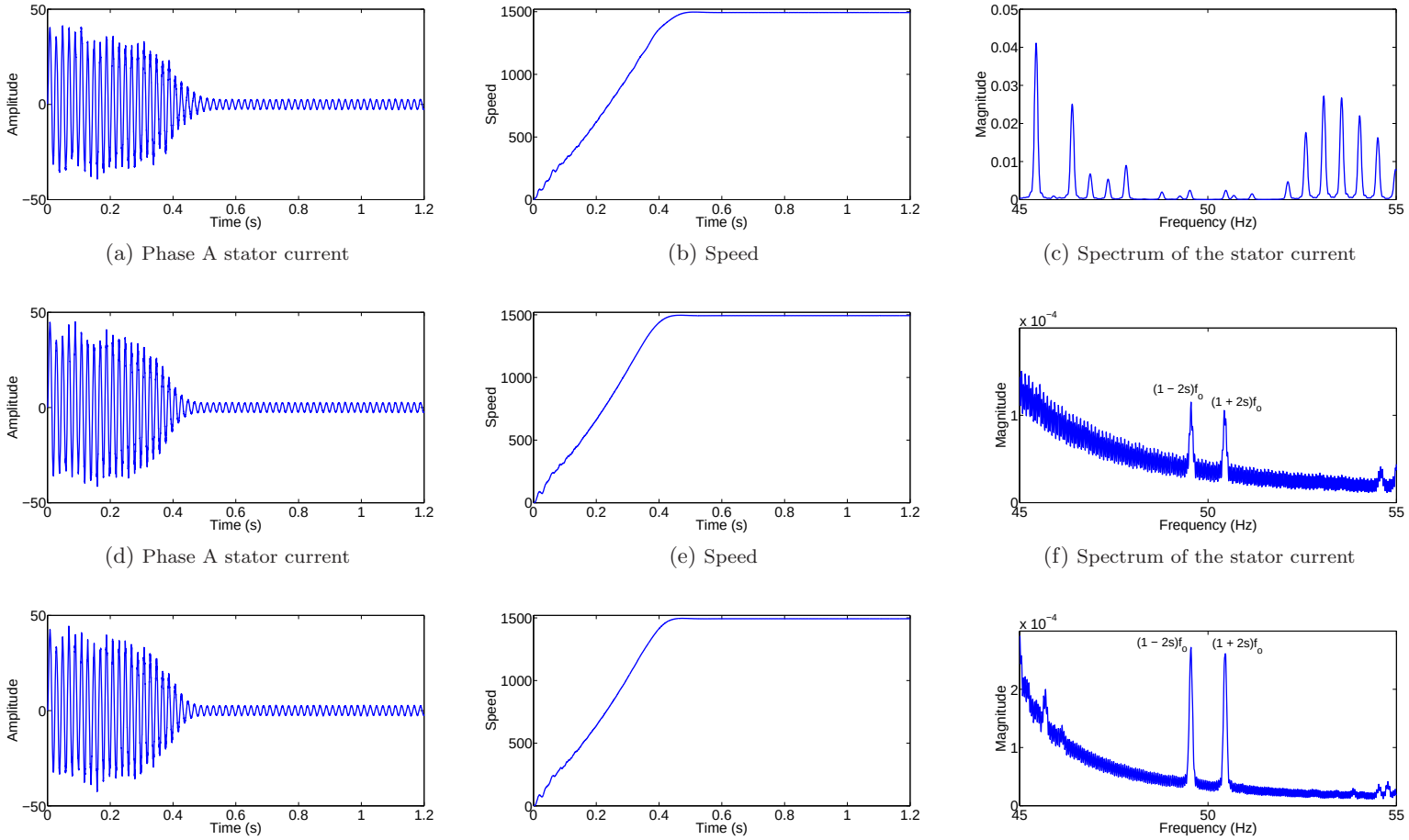

(a) Phase A stator current (b) Speed (c) Spectrum of the stator current

(d) Phase A stator current (e) Speed (f) Spectrum of the stator current

(g) Phase A stator current (h) Speed (i) Spectrum of the stator current

Figure 3.5: Motor running with (a)-(c) broken end ring, (d)-(f) single broken rotor bar, and (g)-(i) two broken bars, and with 2.8% load for all the faults

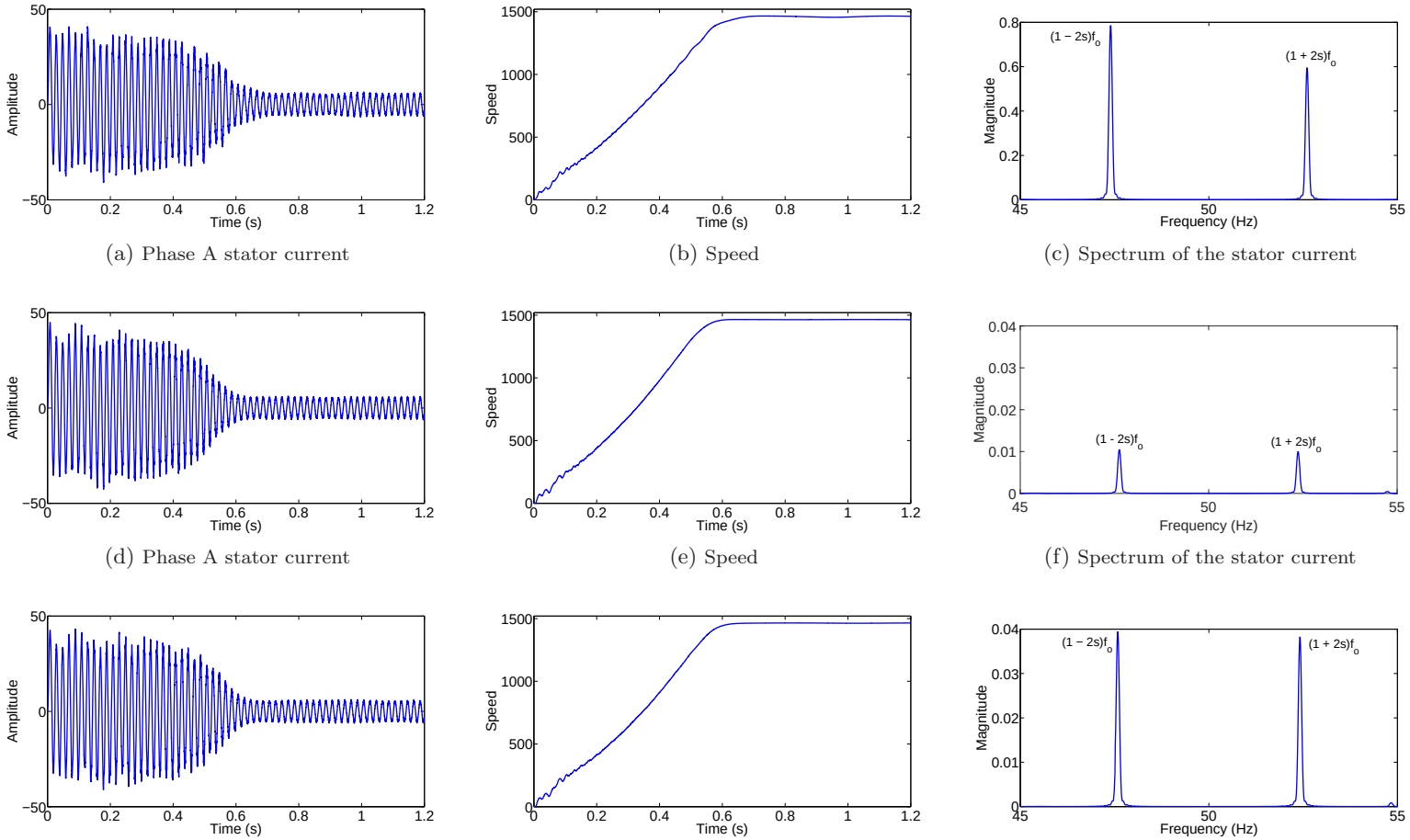

(a) Phase A stator current (b) Speed (c) Spectrum of the stator current

(d) Phase A stator current (e) Speed (f) Spectrum of the stator current

(g) Phase A stator current (h) Speed (i) Spectrum of the stator current

Figure 3.6: Motor running with (a)-(c) broken end ring, (d)-(f) single broken rotor bar, and (g)-(i) two broken bars, and with 14% load for all the faults

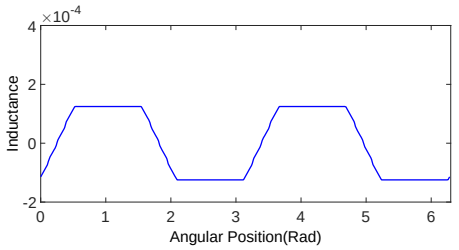

(a) Motor with no eccentricity

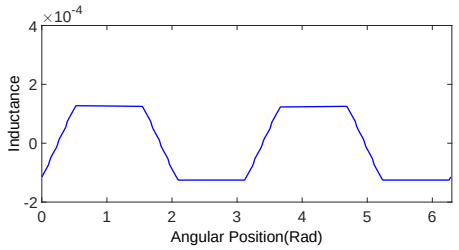

(b) Motor with 10% static eccentricity

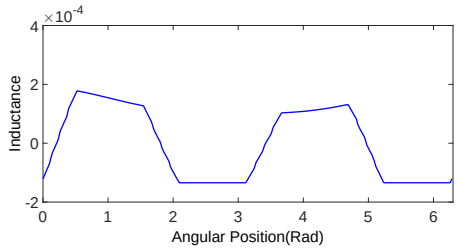

(c) Motor with 40% static eccentricity

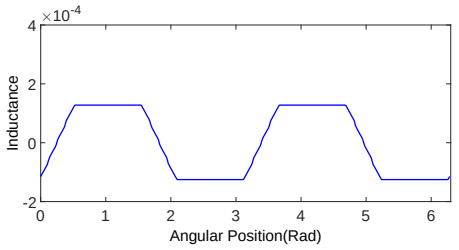

(d) Motor with 10% dynamic eccentricity

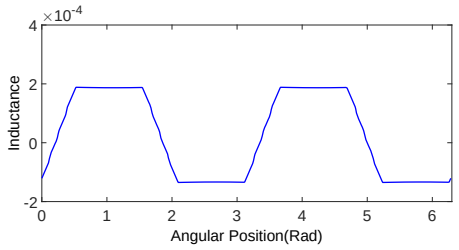

(e) Motor with 40% dynamic eccentricity

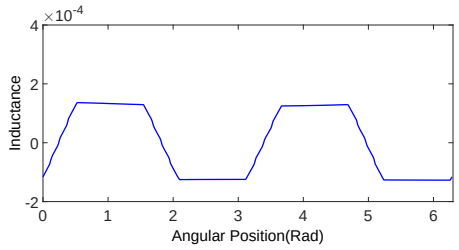

(f) Motor with mixed eccentricity (10% static and 10% dynamic)

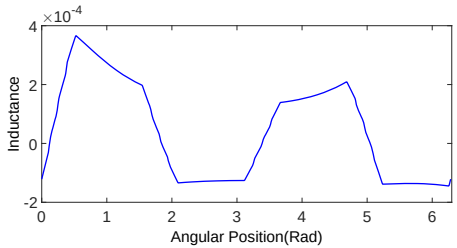

(g) Motor with mixed eccentricity (25% static and 40% dynamic)

Figure 3.7: Mutual inductance between stator phase A and rotor bar one

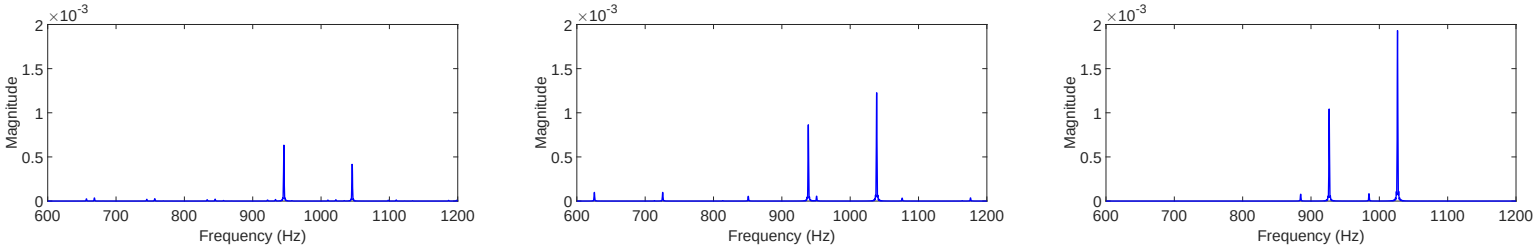

(a) 2.84% load (b) 7.05% load (c) 13.94% load

Figure 3.8: High frequency components of stator current spectrum with no eccentricity faults and $R = 40$

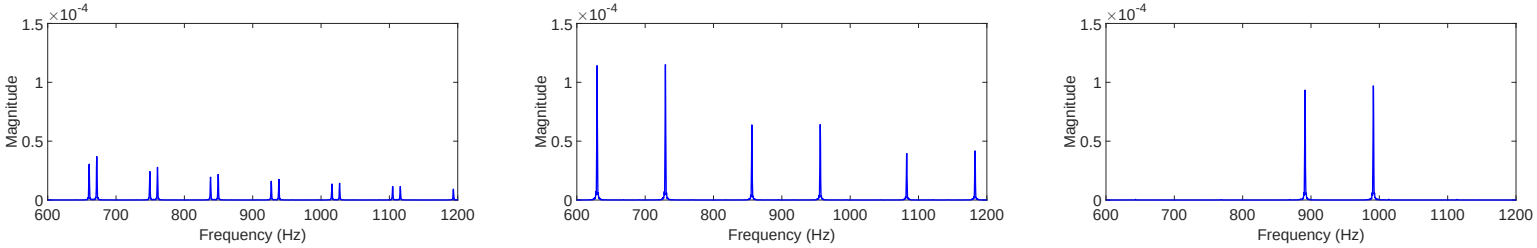

(a) 2.84% load (b) 7.05% load (c) 13.94% load

Figure 3.9: High frequency components of stator current spectrum with no eccentricity faults and $R = 41$

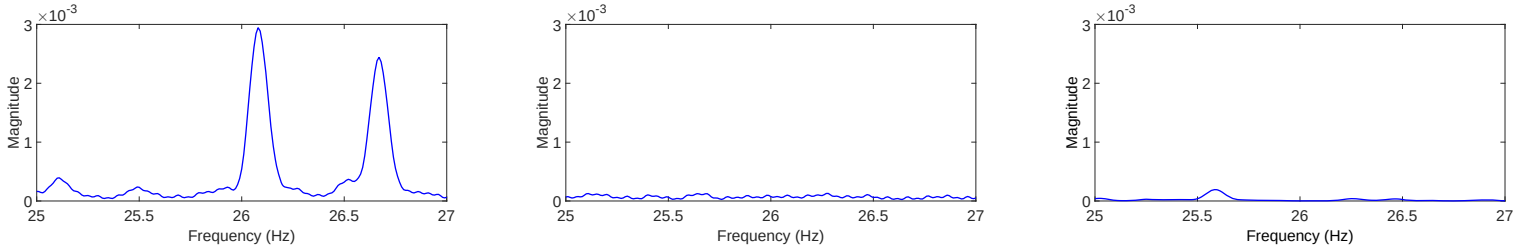

(a) 2.84% load, $R = 40$ (b) 2.84% load, $R = 41$ (c) 13.94% load, $R = 41$

Figure 3.10: Low frequency components of stator current spectrum with no eccentricity faults

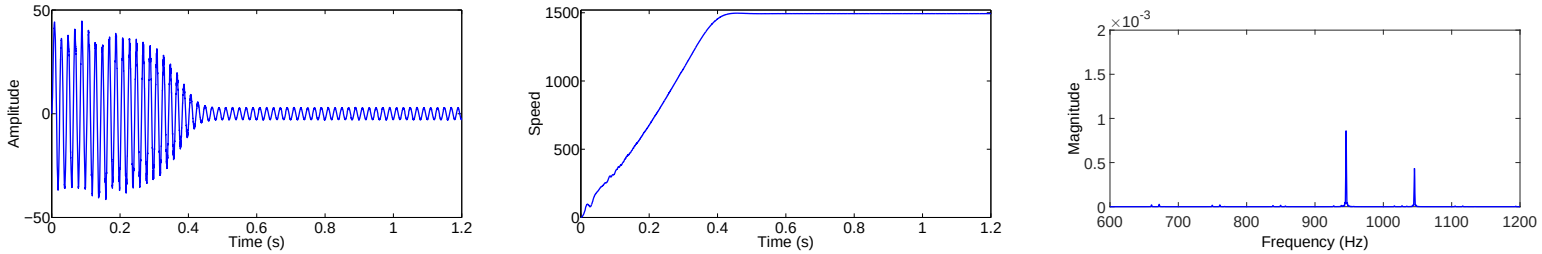

(a) Phase A stator current (b) Speed (c) Spectrum of the stator current

Figure 3.11: Motor running with 2.8% load for 40% static eccentricity and $R = 40$

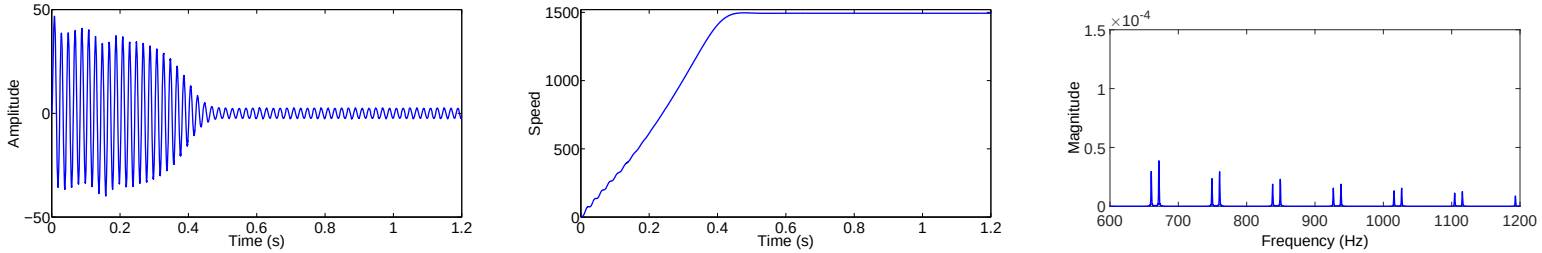

(a) Phase A stator current (b) Speed (c) Spectrum of the stator current

Figure 3.12: Motor running with 2.8% load for 10% static eccentricity and $R = 41$

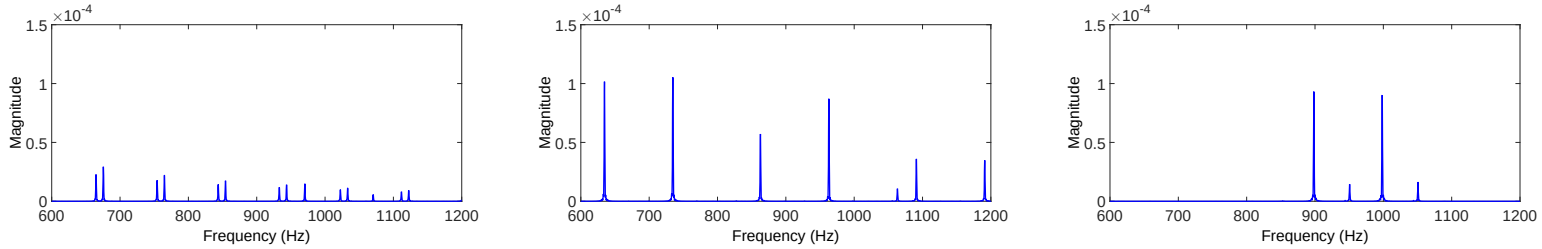

(a) 2.8% load (b) 7.05% load (c) 13.94% load

Figure 3.13: Spectrum of the stator current of motor(R = 41) running with 40% static eccentricity with different loads

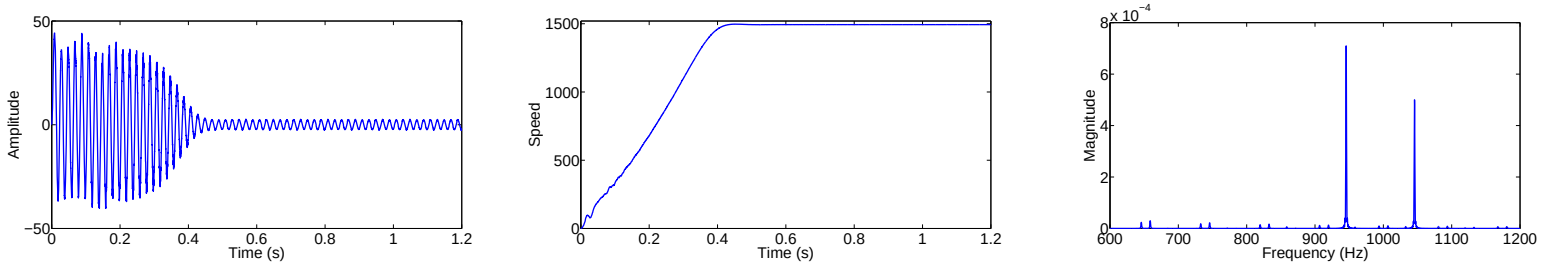

(a) Phase A stator current (b) Speed (c) Spectrum of the stator current

Figure 3.14: Motor running with 2.8% load for 40% dynamic eccentricity and $R = 40$

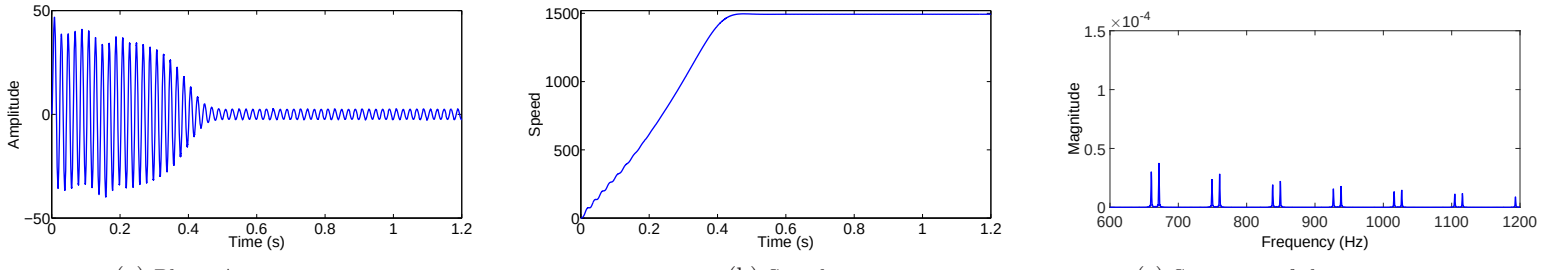

(a) Phase A stator current (b) Speed (c) Spectrum of the stator current

Figure 3.15: Motor running with 2.8% load for 10% dynamic eccentricity and $R = 41$

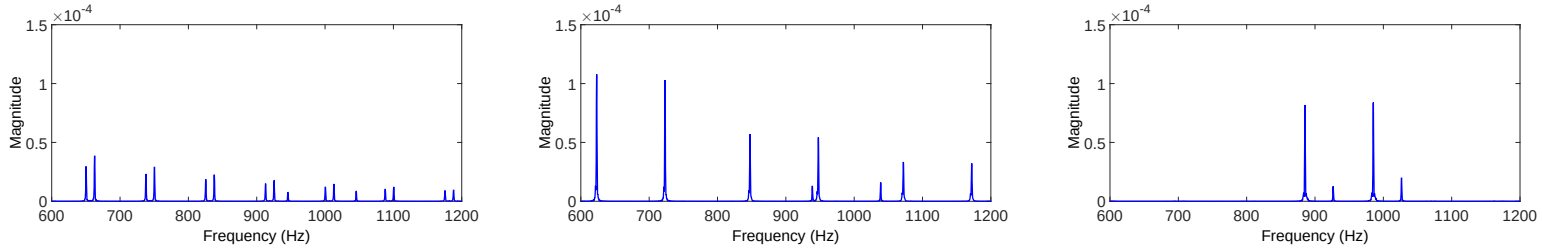

(a) 2.8% load (b) 7.05% load (c) 13.94% load

Figure 3.16: Spectrum of the stator current of motor ($R = 41$) running with 40% dynamic eccentricity with different loads

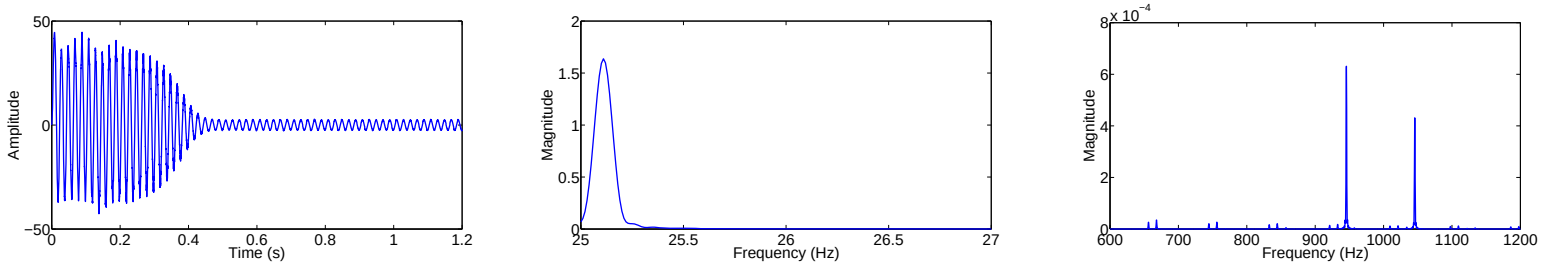

(a) Phase A stator current (b) Low frequency components (c) High frequency components

Figure 3.17: Motor running with 2.8% load for mixed eccentricity (10% static and 10% dynamic) with $R = 40$

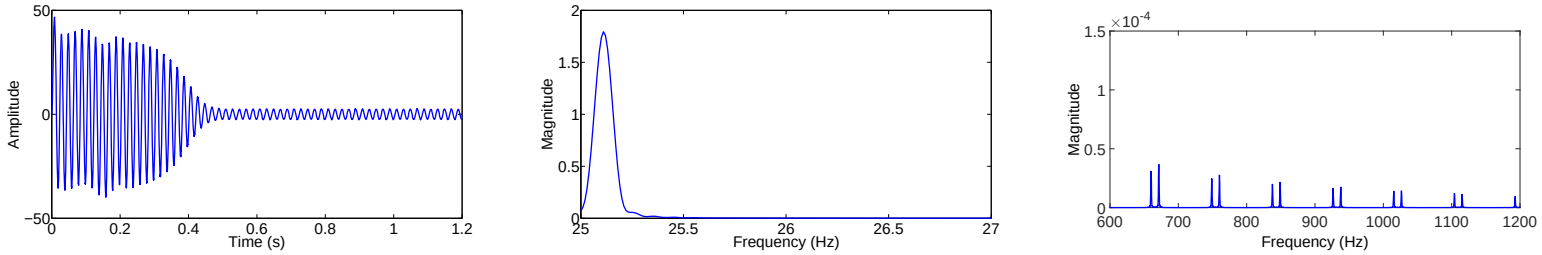

(a) Phase A stator current (b) Low frequency components (c) High frequency components

Figure 3.18: Motor running with 2.8% load for mixed eccentricity (10% static and 10% dynamic) with $R = 41$

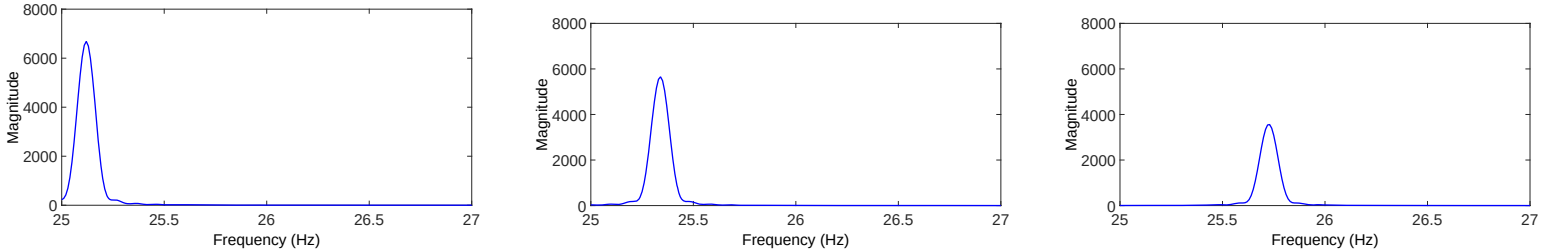

(a) 2.8% load (b) 7.05% load (c) 13.94% load

Figure 3.19: Spectrum of the stator current of motor ($R = 41$) running with mixed eccentricity (25% static and 40% dynamic) with different loads

CHAPTER 4

Induction Motor Weak Fault Detection Algorithm

The aim of this chapter is to develop efficient, reliable, and fast algorithms to detect weak and incipient faults in SCIMs and assess their severity. A schematic block diagram to illustrate the working of the condition monitoring algorithm is shown in Fig. 4.1. The 'Parameter Estimation' block estimates different parameters of the motor like supply frequency, speed, and slip. This block also contains the signal conditioning unit that removes the fundamental frequency from the input stator current for better detectability. The estimated fundamental frequency along with the slip is used for creating spectral search bands. The 'fault detection algorithm' block in Fig. 4.1 estimates the spectrum in the designated search bands and also estimates the relative amplitude of frequency components. The spectral amplitude is used by the 'decision module' to assess the severity of the fault. These modules together help in the detection of weak faults under variable load and supply frequency conditions. The algorithm is capable of detecting faults under load condition when the concerned faults are difficult to detect. The experiments and data analysis for BRB and mixed eccentricity were carried on a 22 kW induction motor experimental setup discussed in this chapter.

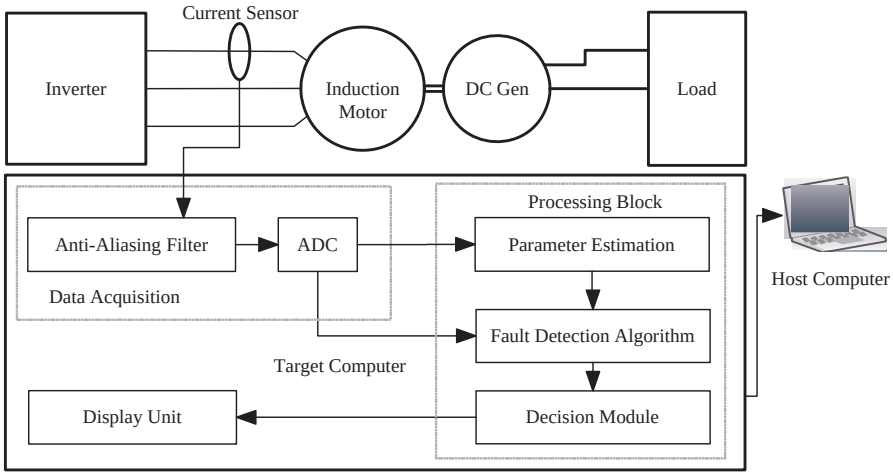

Figure 4.1: The complete fault-condition monitoring system

4.1 Signal Conditioning and Fundamental Frequency Estimator

Extended Kalman Filter (EKF) based fundamental frequency estimation system is designed according to [89]. This method tracks the fundamental frequency component that is essential for forming the spectral search bands for identifying the fault frequency components. It also estimates the instantaneous magnitude of fundamental component, which is subsequently deducted from the input signal. As a consequence, the condition of the input signal is improved, and detectability of weak amplitude sidebands close to the fundamental is enhanced without using any notch filter.

In this method, it is assumed that the amplitude of the frequency components other than the fundamental is negligible. The assumption is valid because the magnitude of the fundamental component of the stator current is very high compared to the fault frequencies in incipient stages. Hence, the signal is considered to be solely composed of the fundamental frequency (f_o) with additive noise of zero mean. The kth sample of the signal is given by

$$y_k = A_o \cos(k\omega_o + \phi_o) + \varepsilon_k \tag{4.1}$$

where A_o, ω_o, and ϕ_o are the amplitude, angular frequency, and phase of the fundamental component and ε_k is the additive zero-mean noise. ω_o is given by $2\pi f_o/F_s$, and F_s is the sampling frequency with which the measurement is sampled.

$$y_k = \hat{y}_k + \varepsilon_k \tag{4.2}$$

With $\hat{y}_k$ being the estimated signal. This signal can be described by an autoregressive signal model where the present sample is defined by past two samples according to the relation

$$\hat{y}_k = 2\cos(\omega_o)\hat{y}_{k-1} - \hat{y}_{k-2} \tag{4.3}$$

The state vector is defined as

$$\hat{x}_k = [2\cos(\omega_o) \quad \hat{y}_{k-1} \quad \hat{y}_{k-2}]^T \tag{4.4}$$

Propagating the state from k to $(k+1)$th instant we need $\hat{x}_{k+1}$, which is given by

$$\begin{aligned} \hat{x}_{k+1} &= [2\cos(\omega_o) \quad \hat{y}_k \quad \hat{y}_{k-1}]^T \\ \text{or, } \hat{x}_{k+1} &= \begin{bmatrix} 1 & 0 & 0 \\ 0 & 2\cos(\omega_o) & -1 \\ 0 & 1 & 0 \end{bmatrix} \hat{x}_k \end{aligned} \tag{4.5}$$

The measurement equation is given by

$$y_k = \begin{bmatrix} 0 & 2\cos(\omega_o) & -1 \end{bmatrix} \hat{x}_k + \varepsilon_k \tag{4.6}$$

The state and measurement equations are nonlinear function of the state and are represented as a function of the state vector by

$$\begin{aligned} \hat{x}_{k+1} &= f(\hat{x}_k) \\ y_k &= g(\hat{x}_k) + \varepsilon_k \end{aligned} \tag{4.7}$$

where using (4.5) we get,

$$f(\hat{x}_k) = \quad [2\cos(\omega_o) \quad 2\cos(\omega_o)\hat{y}_{k-1} - \hat{y}_{k-2} \quad \hat{y}_{k-1}] \tag{4.8}$$

and using (4.6), we get

$$g(\hat{x}_k) = 2\cos(\omega_o)\hat{y}_{k-1} - \hat{y}_{k-2} \tag{4.9}$$

Now, the states are propagated by using time and measurement updates using Kalman theory (see Fig. 4.2) [90], where the states are updated using the measurement input as given below

$$\hat{x}_k^+ = \hat{x}_k^- + K_k(y_k - H\hat{x}_k^-) \tag{4.10}$$

$()^-$ and $()^+$ denotes the pre and post measurement estimates respectively.

The time update is done by

$$\hat{x}_{k+1}^{-} = F\hat{x}_{k}^{+} \tag{4.11}$$

where $K_k = P_k^- H^T (HP_k^- H^T + 1)^{-1}$, with $P_k^- = FP_{k-1}^+ F^T$. F and H are the linearized form of $f(\hat{x}_k)$ and $g(\hat{x}_k)$ respectively and are given by

$$\begin{aligned} F &= \left.\frac{\partial f(\hat{x}_k)}{dx_k}\right|_{x_k = x_k^+} = \begin{bmatrix} 1 & 0 & 0 \\ x_k^+(2) & x_k^+(1) & -1 \\ 0 & 1 & 0 \end{bmatrix} \\ H &= \left.\frac{\partial g(\hat{x}_k)}{dx_k}\right|_{x_k = x_k^+} = \begin{bmatrix} x_k^+(2) & x_k^+(1) & -1 \end{bmatrix} \end{aligned} \tag{4.12}$$

The state error covariance $P_k^+$is given by

$$P_k^+ = (\mathbf{I} - K_k H) P_k^- (\mathbf{I} - K_k H)^T + K_k \sigma_v K_k^T \tag{4.13}$$

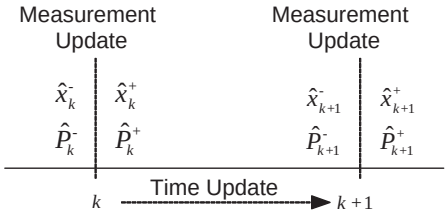

Figure 4.2: Propagation of states

The fundamental signal is estimated from (4.3), and the fundamental frequency is estimated from (4.4) by

$$\hat{f}_o = \frac{F_s}{2\pi} \cos^{-1}(\hat{x}_k^+(1)/2) \tag{4.14}$$

The scheme for signal conditioning by removal of the fundamental component is shown in Fig. 4.3.

The utility of this method is illustrated by plotting the spectrum of conditioned and unconditioned stator current in Fig. 4.4 and Fig. 4.5 respectively. It is observed, that, with EKF signal conditioning, the fundamental component is effectively suppressed Fig. 4.5. As a result, other closely spaced components specific to BRB faults are visible only in the conditioned signal. For this experiment, the current signal from the lab setup was used. The signal was sampled with 200 Samples/s. The spectral search was made in the 48-52Hz band for both the cases.

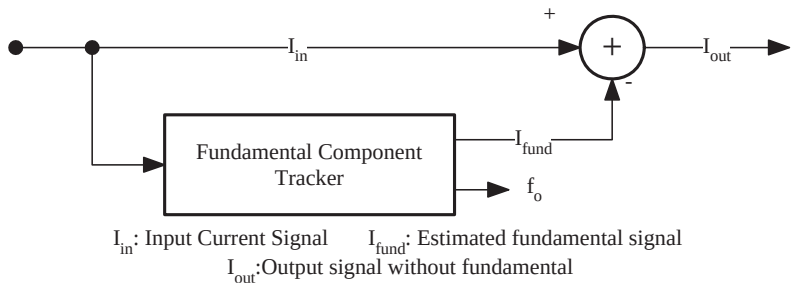

Figure 4.3: The signal conditioning unit.

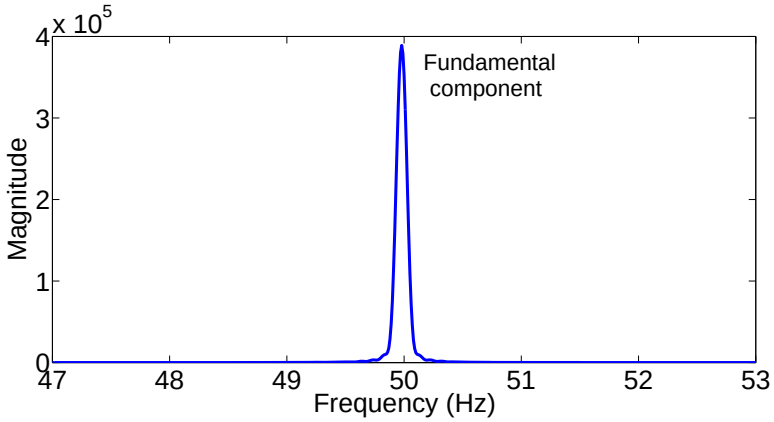

Figure 4.4: Spectrum of the unconditioned stator current

4.2 Estimation of Slip and Speed

Fault frequency components are motor slip dependent. For efficient detection of these fault components, estimation of speed is paramount to the fault diagnostic algorithm. Motor speed can be measured using a speed sensor or can be estimated using soft sensing techniques. Soft sensing techniques can be classified as observer-based [91, 92] and slot-harmonic-based [37, 93, 94, 95] methods. The observer based method requires the acquisition of all the phase voltages and currents. It also requires accurate estimates of some motor parameters that are difficult to evaluate and may change with time. The slot harmonics based methods requires searching for frequency components in high frequency bands. Now, for single-rate system design, the sampling frequency needs to be uniform. High sampling frequency would require longer time samples for resolving frequency components, compared to lower sampling rates. It was found that all the SCIMs used in this research carried an inherent mixed eccentricity component defined by

$$f_{mixed} = |1 \pm k(1-s)/p|\, f_o \tag{4.15}$$

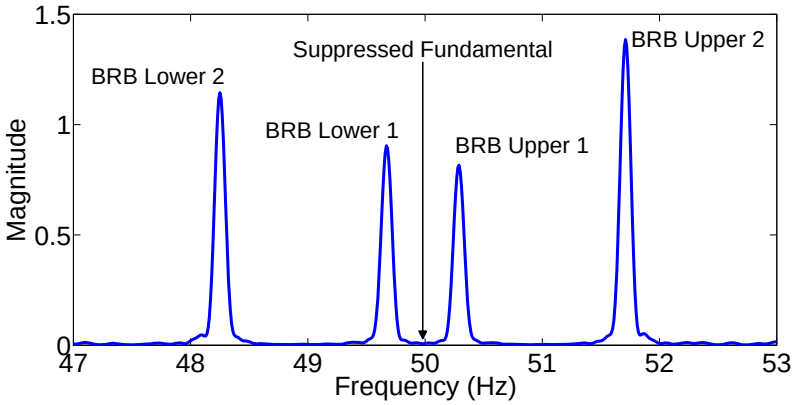

Figure 4.5: Effect of signal conditioning with EKF on the stator current spectrum

This component was present in the stator current spectra, even when all precautions were taken while assembling. Using the lower side band of (4.15), the slip is obtained by

$$s = 1 - \frac{(f_o - f_{mixed})}{f_o k} p \tag{4.16}$$

Putting $k = 1$ and $p = 2$ for the experimental motor, we get

$$s = \frac{2f_{mixed} - f_o}{f_o} \tag{4.17}$$

As the frequency component is limited to lower bands of the spectrum, detection of this frequency component is carried out to estimate the speed from the stator current with the same sampling rate as required for spectral estimation. The conditioned current signal is fed into this system. The spectral estimator in Chapter 2 is used for estimation of the frequency component. For this purpose, the spectral estimator is configured to search in the band of $0.5f_o$ to $0.6f_o$. This band was obtained from (4.17) with the slip ranging from 0% to 20% for the four-pole machine.

4.3 Relative Amplitude Estimation of Fault Frequency Components

Accurate knowledge of the magnitudes is essential to quantify the degree of fault. Some the fault detection algorithms reported in the literature use least square estimates for amplitude estimation [25]. However, these methods are of little use when the frequency components are closely spaced [80]. The proposed spectral estimator described in Chapter 2 is used to determine the amplitude of closely spaced frequency components by (2.26).

4.4 Effect of Windowing on Fault Detection

Windowing of the input signal prior to spectral estimation results in lower false alarms. However, it may result in diminished peaks and lower resolving power. Effect of windowing can be seen in Fig. 4.6. It is observed, that, the magnitude of the overall spectrum is diminished by a factor of approximately 100. In this work, a Chebyshev window was used.

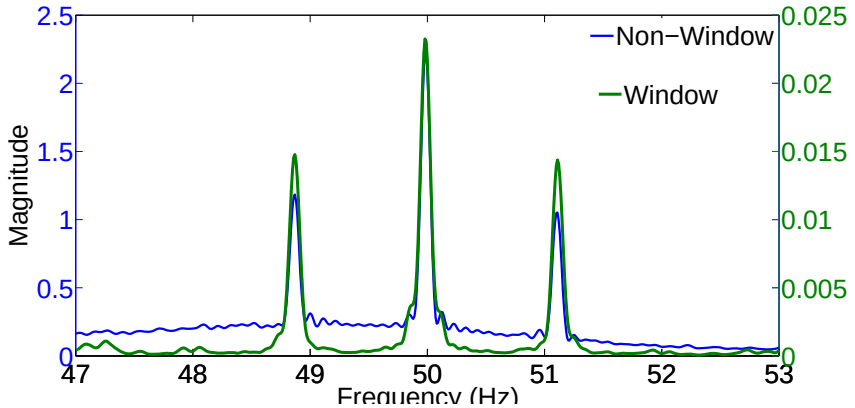

Figure 4.6: Effect of windowing on spectrum of stator current with BRB. Motor running with 43% load and 1.2% slip

4.5 The Experimental Setup

Experiments were carried out with a 22 kW, four-pole, and three-phase delta connected induction motor from ABB. Power to the motor is supplied with an ABB make variable frequency drive. Experiments were carried out for detection of weak faults. Variable loading is achieved through rheostatic loads, with a 24 kW separately-excited DC generator coupled to the motor as shown in Fig. 4.7. The load box for rheostatic loading can be seen in Fig. 4.8. Clamp-type Hall-effect sensors from Fluke (model: i1010s) were used to sense the current signal. Tests were performed in off-line as well as in online mode. For off-line data analysis, DL850v oscilloscope was used for data acquisition, with the analysis being performed in MATLAB environment. For Online mode, experiments were carried out with the system that will be discussed in Chapter 5. A front panel for the purpose of controlling the motor and acquiring the signals was designed and is shown in Fig. 4.9. From this panel, there is provision to change the supply frequency and the loading. Most of the parameters like RMS current, voltages, and speed can also be monitored through this panel. The experimental setup was used to validate BRB and mixed eccentricity condition. Data was acquired using the DL850v oscilloscope with a sampling rate of 20 kSamples/s. A higher sampling rate was chosen for creation of a standard database. For the analysis, this was

downsampled to 200 samples/s by a factor of 100. For this purpose, a low-pass filter was used to avoid aliasing. Each set of data was recorded for approximately 30s.

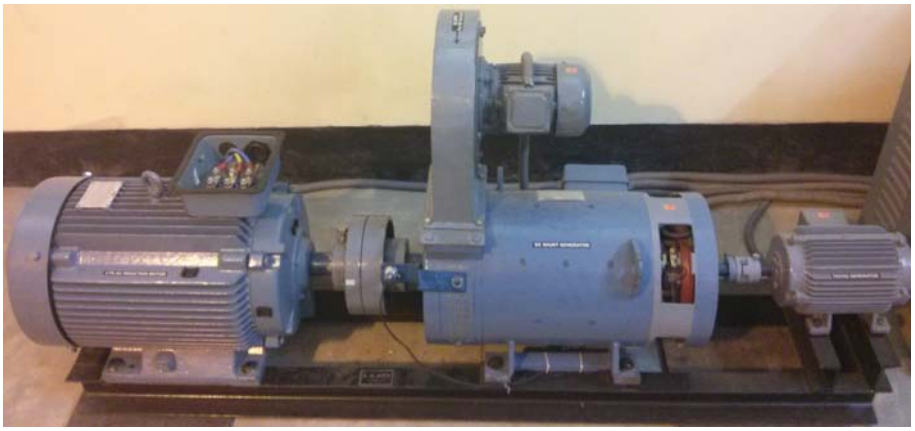

Figure 4.7: The motor-generator experimental setup

Figure 4.8: The load box

4.5.1 Design of Experiment for Eccentricity

During the experiment, it was found that one of the motors carried an inherent non-uniform air gap. Experiment with this motor along with a comparison with a healthy motor was conducted. Using a dial-gauge, the maximum deviation from the mean position was found to be 0.49 mm for the faulty case. The dial gauge was positioned on the coupler between

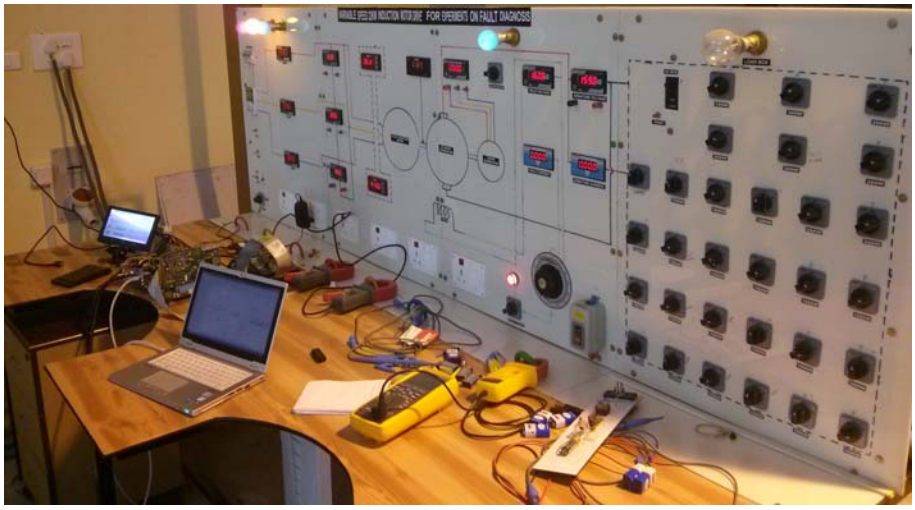

Figure 4.9: The front panel

the motor and the generator, and the readings were taken in steps of 0.5 mm along the circumference of the coupler. The first reading was taken as the reference, and all the measurement were obtained with respect to this value. The resulting variation with rotation of the motor is shown in Fig. 4.10.

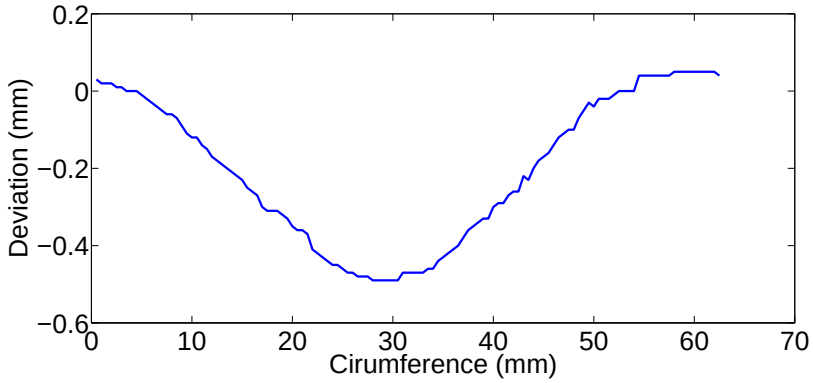

Figure 4.10: Deviation of the coupling from a given reference for the motor with inherent eccentricity

4.5.2 Design of Experiment for BRB

Experiments were performed on single rotor damaged at three different levels as given in Table 4.1 and shown in Fig. 4.11 for BRB.

Table 4.1: Design of experiment for BRB

Nomenclature	Drill Dia (mm)	Drill Depth (mm)
Healthy BRB	0.00	0.00
Partial BRB	3.09	4.00
Half BRB	3.90	16.00
Full BRB	7.54	34.00

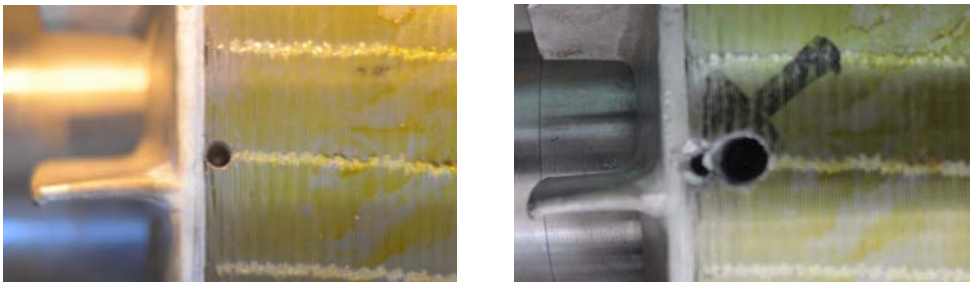

(a) Half BRB fault (b) Full BRB fault

Figure 4.11: Levels of BRB fault

4.6 Results and Discussion for Eccentricity Fault

The four-pole induction motor used for this experiment had 28 rotor bars. As a result, the most prominent fault components for eccentricity related fault can be detected using the (1.5). Fig. 4.12 - Fig. 4.21 shows the stator current spectrum around $(1+s)f_o/2$ and $(3-s)f_o/2$ for healthy and faulty cases with variable loading. It is observed that the magnitude of the fault component is present in both the faulty and the healthy motor. Although, there is a marked difference in the magnitude of the fault component for the two motors. Additionally, it is also observed that the magnitude of the fault component decreases with increased loading. This was also observed in case of the simulated motor. The fault component for the healthy case is visible under all condition of loading. As a result, the fault component is suitable to be used for estimation of speed with high accuracy. Cumulative distribution function was obtained empirically for all the faulty and healthy cases to derive a threshold for the fault hypothesis. The ECDF was determined from the peak magnitude of the lower sideband. This magnitude was normalized by the fundamental peak value before computing the ECDF for both the healthy as well as the faulty case. It can be concluded that with a threshold value of 2.282, there is less than 3% of missed detections without any false alarms. With a stricter threshold, there will be an escalation of false alarms with lower missed detections.

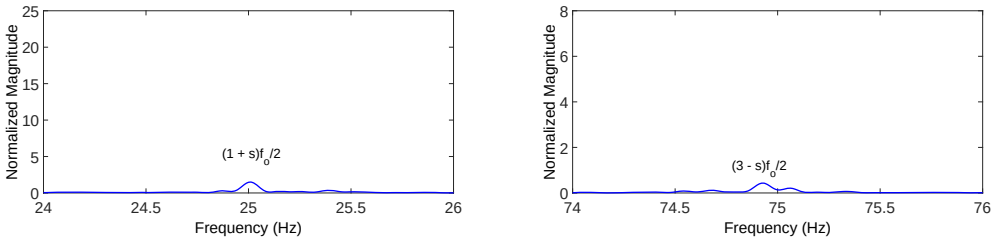

(a) Lower side band (b) Higher side band

Figure 4.12: Stator current spectrum for healthy motor with no load, and 0.13% slip

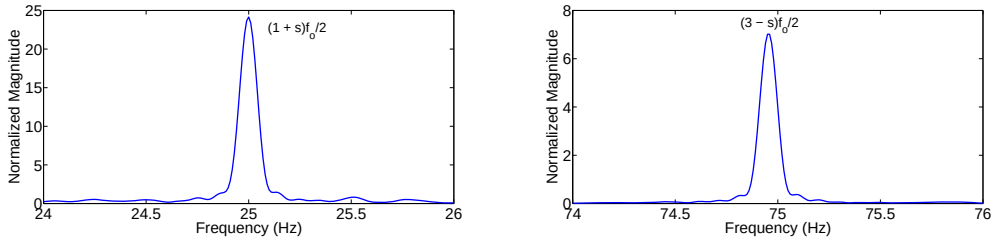

(a) Lower side band (b) Higher side band

Figure 4.13: Stator current spectrum for faulty motor with no load, and 0.13% slip

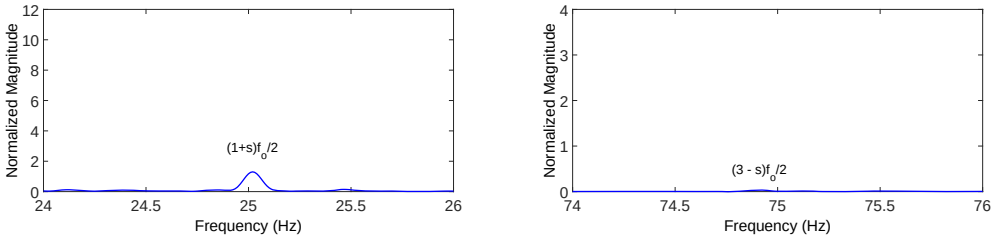

(a) Lower side band (b) Higher side band

Figure 4.14: Stator current spectrum for healthy motor with 1.9% load and 0.2% slip

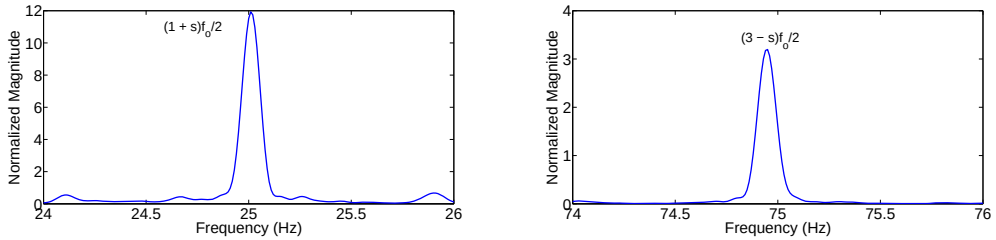

(a) Lower side band (b) Higher side band

Figure 4.15: Stator current spectrum for faulty motor with 1.9% load and 0.2% slip

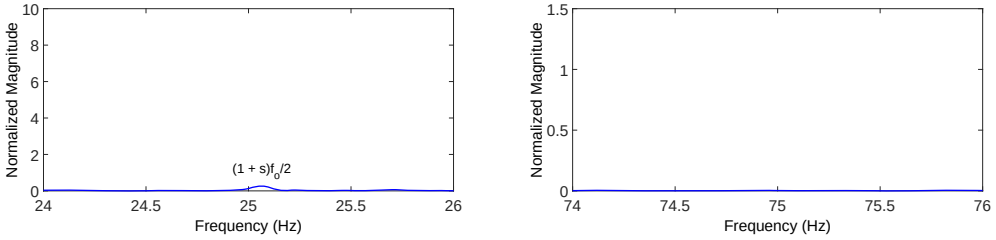

(a) Lower side band (b) Higher side band

Figure 4.16: Stator current spectrum for healthy motor with 13.5% load and 0.46% slip

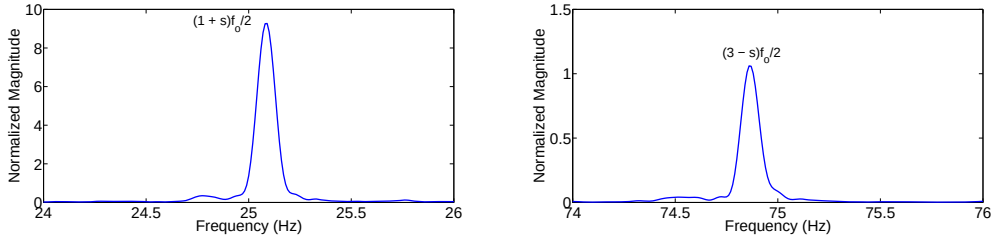

(a) Lower side band (b) Higher side band

Figure 4.17: Stator current spectrum for faulty motor with 13.5% load and 0.46% slip

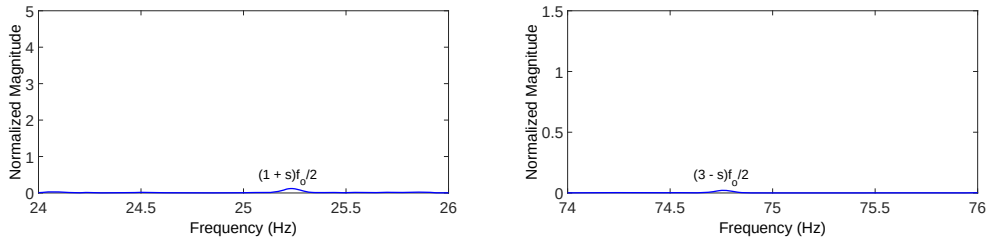

(a) Lower side band (b) Higher side band

Figure 4.18: Stator current spectrum for healthy motor with 33% load and 1% slip

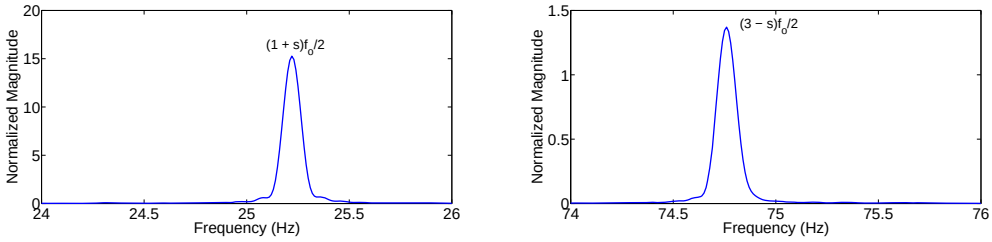

(a) Lower side band (b) Higher side band

Figure 4.19: Stator current spectrum for faulty motor with 33% load and 1% slip

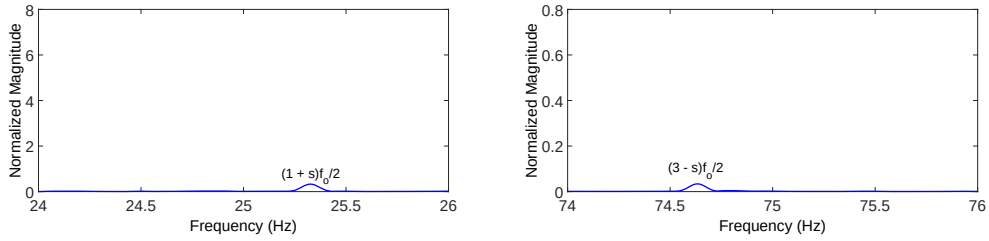

(a) Lower side band (b) Higher side band

Figure 4.20: Stator current spectrum for healthy motor with 50% load and 1.4% slip

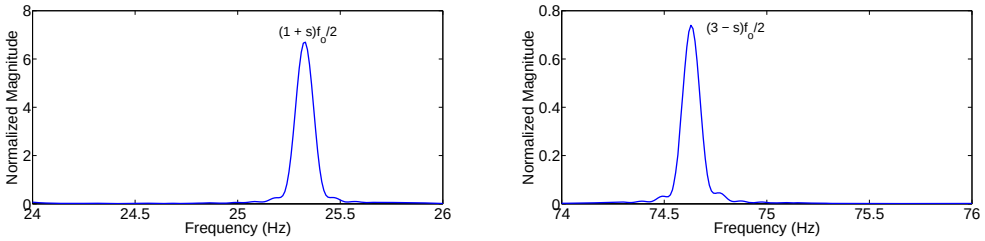

(a) Lower side band (b) Higher side band

Figure 4.21: Stator current spectrum for faulty motor with 50% load and 1.4% slip

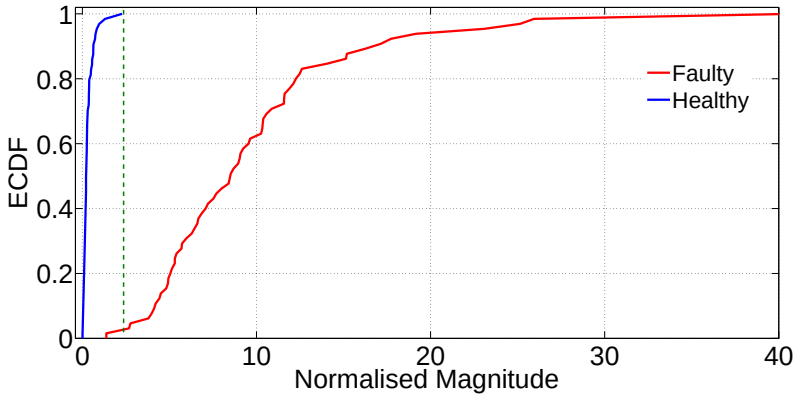

Figure 4.22: ECDF plot for mixed eccentricity faults

4.7 Results and Discussion for BRB Fault

The fault components on the stator current spectrum produced by BRB and BER are similar. Single broken bar is considered as a weak fault. In this thesis, the emphasis is laid on detection of partial broken bar fault condition under low load. In this case, the fault components are of very low magnitude and are very close to the fundamental. Hence, the signal needs to be conditioned prior to the estimation of its spectrum. As already discussed, a healthy rotor was damaged at three levels for the experiments of BRB. Different degrees of fault helps in testing the algorithms for detection of weaker faults as well as quantification of the fault. The motor was run with different supply frequencies and under various loading conditions. Fig. 4.23 to Fig. 4.26 shows the spectrum of the stator current with the supply frequency of 50 Hz. The figures are classified as (a) Healthy, (b) Partial BRB, (c) Half BRB and (d) Full BRB. It is observed the fault specific frequency component are feebly visible for the no-load condition. Although, multiple minute peaks are observed for the Partial BRB. In case of Full BRB, a significantly large, high order

component was visible. As the loading is increased in Fig. 4.24, the fault components starts appearing around the fundamental with different values of k as in (1.1). As the load is increased to 24% multiple components of BRB starts appearing for the Full BRB case. For the Partial and Half BRB cases, the components have a lower magnitude than the Full BRB case. However, on increasing the load any further, the fault component magnitude for Half and Partial BRB becomes more conspicuous than the Full BRB. For experiments with the 50 Hz supply frequency, it is observed that the magnitude of the fault component does not present a clear trend with the level of fault present. It is also observed, that, with increased loading, the low-order frequency components have significantly higher magnitude than the low-ordered components. For some cases, the Healthy motor gave rise to frequency components around the fundamental, but these components don't conform to BRB components. One such situation arose in the Partial BRB case as in Fig. 4.26(b). These components may be due to the VFD drive or due to the presence of low-frequency load torque oscillations. The distribution of the sideband band peaks around the fundamental was determined using ECDF. For this purpose, the magnitude of the sideband peaks were normalized by the fundamental peak value. ECDF curves for BRB reveals certain conditions that are highly dependant on the chosen threshold as illustrated in Table 4.2. Depending upon the application, a value of the threshold can be selected. This table was derived from the curve as shown in Fig. 4.27. A zoomed version of Fig. 4.27 is provided in Fig. 4.28 to illustrate the evaluation of the thresholds for specific missed detection and false alarms.

Fig. 4.29 to Fig. 4.31 shows the stator current spectrum for the motor supplied from a 40 Hz supply with various loads. From these figures, a trend is observed for the magnitude of the fault component for different levels of the fault. The magnitude of the fault component increases with increasing level of fault for different loads.

The Most comprehensive trend for the magnitude of the fault component was observed for the motor running with 30 Hz in Fig. 4.32 to Fig. 4.34. In this case, a clear scenario is presented. The magnitude of the fault component increases with increased level of fault for different loads.

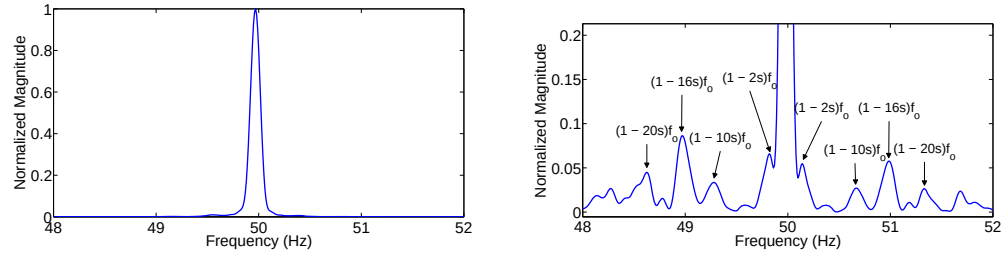

(a) Healthy BRB

(b) Partial BRB

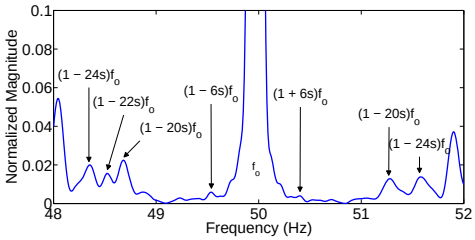

(c) Half BRB

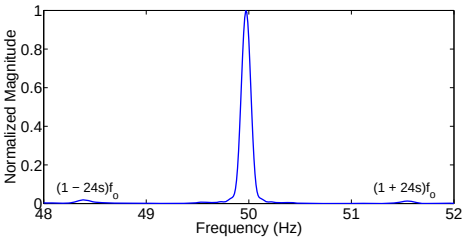

(d) Full BRB

Figure 4.23: Stator current spectrum of motor for different levels of fault (supply frequency of 50Hz, with no load and 0.13% slip)

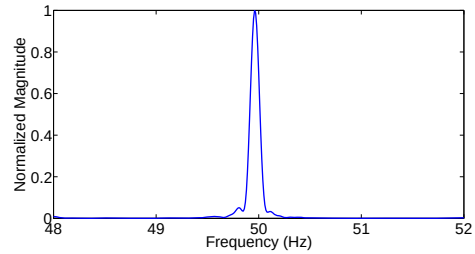

(a) Healthy BRB

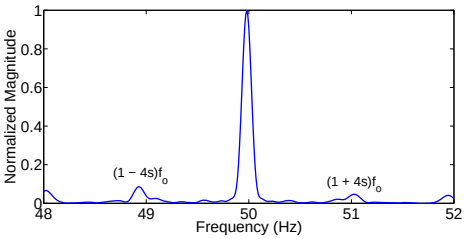

(b) Partial BRB

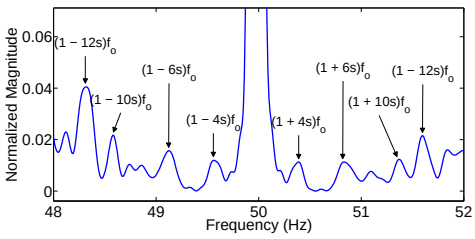

(c) Half BRB

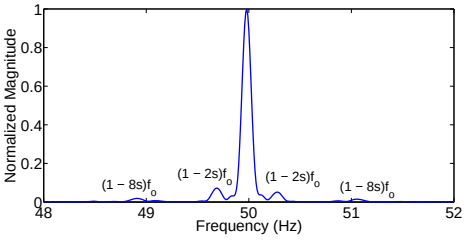

(d) Full BRB

Figure 4.24: Stator current spectrum of motor for different levels of fault (supply frequency of 50Hz, with 4.5% load and 0.26% slip)

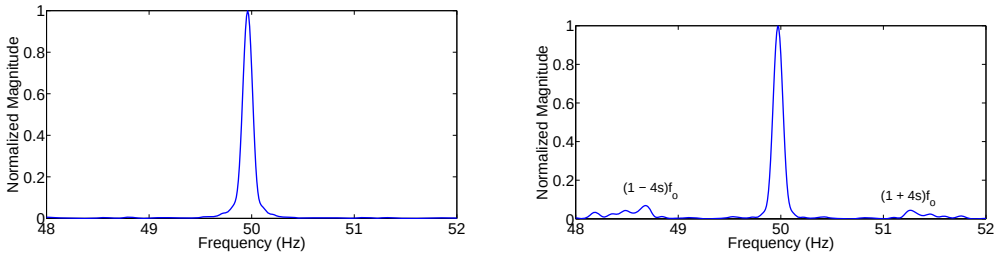

(a) Healthy BRB

(b) Partial BRB

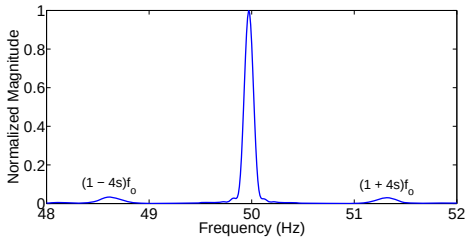

(c) Half BRB

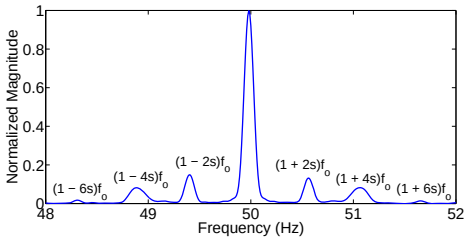

(d) Full BRB

Figure 4.25: Stator current spectrum of motor for different levels of fault (supply frequency of 50Hz, with 24% load and 0.67% slip)

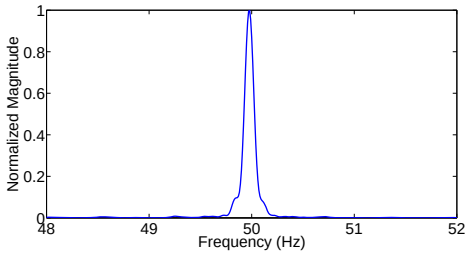

(a) Healthy BRB

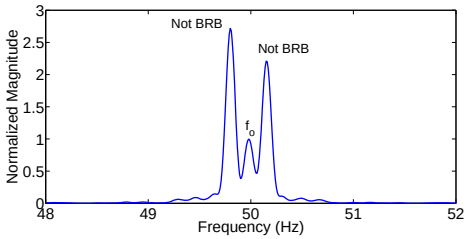

(b) Partial BRB

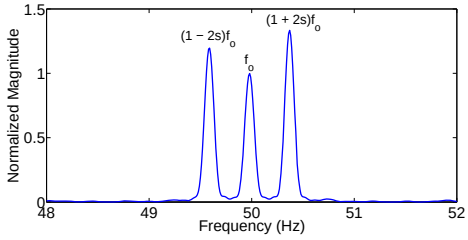

(c) Half BRB

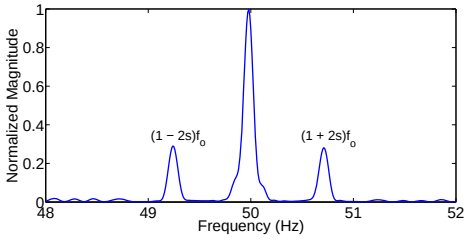

(d) Full BRB

Figure 4.26: Stator current spectrum of motor for different levels of fault (supply frequency of 50Hz, with 30% load and 0.8% slip)

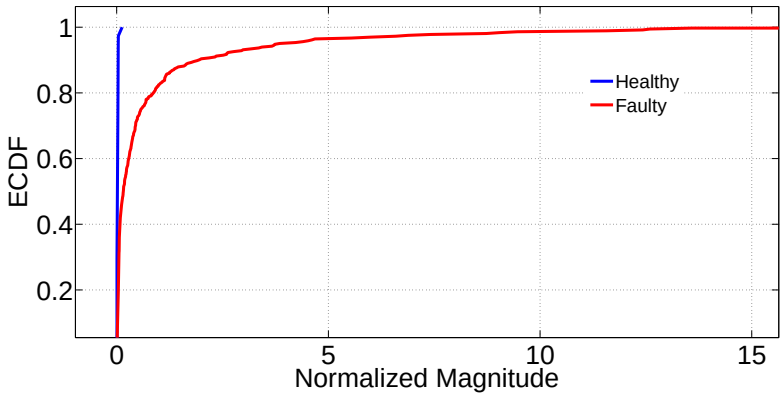

Figure 4.27: ECDF plot for BRB faults

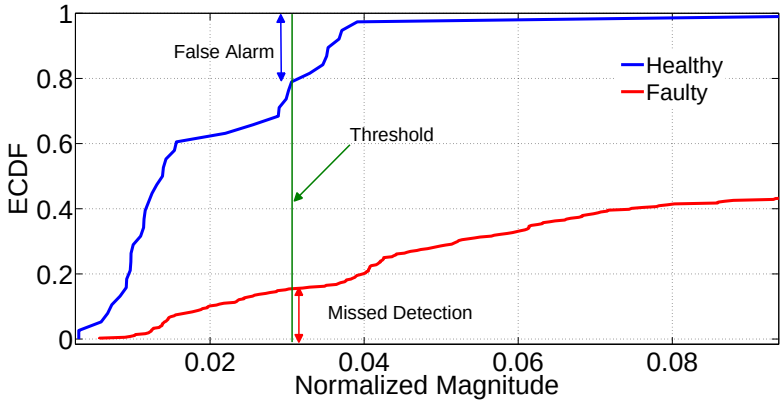

Figure 4.28: ECDF plot for BRB faults by zooming into Fig. 4.27

Table 4.2: Statistics for BRB fault

Threshold Value	Missed Detection	False Alarm
0.015	7.42%	39.47%
0.021	10.99%	36.84%
0.030	15.38%	21.05%
0.039	19.51%	2.63%

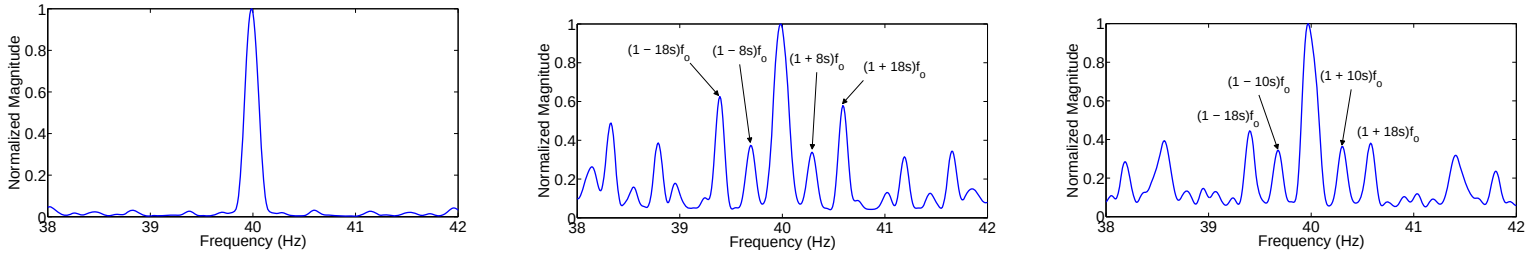

(a) Healthy (b) Half BRB fault (c) Full BRB fault

Figure 4.29: Stator current spectrum of motor for different levels of fault (supply frequency of 40Hz, with no load, and 0.083% slip)

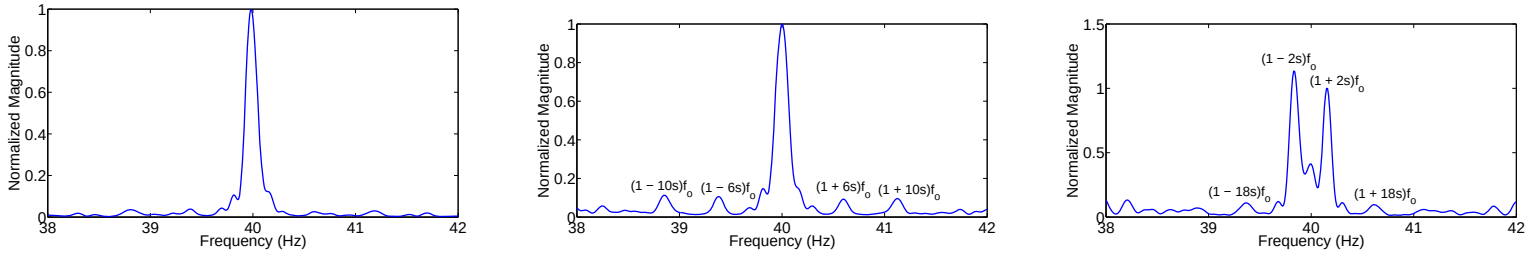

(a) Healthy (b) Half BRB fault (c) Full BRB fault

Figure 4.30: Stator current spectrum of motor for different levels of fault (supply frequency of 40Hz, with 3.7% load, and 0.25% slip)

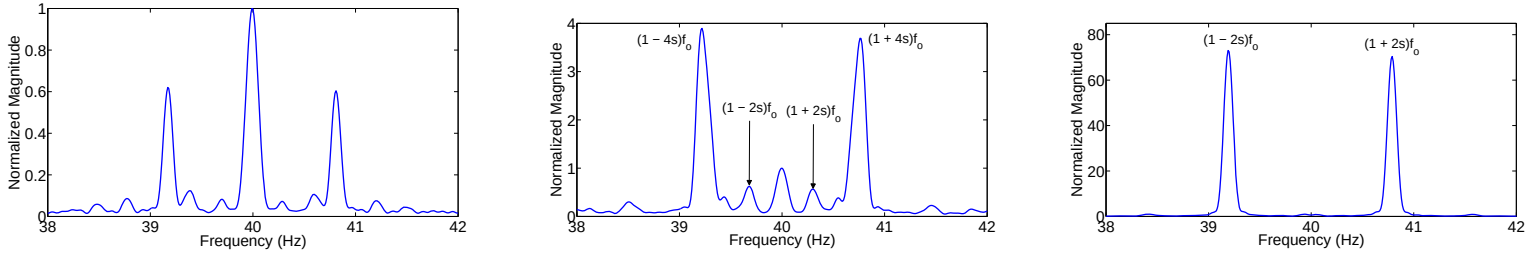

(a) Healthy (b) Half BRB fault (c) Full BRB fault

Figure 4.31: Stator current spectrum of motor for different levels of fault (supply frequency of 40Hz, with 25% load, and 1.08% slip)

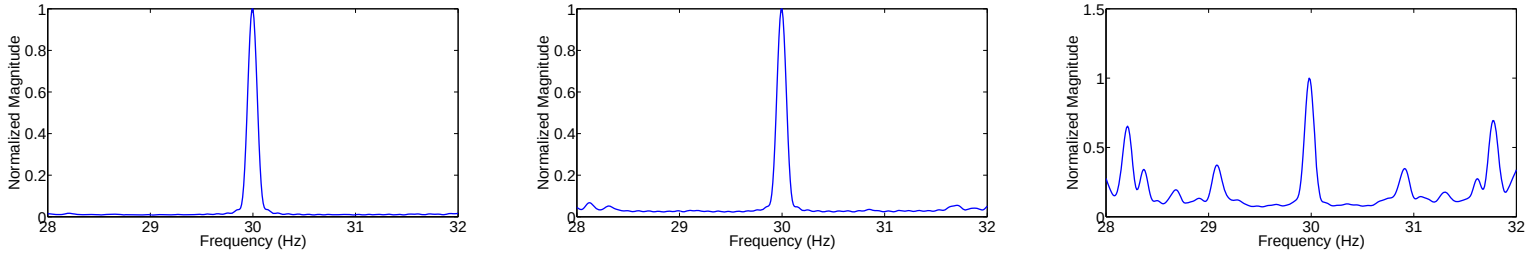

(a) Healthy (b) Half BRB fault (c) Full BRB fault

Figure 4.32: Stator current spectrum of motor for different levels of fault (supply frequency of 30Hz, with no load, and 0.083% slip)

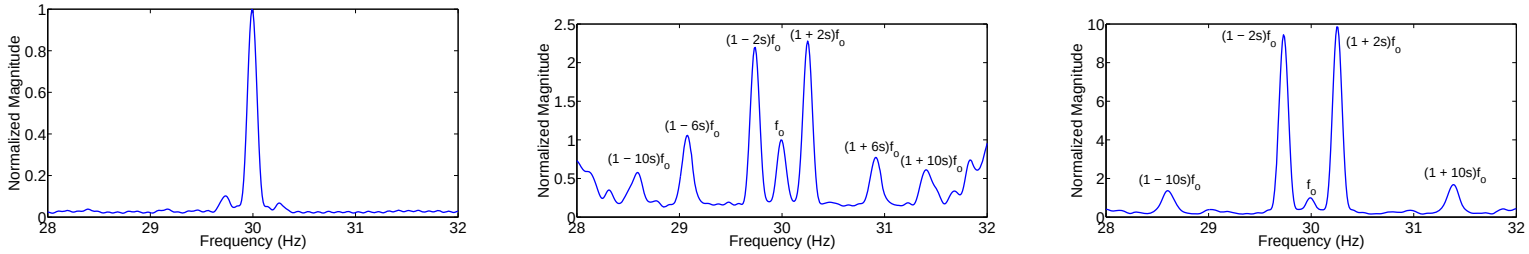

(a) Healthy (b) Half BRB fault (c) Full BRB fault

Figure 4.33: Stator current spectrum of motor for different levels of fault (supply frequency of 30Hz, with 6% load, and 0.5% slip)

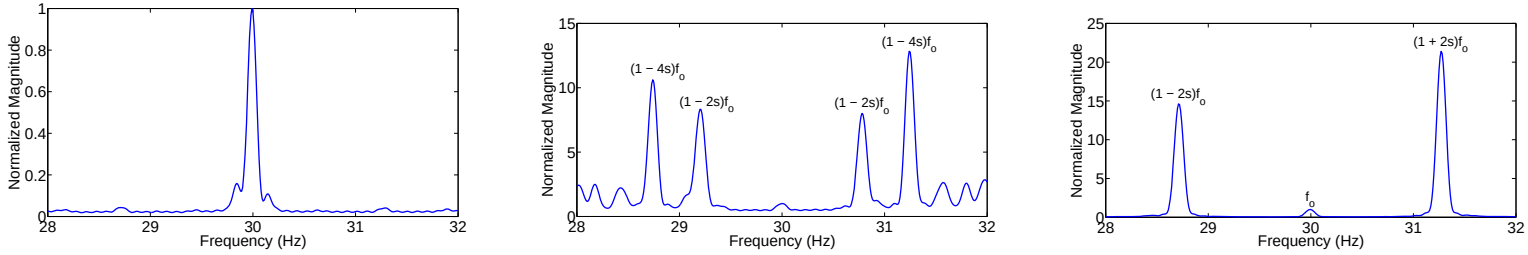

(a) Healthy (b) Half BRB fault (c) Full BRB fault

Figure 4.34: Stator current spectrum of motor for different levels of fault (supply frequency of 30Hz, with 28% load, and 2.1% slip)

4.8 Summary

This chapter presented the fault detection scheme that can be implemented on an embedded platform. Fault conditions like BRB and Eccentricity were studied in this chapter. The motor was eccentric inherently. Further investigation with proper experimental arrangements is required to quantify between weak and severe eccentricity faults. Detection of partially and completely damaged bars was accomplished with in low-loading conditions.

Fault detection was performed by spectral analysis of conditioned stator current. The proposed fault detector can detect Partial BRB fault with the motor running with 0.2% slip and 1.9% load. Using EKF-based signal conditioner has led to the detection under such conditions. Further improvement can be envisioned for detection under no-load conditions by using zooming techniques. The system uses the mixed eccentricity fault component for estimation of slip. The system is adaptive to changes in supply frequency and loads for a particular frame of data but is unsuitable for the detection of faults in transient and non-stationary conditions. Empirical CDF was adopted to determine a threshold required for assessment of faults with different levels of missed detection and false alarms. A threshold can fixed for a healthy motor with ECDF so that any fault-specific peak beyond this threshold can envisage the presence of a fault in the incipient stage. Detection of closely spaced sinusoids under low sampling rate makes this method a powerful tool for detection of eccentricity and BRB under severe physical conditions.

CHAPTER 5

Embedded System Development for Online Fault Diagnosis

This research was carried out with the goal of developing a hardware platform for implementation of an SCIM fault detector and it's testing through an RT fault simulator. For this purpose, a unified hardware platform is developed. The developed system is capable of acquiring analog input signals and process it as required. In case of the fault simulator, the input signal can be the three phase supply voltages and the load signal, whereas for the fault detector, it can be the stator current from an actual motor or signals generated by the simulator. In this chapter, a brief description of the hardware and software platform is followed by the online implementation schema for the fault detector. Discussions about the implementation of the fault simulator were provided in Chapter 3. The spectral estimator developed in Chapter 2 can be represented in the form of matrix multiplication. This form is utilized for smooth and efficient implementation of the spectral estimator. A brief description of the implementation of the proposed spectral estimator is also presented. This chapter also discusses the evolution of the fault detector from it's primitive phase to the current state.

5.1 The Embedded Platform

DOS based RT kernel popularly known as SIMULINK Real Time (SLRT) Target (formerly known as xPC target) developed by Mathworks is used for the online implementation. The RT kernel along with an x86-based computer system provides an environment for emulation

of the complex fault detection codes. SLRT is a Host-Target based system, where the codes are initially formulated in the host computer using SIMULINK and MATLAB. Once the codes are compiled, an executable file is generated. This file is transferred to the target computer for RT execution. A diagram to illustrate the functional flow for creating the executable is shown in Fig. 5.1. The host-target interface is established through Ethernet. A solid state hard disk is used on the target machine for logging of data, which can be accessed from the host computer. The target computer can also run in standalone mode with no intervention from the host computer. Initially in the host computer, a SIMULINK model is created for the required application with all the system and IO requirements. A photograph of the developed system is shown in Fig. 5.2. The main technical specification of the developed system is given in Table 5.1.

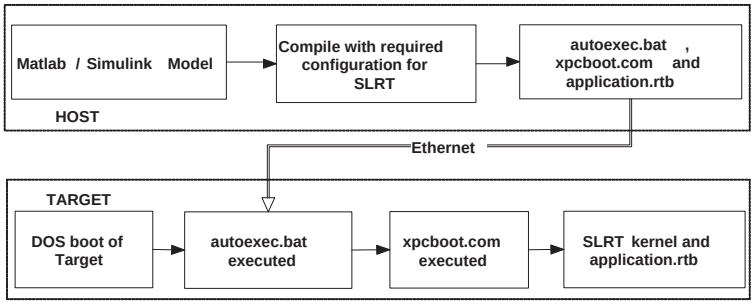

Figure 5.1: Flow diagram illustrating the steps required for execution of a simulink model in RT environment of xPC kernel

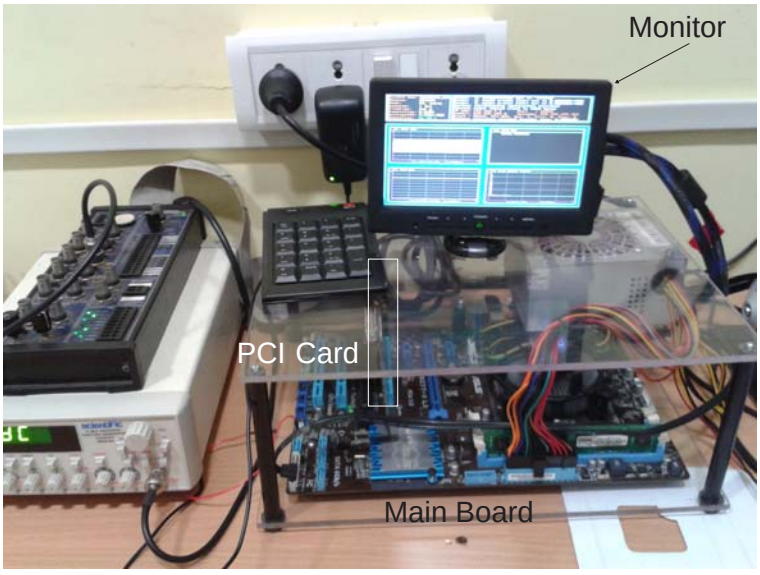

Figure 5.2: Photograph of the developed system

Table 5.1: Technical specification of the target hardware

Sl. No.	Subsystem	Description
1	Main Board	Asus(Z87)
2	PCI slots	3xPCI,2xPCIe(x16)
3	Ethernet ports	1xGigabit LAN Controller
4	USB ports	6 x USB 3.0/2.0
5	Processor	Intel Core i7
6	Speed	3.4 GHz
7	RAM	8GB DDR3 (1600 MHz)
8	Hard Disk	120 GB Solid State [1]
9	BIOS	UEFI AMI BIOS
10	ROM	64 Mb Flash
11	Media	HDMI
12	IO Interface	NI PCI 6024E
13	Analog input	16 SE, 8 DE
14	Sampling freq.	200KHz (max)
15	Resolution	12 bit
16	Analog output	2 Channels

5.2 Implementation of the Proposed Spectral Estimator

Chapter 2 focussed on deriving the magnitude of a single frequency in the spectrum using the proposed spectral estimator. It was found, that the spectral estimator can be formulated in a simple vector-matrix format for easy implementation. This formulation is suitable for finding the spectral magnitudes in a single specific band or in multiple bands. The formulation involves a matrix multiplication followed by extraction of diagonal elements as given below

$$\hat{\mathbf{h}} = diag\left(\mathbf{W}^H \hat{\mathbf{R}}_x \mathbf{W}\right) \tag{5.1}$$

where, $\mathbf{W} \in [\mathbf{w}(\omega_l) : \omega_{steps} : \mathbf{w}(\omega_u)]$ is known as the search manifold matrix. The normalized frequency band where the search is made is represented by $[\omega_l, \omega_u]$. $\mathbf{w}(\omega_i) = \begin{bmatrix} 1 & e^{j\omega_i} & \cdots & e^{j\omega_i(L-1)} \end{bmatrix}^H$, and L is the size of the autocorrelation matrix $\hat{\mathbf{R}}_x$ given by (2.12). Now the diagonal elements of the matrix $(\mathbf{W}^H \hat{\mathbf{R}}_x \mathbf{W})$, when extracted contains the spectral peaks in the region where the search is made. Fig. 5.3 shows the contour map of the matrix and Fig. 2.4 showed the diagonal elements of this matrix representing the spectral peaks of the given signal.

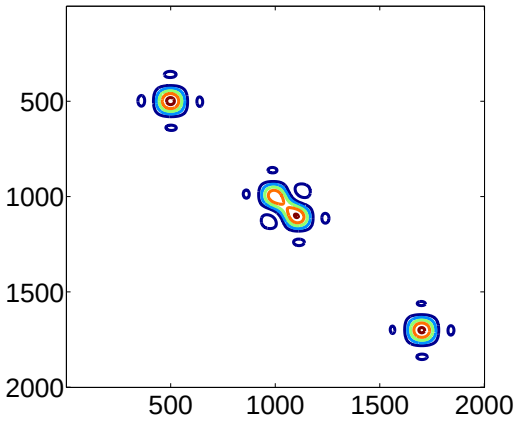

Figure 5.3: Contour map of matrix the $\mathbf{W}^H \hat{\mathbf{R}}_x \mathbf{W}$

5.2.1 Mathematical Insight into the Implementation Procedure

The spectral peaks of (5.1) can be decomposed by using (2.12) into

$$\hat{\mathbf{h}} = \frac{1}{L} diag \left\{ (\mathbf{X}_\beta \mathbf{W})^H (\mathbf{X}_\beta \mathbf{W}) \right\} \tag{5.2}$$

Taking into consideration a single element of the product of (5.2) and evaluating $(\mathbf{X}_\beta \mathbf{W})$ gives

$$\mathbf{X}_\beta \mathbf{W} = \begin{bmatrix} \sum_{i=0}^{L-1} x(i) e^{-j\omega_l \cdot i} & \cdots & \sum_{i=0}^{L-1} x(i) e^{-j\omega_u \cdot i} \\ \vdots & \ddots & \vdots \\ \sum_{i=0}^{L-1} x(i+L-1) e^{-j\omega_l \cdot i} & \cdots & \sum_{i=0}^{L-1} x(i+L-1) e^{-j\omega_u \cdot i} \end{bmatrix} \tag{5.3}$$

Now, with the assumption that

$$X_p(\omega_q) = \sum_{v=0}^{L-1} x(v+p) e^{-j\omega_q \cdot v} \tag{5.4}$$

And using (5.4) in (5.3) gives

$$\mathbf{X}_\beta \mathbf{W} = \begin{bmatrix} X_0(\omega_l) & \cdots & X_0(\omega_u) \\ \vdots & \ddots & \vdots \\ X_{L-1}(\omega_l) & \cdots & X_{L-1}(\omega_u) \end{bmatrix} \tag{5.5}$$

Putting the value of (5.5) in (5.2), we get

$$\hat{\mathbf{h}} = \frac{1}{L}\left[\sum_{i=0}^{L-1} |X_i(\omega_l)|^2 \quad \cdots \quad \sum_{i=0}^{L-1} |X_i(\omega_u)|^2 \right]^T \tag{5.6}$$

Further simplification is achieved by taking the square of the absolute value on both sides in (5.4) and putting this value in (5.6), resulting in

$$\hat{\mathbf{h}} = \frac{1}{L}\left[\sum_{i=0}^{L-1} \left| \sum_{v=0}^{L-1} x(v+i)e^{-j\omega_l \cdot v} \right|^2 \quad \cdots \quad \sum_{i=0}^{L-1} \left| \sum_{v=0}^{L-1} x(v+i)e^{-j\omega_u \cdot v} \right|^2 \right] \tag{5.7}$$

Magnitude of a particular sinusoidal component at ω_k is given by

$$\hat{h}(\omega_k) = \frac{1}{L} \sum_{i=0}^{L-1} \left| \sum_{v=0}^{L-1} x(v+i)e^{-j\omega_k \cdot v} \right|^2 \tag{5.8}$$

This component is similar to the relation obtained in (2.21). A block diagram to illustrate the implementation of the spectral estimator is shown in Fig. 5.4. The spectral estimator is crucial for the detecting multiple faults and slip related frequency components. For developing a complete system, the spectral estimator needs to be efficient and accurate. It can be made efficient by searching in specific pre-defined bands instead of the full band. These frequency bands are fixed from the slip and fundamental frequency information. Modification of the spectral estimator to evaluate the spectral magnitude in multiple bands is given below:

5.3 Modification of the Spectral Estimator for Multiple Search Bands

For detecting multiple faults, the major modifications are associated with the spectral estimator. As is evident from Table 1.1, different faults in induction motor occupy different bands on the stator current spectrum. It is possible to evaluate the peak and their magnitude in the concerned band of interest instead of searching the whole band. This amounts to performing the spectral estimation in small multiple bands. It is considered that the frequency components of interest lie sporadically over the entire space defined by ω. In this situation, it is not viable to search in the full frequency space. Let's assume that there are k Central Frequencies (CFs) and are known apriori given by $[\omega_1, \omega_2, ..., \omega_k]$. These CFs can be obtained from Table 1.1. Search bands are constructed around these CFs. A spectral search band corresponding to the ith CF is characterized by its lower ω_i^l and upper ω_i^u band limit. Multiple search manifold matrix is constructed with the bands thus formed. A particular step size is also selected as per the resolution requirement. The search manifold

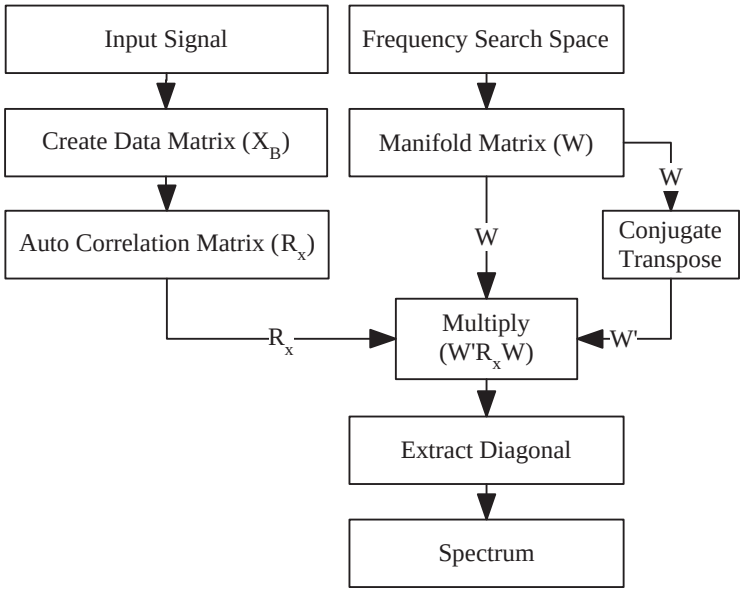

Figure 5.4: Block diagram of the spectral estimator for fault detection

matrix for the overall search space is given by

$$\mathbf{W} = \begin{bmatrix} \mathbf{\Omega}_1 & \mathbf{\Omega}_2 & \cdots & \mathbf{\Omega}_k \end{bmatrix} \tag{5.9}$$

where $\mathbf{\Omega}_i$ represents the search manifold matrix for ith CF and is given by

$$\mathbf{\Omega}_i = \begin{bmatrix} 1 & 1 & \cdots & 1 \\ e^{j\omega_i^l} & e^{j\left(\omega_i^l+\Delta\omega_i\right)} & \cdots & e^{j\omega_i^u} \\ \vdots & \vdots & \vdots & \vdots \\ e^{j\omega_i^l(L-1)} & e^{j\left(\omega_i^l+\Delta\omega_i\right)(L-1)} & \cdots & e^{j\omega_i^u(L-1)} \end{bmatrix} \tag{5.10}$$

$\Delta\omega_i$ represents the steps in which ω_i^l is increased to ω_i^u. The value of $\Delta\omega_i$ is constant for a particular CF but may vary for different CFs.

5.4 Implementation of the Online Fault Detector

Online implementation of the fault detector was carried out using different methodologies. A brief overview of the various methods is provided in Fig. 5.6. The SIMULINK model is developed in accordance with the system described in Fig. 4.1 for detection of faults. A detailed diagram to illustrate the full working of the implemented system can be seen in

Fig. 5.5

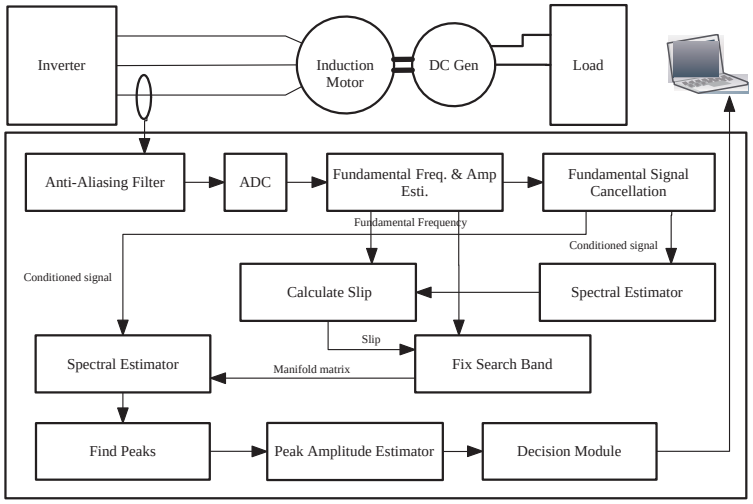

Figure 5.5: Fault detection scheme

It consists of two phase. The first stage is used for initialization and the second for execution. In the first phase, various physical motor parameters and information about different variables are defined. Dynamic memory allocation problems are avoided by fixing the dimension of vectors and matrices that are to be used in the execution phase. This part of the code is run in the non-RT environment, and the variables defined here are constant throughout the code. These constants can be classified into different groups like the parameters required for fundamental frequency estimation, slip estimation, spectral estimation, sampling rates, execution time-steps, etc. The second part is used for estimating the amplitude of the fault specific frequency components that are to be detected. For this purpose, the stator current signal is acquired with the analog input card of NI PCI 6024E. This data is then fed to different subsystems for estimation of the slip, and the fundamental frequency. The block for estimating the fundamental frequency is also used for input signal conditioning. The time of execution and the data acquisition sample time is same till this point, and the execution is performed in RT. After this point, buffers are used for storing a frame of data, and these frames are transferred to the spectral estimator block which executes with a slower execution time.

The design of the existing SCIM fault detection system has evolved in the duration of this research. In this thesis, two of the most significant developments are discussed before presenting the final version. A separate section is dedicated to the discussion about the major steps that are involved in the development of the system for detection of multiple faults efficiently. A brief description of each method is provided below:

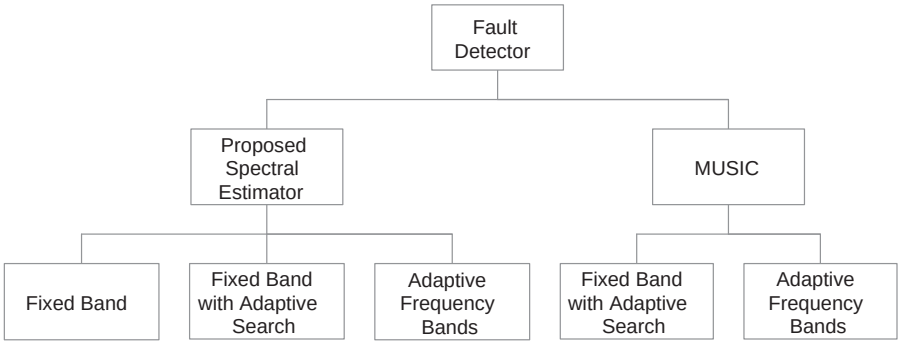

Figure 5.6: Classification and evolution of different implementation strategies for both the spectral estimators

5.4.1 Single Fixed Frequency Band for Detection of Single Fault

In this case, the spectral estimator estimates the magnitude of the frequency components in a fixed band. This band is fixed in the initialization stage and so is the manifold matrix **W**. A search is made after spectral estimation to find the peak in the fixed band for a fault component. The search space is also non-adaptive in nature and is fixed. This method is suitable for detection of a single fault in case of motors where the supply frequency is fixed, and the variation of the load is also small. The maximum allowed size of the model for SLRT is limited to 4MB for standalone applications. As a result, this implementation scheme is not suitable, as large matrices are created during the initialization stage. This particular method though easy to implement but requires the vital parameters like the search space to be prefixed.

5.4.2 Single Fixed Frequency Band for Detection of Multiple Faults

In this case also, the frequency band for the spectral estimator is fixed. As the method is suited for multiple fault detection, therefore, the spectral estimation is performed over a large band of frequency. This band is fixed in the initialization stage. The only change is in the search space. The search space is made adaptive to changes in fundamental supply frequency and slip. Mean values of this slip and fundamental frequency are used to fix the search band for a particular frame of conditioned stator current. Meanwhile, the spectral estimation of the stator current is accomplished over the full band, and fault component peaks are searched in the distinct search bands. This method is suitable for detection of multiple faults simultaneously under variable loading and change in fundamental supply frequency. This method requires large memory space for storing the **W** matrix and hence is not suitable for the standalone application.

5.4.3 Multiple Adaptive Frequency Bands for Detection of Multiple Faults

In this case, the spectral estimation is accomplished over multiple frequency bands. These frequency bands are characterized by their central frequency and bandwidth. The central frequencies are fixed from various literature surveys as given in Table 1.1. The bandwidth is set during the initialization phase, whereas the central frequencies are adaptive to the changes in rotor speed and supply frequency. The number of CFs and the bandwidth is fixed at the initialization stage. As a result, dynamic memory allocation problems are circumvented. The content of each of the bands are dynamic and are assigned during the runtime. With this implementation, the time required for the spectral estimation is reduced drastically, although the contents of **W** needs to be assigned for every step unlike the methods discussed above. This design is suited for detection of multiple faults very efficiently. The memory required for this method is reduced as **W** is small. As a result, standalone application is also suitable with this design.

5.4.3.1 Implementation of 'Multiple Adaptive Frequency Band' fault detection Schema

Online implementation scheme for detection of multiple faults was implemented on a hardware platform for online execution as described at the beginning of the chapter. The architecture of the fault detection system comprises two execution subsystems. The first subsystem is executed on the host computer and is executed in non-real-time, while, the second subsystem is used for execution of the fault diagnostic algorithm in a real-time frame processing based environment, where the data is acquired at a much faster rate than the execution rate. This is accomplished by using 'Function call generator' sub-block which process an array of buffered data at the specified execution rate. No data is missed, as the overall system works with single sampling rate. The first subsystem is used for initialization of various model parameters like the data acquisition sample time, execution time-step, and necessary motor parameters like pole-pairs, no. of bars, rated voltage, rated current and rated speed, etc. It is in this part that the number of faults to be detected, the total number of bands to be searched, and the width of each band are defined. The frequency search space thus created is dimensionally fixed and, as a result, doesn't require dynamic memory allocation. The workflow of the second subsystem can be enumerated in the following steps.

i. The stator current is acquired with the predefined sampling rate of 200 Samples/sec.

ii. The acquired data is sent to the next block for supply frequency estimation and signal conditioning using EKF.

iii. A block estimates the slip according to (4.17).

iv. A buffer is used for storing the acquired samples. The fundamental frequency is computed with the acquisition rate. As a result, the stator current, slip, and fundamental

frequency are stored in a buffer, and this frames of data are transferred to the next section, where the processing of these data takes place.

v. For a particular set of stator current, the mean values of fundamental frequency, and the slip are taken for creation of the search space required for spectral estimation.

vi. Autocorrelation matrix is then created from the stator current data.

vii. Multiple search bands are created from fundamental frequency and slip for different faults.

viii. Spectral estimation is performed on the conditioned stator current over the constructed frequency search space for all the faults.

ix. Peaks in the spectrum are detected. Magnitude of the normalized peaks are determined and are sent to a decision block. The decision block compares the peak amplitudes with a predefined thresholds for establishing the presence of fault and can also assess of fault severity depending on the amplitude.

The SIMULINK implementation of the 'Multiple Adaptive Frequency Band' fault detection system is shown in Fig. 5.7. A screenshot from the fault detection system console running the SIMULINK model in RT with SLRT is shown in Fig. 5.8. Technical specification of the fault detection algorithm is provided in Table 5.2.

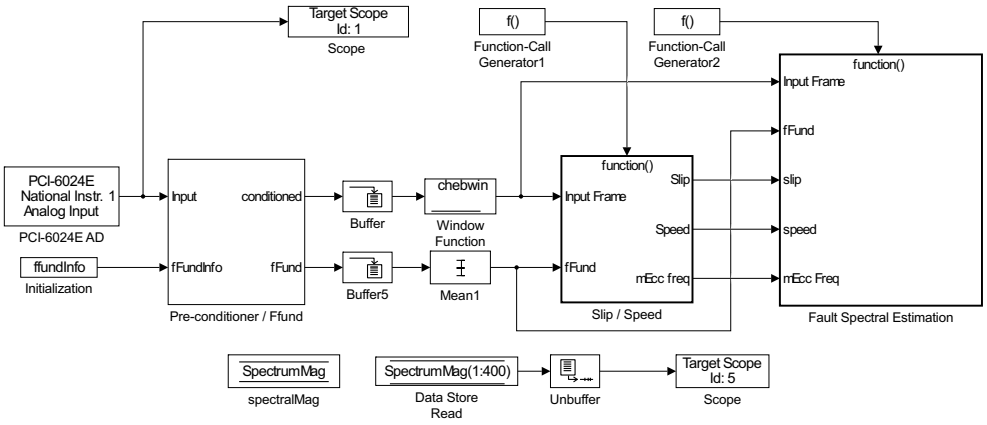

Figure 5.7: Implementation of the fault detector in SIMULINK for SLRT

5.5 Summary

This chapter presents the schemes that were utilized for the online and RT implementation of the fault detection system. SLRT based hardware platform was developed for this purpose.

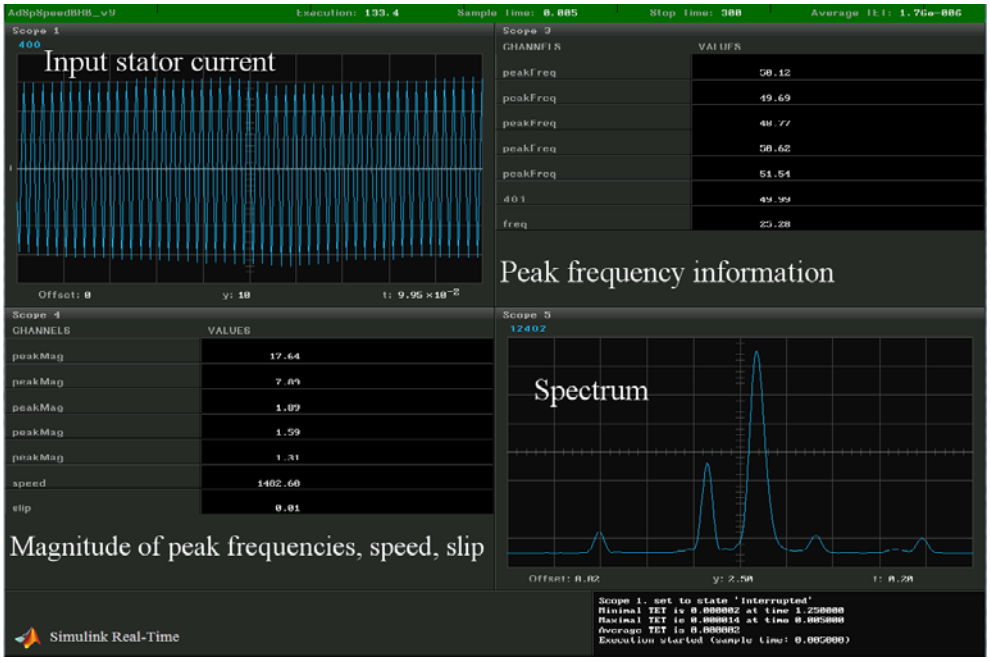

Figure 5.8: Screen shot of the fault detector console

Table 5.2: Technical specification of the Fault Detection Algorithm

Sl. No.	Subsystem	Description
1	Sampling rate	200 samples/s
2	No. of samples acquired	4000
3	Data acquisition time	20s
4	Processing time/frame	20s
5	No. of faults to be identified	2
6	No. of frequency bands observed	3
7	Additional estimated quantities	Slip, fundamental frequency, peak amplitude

The schematic diagram about the implementation of the spectral estimator is also presented. It is also discussed, how the spectral estimator is modified for estimation of multiple spectral bands. This has led to faster execution with the minimal use of memory.

CHAPTER 6

Conclusion and Future Directions

6.1 Summary of the Studies

This thesis presents the methods and technologies required for an online condition monitoring of induction motors. A special application of this scheme can be the railway locomotive engine.

Induction motors' wide utilization in various industries has led to wide-scale research to detect faults to avoid unscheduled termination of productivity. Through this research, an unsupervised condition monitoring system for early detection of incipient faults in induction motors is developed. The faults under consideration were confined to the rotor faults like BRB, BER, and eccentricity. The method of fault detection is based on spectral analysis of the stator current. The spectral estimation is performed by an elegant Rayleigh quotient-based method. This method is having lower computational complexity than the popular method of MUSIC and can also estimate the amplitude of constituent sinusoids with high accuracy. This information is vital for quantifying the degree of fault present. The Probability of resolution was used to determine statistically the resolution variation with different values of autocorrelation matrix size, sampling frequency, and SNR level. The resolution capacity is found to be lower than the Fourier resolution limit of (Fs/L). Error in the estimation of the frequency was found and compared to MUSIC and DFT. It was found that the proposed method has higher accuracy than DFT and is at par to that of MUSIC.

For testing the fault diagnosis system, an RT SCIM fault simulator is also developed. Analysis of the fault simulator was carried out with the proposed spectral estimator. The spectral signatures of the fault simulator were in agreement with the available literature

and replicates the actual lab setup, with the difference in magnitudes due to the difference in their sizes. The motor parameters used for the simulation is from the motor that is available in the literature. Validation of the simulator is envisaged for the experimental motor, which requires experiments for the parameter estimation of the motor.

The basis of the fault detection is the spectral estimation of the conditioned stator current. An EKF-based signal pre-conditioning unit is used in conjunction with the spectral estimator to detect sinusoids that are close to the fundamental and have negligible magnitude compared to the fundamental. It was found that the component of the mixed eccentricity was present inherently in all the motors. Although, the magnitude of this component varies drastically in the presence of eccentricity fault. It was found, that the magnitude decreased with increased loading of the motor. Rotational speed is estimated from the slip obtained from this mixed eccentricity component. The slip along with the value of the fundamental frequency is used for creating multiple search bands for detecting multiple faults. Most of research concerned with detecting BRB faults are confined to the detection of multiple bar failures. In this thesis, a single bar with various levels of damage were tested. The spectral estimator was found to be reliable in quantifying the degree of damage. The normalized peak magnitude of sideband frequency components w.r.t the fundamental is considered as the discriminating feature for fault detection and quantification. The distribution of the normalized magnitude is determined using ECDF. In case of BRB, the distribution of healthy and faulty cases overlap with each other. As a result, there is a chance of false and missed detection in case of weak faults running under low loads. The thresholds are selected, considering both the missed detection and false alarm rates. With increased loading and degree of the fault, the normalized magnitude can clearly distinguish between a healthy and faulty motor. In case of the eccentricity fault, distribution of the healthy and faulty cases do not overlap. As a result, the probability of missed detection is negligible, with very low false alarm. An embedded hardware platform is developed for online fault diagnosis and RT fault simulation. The fault detection algorithm evolved from the primitive form to its current form in the due course of this research. Presently, the fault detector uses 'Multiple Adaptive Frequency Band' for detection of multiple faults. This method is fast and takes minimal space in terms of memory.

The novel and original methods developed in the present study will find useful applications not only in areas in fault detection but also other areas of science and engineering in the near future. For example, the Rayleigh quotient-based spectral estimator can be modified to be used in the direction of arrival applications with the added advantage of exact peak magnitude which is not available in subspace-based methods.

6.2 Contribution of the Thesis

The contribution of the thesis can be enumerated as:

i. A high-resolution spectral estimation technique based on Rayleigh quotient is proposed for semi RT and frame processing based implementation with computational complexity lower than the conventional method of MUSIC. This spectral estimator is capable of estimating the accurate amplitude of sinusoids, and it doesn't require additional information about input signal parameters like the number of sinusoids. The practical limit of resolution with different parameters for the spectral estimator is evaluated by the probability of resolution. Relative errors were statistically determined and compared with DFT and MUSIC.

ii. A system is developed for fault detection. This system consists of proposed spectral estimator, a fundamental frequency tracker, a signal conditioner, and a speed estimator. Use of EKF-based signal conditioner has improved the detectability of BRB fault components. This method is also suitable for online implementation as it is adaptive to changes in speed and supply frequency. The amplitude of fault specific components is shown to be dependent on the degree of the fault. Empirical Cumulative Distribution Function (ECDF) was utilized to find the threshold for the two faults for particular missed detection and false alarm rate.

iii. An RT SCIM simulator for simulation of BRB, BER and different type of eccentricity faults has been developed.

iv. An experimental test setup comprising of a 22KW SCIM with minimal to the overloading arrangement has been designed for emulation of different faults. BRB has been tested for different levels of damage to a single rotor. Additionally, an RT hardware platform for RT fault simulation and online fault detection has been designed.

6.3 Future Scope

The investigation carried out in the present work leaves enough scope for extension of the approaches presented in this thesis. The future lines of investigation related to the thesis are listed below:

i. The spectral estimator can be improved for better resolution and accuracy with sparse techniques. Improvement of the present form is possible using zooming.

ii. The fault simulator can be made more precise with the inclusion of effects like skewing of rotor bars and slotting.

iii. Currently, the fault detector needs 20 seconds of statistically stationary data at 200 samples/s. The algorithm needs to be improved with a lower acquisition time.

iv. For the online system, concurrent and multicore implementation with SLRT can be utilized for faster execution

v. The present study on eccentricity fault was based on the inherent eccentricity observed in one of the motors. In future, test-setups can be designed for systematic emulation of eccentricity and bearing related faults.

vi. With the current state of the fault detection scheme, further improvements can be envisaged with portable solutions with ARM, FPGA, and DSP-based boards.

References

[1] R. Isermann, *Fault-Diagnosis Systems*. Springer, 2006.

[2] S. Nandi, H. A. Toliyat, and X. Li, "Condition Monitoring and Fault Diagnosis of Electrical Motors A Review," *IEEE Trans. Energy Convers.*, vol. 20, no. 4, pp. 719–729, Dec. 2005.

[3] H. Henao, C. Bruzzese, E. Strangas, R. Pusca, J. Estima, M. Riera-guasp, and S. Hedayati-kia, "Trends in Fault Diagnosis for Electrical Machines: A Review of Diagnostic Techniques," *Industrial Electronics Magazine, IEEE*, vol. 8, no. June, pp. 31–42, 2014.

[4] S. H. Kia, H. Henao, and G.-A. Capolino, "Zoom-music frequency estimation method for three-phase induction machine fault detection," in *Industrial Electronics Society, 2005. IECON 2005. 31st Annual Conference of IEEE*. IEEE, 2005, pp. 6–pp.

[5] G. Didier, E. Ternisien, O. Caspary, and H. Razik, "Fault detection of broken rotor bars in induction motor using a global fault index," *Industry Applications, IEEE Transactions on*, vol. 42, no. 1, pp. 79–88, 2006.

[6] B. Xu, L. Sun, and H. Ren, "A New Criterion for the Quantification of Broken Rotor Bars in Induction Motors," *IEEE Trans. Energy Convers.*, vol. 25, no. 1, pp. 100–106, Mar. 2010.

[7] T.-j. Kang, S. Member, J. Kim, S. Member, S. B. Lee, S. Member, C. Yung, and S. Member, "Experimental Evaluation of Low-Voltage Offline Testing for Induction Motor Rotor Fault Diagnostics," *IEEE Trans. Ind. Appl.*, vol. 51, no. 2, pp. 1375–1384, 2015.

[8] A. Sapena-bano, M. Pineda-sanchez, R. Puche-panadero, J. Perez-cruz, J. Roger-folch, M. Riera-guasp, and J. Martinez-roman, "Harmonic Order Tracking Analysis : A Novel Method for Fault Diagnosis in Induction Machines," *IEEE Trans. Energy Convers.*, no. 1, pp. 1–9, 2015.

[9] J.-h. Jung, J.-j. Lee, and B.-h. Kwon, "Online Diagnosis of Induction Motors Using MCSA," *IEEE Trans. Ind. Electron.*, vol. 53, no. 6, pp. 1842–1852, 2006.

[10] C. Bruzzese, O. Honorati, E. Santini, and D. Sciunnache, "New Rotor Fault Indicators for Squirrel Cage Induction Motors," in *Industry Applications Conference, 2006. 41st IAS Annual Meeting. Conference Record of the 2006 IEEE*, vol. 00, no. c, 2006, pp. 1541–1548.

[11] C. Bruzzese, "Analysis and Application of Particular Current Signatures (Symptoms) for Cage Monitoring in Nonsinusoidally Fed Motors With High Rejection to Drive Load , Inertia , and Frequency Variations," *IEEE Trans. Ind. Electron.*, vol. 55, no. 12, pp. 4137–4155, 2008.

[12] C. Yang, T.-j. Kang, S. B. Lee, J.-y. Yoo, A. Bellini, L. Zarri, and F. Filippetti, "Screening of False Induction Motor Fault Alarms Produced by Axial Air Ducts based on the Space Harmonic-Induced Current Components," *IEEE Trans. Ind. Electron.*, vol. 0046, no. c, pp. 1–1, 2014.

[13] A. Khezzar, M. Y. Kaikaa, M. E. K. Oumaamar, M. Boucherma, and H. Razik, "On the Use of Slot Harmonics as a Potential Indicator of Rotor Bar Breakage in the Induction Machine," *IEEE Trans. Ind. Electron.*, vol. 56, no. 11, pp. 4592–4605, Nov. 2009.

[14] M. F. Cabanas, F. Pedrayes, M. G. Melero, C. H. R. García, J. M. Cano, G. A. Orcajo, and J. G. Norniella, "Unambiguous Detection of Broken Bars in Asynchronous Motors by Means of a Flux Measurement-Based Procedure," *IEEE Trans. Instrum. Meas.*, vol. 60, no. 3, pp. 891–899, 2011.

[15] M. Drif and A. J. M. Cardoso, "Discriminating the Simultaneous Occurrence of Three-Phase Induction Motor Rotor Faults and Mechanical Load Oscillations by the Instantaneous Active and Reactive Power Media Signature Analyses," *IEEE Trans. Ind. Electron.*, vol. 59, no. 3, pp. 1630–1639, Mar. 2012.

[16] A. M. da Silva, R. J. Povinelli, and N. A. O. Demerdash, "Rotor Bar Fault Monitoring Method Based on Analysis of Air-Gap Torques of Induction Motors." *IEEE Trans. Ind. Informat.*, vol. 9, no. 4, pp. 2274–2283, 2013.

[17] S. H. Kia, H. Henao, and G.-A. Capolino, "A High-Resolution Frequency Estimation Method for Three-Phase Induction Machine Fault Detection," *IEEE Trans. Ind. Electron.*, vol. 54, no. 4, pp. 2305–2314, Aug. 2007.

[18] E. Radoi and A. Quinquis, "A New Method for Estimating the Number of Harmonic Components in Noise with Application in High Resolution Radar," *EURASIP, J. Appl. Signal Process.*, pp. 1177–1188, Jul. 2004.

[19] E. A. Hoyer and R. F. Stork, "The Zoom FFT using Complex Modulation," in *Acoustics, Speech, and Signal Processing, IEEE International Conference on ICASSP'77.*, vol. 2. IEEE, 1977, pp. 78–81.

[20] A. Lebaroud and G. Clerc, "Classification of Induction Machine Faults by Optimal Time Frequency Representations," *IEEE Trans. Ind. Electron.*, vol. 55, no. 12, pp. 4290–4298, 2008.

[21] A. M. da Silva, R. J. Povinelli, and N. A. O. Demerdash, "Induction Machine Broken Bar and Stator Short-Circuit Fault Diagnostics Based on Three-Phase Stator Current Envelopes," *IEEE Trans. Ind. Electron.*, vol. 55, no. 3, pp. 1310–1318, 2008.

[22] A. Bellini, F. Filippetti, G. Franceschini, C. Tassoni, and G. B. Kliman, "Quantitative Evaluation of Induction Motor Broken Bars by Means of Electrical Signature Analysis," *IEEE Trans. Ind. Appl.*, vol. 37, no. 5, pp. 1248–1255, Oct. 2001.

[23] B. Xu, L. Sun, L. Xu, and G. Xu, "An ESPRIT-SAA-Based Detection Method for Broken Rotor Bar Fault in Induction Motors," *IEEE Trans. Energy Convers.*, vol. 27, no. 3, pp. 654–660, 2012.

[24] J. A. Antonino-daviu, M. Riera-guasp, J. Pons-llinares, J. Park, S. B. Lee, J. Yoo, and C. Kral, "Detection of Broken Outer-Cage Bars for Double-Cage Induction Motors Under the Startup Transient," *IEEE Trans. Ind. Appl.*, vol. 48, no. 5, pp. 1539–1548, 2012.

[25] Y.-H. Kim, Y.-W. Youn, D.-H. Hwang, J.-H. Sun, and D.-S. Kang, "High-Resolution Parameter Estimation Method to Identify Broken Rotor Bar Faults in Induction Motors," *IEEE Trans. Ind. Electron.*, vol. 60, no. 9, pp. 4103–4117, Sep. 2013.

[26] P. Stoica, H. Li, and J. Li, "Amplitude Estimation of Sinusoidal Signals : Survey , New Results , and an Application," *IEEE Trans. Signal Process.*, vol. 48, no. 2, pp. 338–352, 2000.

[27] R. Puche-Panadero, M. Pineda-Sanchez, M. Riera-guasp, J. Roger-Folch, E. Hurtado-Perez, and J. Perez-Cruz, "Improved Resolution of the MCSA Method Via Hilbert Transform , Enabling the Diagnosis of Rotor Asymmetries at Very Low Slip," *IEEE Trans. Energy Convers.*, vol. 24, no. 1, pp. 52–59, 2009.

[28] B. Xu, L. Sun, L. Xu, and G. Xu, "Improvement of the Hilbert Method via ESPRIT for Detecting Rotor Fault in Induction Motors at Low Slip," *IEEE Trans. Energy Convers.*, vol. 28, no. 1, pp. 225–233, 2013.

[29] M. Y. Kaikaa and M. Hadjami, "Effects of the Simultaneous Presence of Static Eccentricity and Broken Rotor Bars on the Stator Current of Induction Machine," *IEEE Trans. Ind. Electron.*, vol. 61, no. 5, pp. 2452–2463, 2014.

[30] K. Boughrara, N. Takorabet, R. Ibtiouen, O. Touhami, and F. Dubas, "Analytical Analysis of Cage Rotor Induction Motors in Healthy, Defective and Broken Bars Conditions," *IEEE Trans. Magn.*, vol. 02, no. c, pp. 1–1, 2014.

[31] J. Pons-Llinares, J. A. Antonino-daviu, M. Riera-guasp, S. B. Lee, T.-J. Kang, and C. Yang, "Advanced Induction Motor Rotor Fault Diagnosis via Continuous and Discrete Time-Frequency Tools," *IEEE Trans. Ind. Electron.*, vol. 0046, no. c, p. 1, 2014.

[32] J. Faiz, V. Ghorbanian, and B. M. Ebrahimi, "EMD-Based Analysis of Industrial Induction Motors With Broken Rotor Bars for Identification of Operating Point at Different Supply Modes," *IEEE Trans. Ind. Informat.*, vol. 10, no. 2, pp. 957–966, 2014.

[33] K. N. Gyftakis and J. C. Kappatou, "A Novel and Effective Method of Static Eccentricity Diagnosis in Three-Phase PSH Induction Motors," *IEEE Trans. Energy Conv.*, vol. 28, no. 2, pp. 405–412, 2013.

[34] X. Huang, T. G. Habetler, R. G. Harley, and E. J. Wiedenbrug, "Using a Surge Tester to Detect Rotor Eccentricity Faults in Induction Motors," *IEEE Trans. Ind. Appl.*, vol. 43, no. 5, pp. 1183–1190, 2007.

[35] R. R. Schoen and T. G. Habetler, "Effects of Time-Varying Loads on Rotor Fault Detection in Induction Machines," *IEEE Trans. Ind. Appl.*, vol. 31, no. 4, pp. 900–906, 1995.

[36] M. Blödt, J. Regnier, and J. Faucher, "Distinguishing Load Torque Oscillations and Eccentricity Faults in Induction Motors Using Stator Current Wigner Distributions," *IEEE Trans. Ind. Appl.*, vol. 45, no. 6, pp. 1991–2000, 2009.

[37] S. Nandi, S. Ahmed, and H. A. Toliyat, "Detection of Rotor Slot and other Eccentricity Related Harmonics in a Three Phase Induction Motor with Different Rotor Cages," *IEEE Trans. Energy Convers.*, vol. 16, no. 3, pp. 253–260, 2001.

[38] Z. Ye, B. Wu, and A. Sadeghian, "Current Signature Analysis of Induction Motor Mechanical Faults by Wavelet Packet Decomposition," *IEEE Trans. Ind. Electron.*, vol. 50, no. 6, pp. 1217–1228, 2003.

[39] M. Riera-Guasp, M. Pineda-Sanchez, J. Perez-Cruz, R. Puche-Panadero, J. Roger-Folch, and J. A. Antonino-Daviu, "Diagnosis of Induction Motor Faults via Gabor Analysis of the Current in Transient Regime," *IEEE Trans. Instrum. Meas.*, vol. 61, no. 6, pp. 1583–1596, 2012.

[40] Z. Liu, X. Yin, Z. Zhang, D. Chen, and W. Chen, "Online Rotor Mixed Fault Diagnosis Way Based on Spectrum Analysis of Instantaneous Power in Squirrel Cage Induction Motors," *IEEE Trans. Energy Convers.*, vol. 19, no. 3, pp. 485–490, 2004.

[41] J. Faiz and M. Ojaghi, "Instantaneous-Power Harmonics as Indexes for Mixed Eccentricity Fault in Mains-Fed and Open/Closed-Loop Drive-Connected Squirrel-Cage Induction Motors," *IEEE Trans. Ind. Electron.*, vol. 56, no. 11, pp. 4718–4726, 2009.

[42] M. Drif and A. J. M. Cardoso, "Airgap-Eccentricity Fault Diagnosis , in Three-Phase Induction Motors , by the Complex Apparent Power Signature Analysis," *IEEE Trans. Ind. Electron.*, vol. 55, no. 3, pp. 1404–1410, 2008.

[43] A. M. Knight and S. P. Bertani, "Mechanical Fault Detection in a Medium-Sized Induction Motor Using Stator Current Monitoring," *IEEE Trans. Energy Convers.*, vol. 20, no. 4, pp. 753–760, 2005.

[44] S. Nandi, T. C. Ilamparithi, S. B. Lee, and D. Hyun, "Detection of Eccentricity Faults in Induction Machines Based on Nameplate Parameters," *IEEE Trans. Ind. Electron.*, vol. 58, no. 5, pp. 1673–1683, 2011.

[45] D. Hyun, J. Hong, S. B. Lee, K. Kim, E. J. Wiedenbrug, M. Teska, and S. Nandi, "Automated Monitoring of Airgap Eccentricity for Inverter-Fed Induction Motors Under Standstill Conditions," *IEEE Trans. Ind. Appl.*, vol. 47, no. 3, pp. 1257–1266, 2011.

[46] I. P. Georgakopoulos, E. D. Mitronikas, and A. N. Safacas, "Detection of Induction Motor Faults in Inverter Drives Using Inverter Input Current Analysis," *IEEE Trans. Ind. Electron.*, vol. 58, no. 9, pp. 4365–4373, 2011.

[47] V. N. Ghate and S. V. Dudul, "Cascade Neural-Network-Based Fault Classifier for Three-Phase Induction Motor," *IEEE Trans. Ind. Electron.*, vol. 58, no. 5, pp. 1555–1563, May 2011.

[48] M. Seera, C. P. Lim, D. Ishak, and H. Singh, "Fault Detection and Diagnosis of Induction Motors Using Motor Current Signature Analysis and a Hybrid FMM CART Model," *IEEE Trans. Neural Networks Learn. Syst.*, vol. 23, no. 1, pp. 97–108, 2012.

[49] S. Choi, B. Akin, M. M. Rahimian, and H. A. Toliyat, "Implementation of a Fault-Diagnosis Algorithm for Induction Machines Based on Advanced," *IEEE Transaction on Industrial electronics.*, vol. 58, no. 3, pp. 937–948, 2011.

[50] C. Concari, G. Franceschini, and C. Tassoni, "Toward Practical Quantification of Induction Drive Mixed Eccentricity," *IEEE Trans. Ind. Appl.*, vol. 47, no. 3, pp. 1232–1239, 2011.

[51] A. Ceban, R. Pusca, and R. Romary, "Study of Rotor Faults in Induction Motors Using External Magnetic Field Analysis," *IEEE Transactions on Industrial Electronics*, vol. 59, no. 5, pp. 2082–2093, May 2012.

[52] R. N. Andriamalala, H. Razik, L. Baghli, and F.-m. Sargos, "Eccentricity Fault Diagnosis of a Dual-Stator Winding Induction Machine Drive Considering the Slotting Effects," *IEEE Trans. Ind. Electron.*, vol. 55, no. 12, pp. 4238–4251, 2008.

[53] J. Faiz, B. M. Ebrahimi, B. Akin, and H. A. Toliyat, "Finite-Element Transient Analysis of Induction Motors Under Mixed Eccentricity Fault," *IEEE Trans. Magn.*, vol. 44, no. 1, pp. 66–74, 2008.

[54] ——, "Motors using Finite Element Method," *IEEE Trans. Magn.*, vol. 45, no. 3, pp. 1764–1767, 2009.

[55] J. Faiz and M. Ojaghi, "Stator Inductance Fluctuation of Induction Motor as an Eccentricity Fault Index," *IEEE Transactions on Magnetics*, vol. 47, no. 6, pp. 1775–1785, Jun. 2011.

[56] D. G. Dorrell, "Sources and Characteristics of Unbalanced Magnetic Pull in Three-Phase Cage Induction Motors With Axial-Varying Rotor Eccentricity," *IEEE Trans. Ind. Appl.*, vol. 47, no. 1, pp. 12–24, 2011.

[57] D.-J. Kim, H.-J. Kim, J.-P. Hong, and C.-J. Park, "Estimation of Acoustic Noise and Vibration in an Induction Machine Considering Rotor Eccentricity," *IEEE Trans. Magn.*, vol. 50, no. 2, pp. 857–860, Feb. 2014.

[58] J. Seshadrinath, B. Singh, and B. K. Panigrahi, "Investigation of Vibration Signatures for Multiple Fault Diagnosis in Variable Frequency Drives Using Complex Wavelets," *IEEE Trans. Power Electron.*, vol. 29, no. 2, pp. 936–945, Feb. 2014.

[59] V. Climente-Alarcon, J. Antonino-Daviu, F. Vedreno-Santos, and R. Puche-Panadero, "Vibration transient detection of broken rotor bars by psh sidebands," *Industry Applications, IEEE Transactions on*, vol. 49, no. 6, pp. 2576–2582, Nov 2013.

[60] Y. Gritli, A. Di Tommaso, F. Filippetti, R. Miceli, C. Rossi, and A. Chatti, "Investigation of motor current signature and vibration analysis for diagnosing rotor broken bars in double cage induction motors," in *Power Electronics, Electrical Drives, Automation and Motion (SPEEDAM), 2012 International Symposium on*. IEEE, 2012, pp. 1360–1365.

[61] S. Chang and R. Yacamini, "Experimental study of the vibrational behaviour of machine stators," in *Electric Power Applications, IEE Proceedings-*, vol. 143, no. 3. IET, 1996, pp. 242–250.

[62] S. Verma, R. Singal, and K. Williams, "Vibration behaviour of stators of electrical machines, part i: Theoretical study," *Journal of sound and vibration*, vol. 115, no. 1, pp. 1–12, 1987.

[63] R. Singal, K. Williams, and S. Verma, "Vibration behaviour of stators of electrical machines, part ii: experimental study," *Journal of sound and vibration*, vol. 115, no. 1, pp. 13–23, 1987.

[64] A. S. Raj and N. Murali, "Early classification of bearing faults using morphological operators and fuzzy inference," *Industrial Electronics, IEEE Transactions on*, vol. 60, no. 2, pp. 567–574, 2013.

[65] V. C. Leite, B. da Silva, J. Guedes, G. F. Cintra Veloso, L. E. Borges da Silva, G. Lambert-Torres, E. L. Bonaldi, and L. E. de Lacerda de Oliveira, "Detection of localized bearing faults in induction machines by spectral kurtosis and envelope analysis of stator current," *Industrial Electronics, IEEE Transactions on*, vol. 62, no. 3, pp. 1855–1865, 2015.

[66] M. Nemec, K. Drobnic, D. Nedeljkovic, F. Rastko, V. Ambrozic, R. Fiser, and V. Ambrozic, "Detection of Broken Bars in Induction Motor through the Analysis of Supply Voltage Modulation," *IEEE Trans. Ind. Electron.*, vol. 57, no. 8, pp. 2879–2888, 2010.

[67] S. M. A. Cruz, "An Active Reactive Power Method for the Diagnosis of Rotor Faults in Three-Phase Induction Motors Operating Under Time-Varying Load Conditions," *IEEE Transactions on Energy Conversion*, vol. 27, no. 1, pp. 71–84, 2012.

[68] X. Ying, "Performance evaluation and thermal fields analysis of induction motor with broken rotor bars located at different relative positions," *Magnetics, IEEE Transactions on*, vol. 46, no. 5, pp. 1243–1250, 2010.

[69] M. J. Picazo-Rodenas, R. Royo, J. A. Antonino-Daviu, and J. Roger-Folch, "Use of Infrared Thermography for Computation of Heating Curves and Preliminary Failure Detection in Induction Motors," *2012 XXth Int. Conf. Electr. Mach.*, pp. 525–531, Sep. 2012.

[70] L. Li, W. Fu, S. Ho, S. Niu, and Y. Li, "A quantitative comparison study of power-electronic-driven flux-modulated machines using magnetic field and thermal field co-simulation," *Industrial Electronics, IEEE Transactions on*, vol. 62, no. 10, pp. 6076–6084, 2015.

[71] B. Ayhan, M.-Y. Chow, and M.-H. Song, "Multiple Signature Processing-Based Fault Detection Schemes for Broken Rotor Bar in Induction Motors," *IEEE Trans. Energy Convers.*, vol. 20, no. 2, pp. 336–343, 2005.

[72] B. Ayhan, M.-y. Chow, and M.-h. Song, "Multiple Discriminant Analysis and Neural-Network-Based Monolith and Partition Fault-Detection Schemes for Broken Rotor Bar in Induction Motors," *IEEE Trans. Ind. Electron.*, vol. 53, no. 4, pp. 1298–1308, Aug. 2006.

[73] B. Ayhan, H. J. Trussell, M.-y. Chow, and M.-H. Song, "On the Use of a Lower Sampling Rate for Broken Rotor Bar Detection With DTFT and AR-Based Spectrum Methods," *IEEE Transaction on Industrial electronics.*, vol. 55, no. 3, pp. 1421–1434, 2008.

[74] A. Garcia-perez, R. D. J. Romero-troncoso, E. Cabal-yepez, and R. A. Osornio-rios, "The Application of High-Resolution Spectral Analysis for Identifying Multiple Combined Faults in Induction Motors," *IEEE Trans. Ind. Electron.*, vol. 58, no. 5, pp. 2002–2010, May 2011.

[75] M. Khan, T. S. Radwan, and M. A. Rahman, "Real-time implementation of wavelet packet transform-based diagnosis and protection of three-phase induction motors," *Energy Conversion, IEEE Transactions on*, vol. 22, no. 3, pp. 647–655, 2007.

[76] M. Pineda-Sanchez, J. Perez-Cruz, J. Roger-Folch, M. Riera-Guasp, A. Sapena-Bano, and R. Puche-Panadero, "Diagnosis of induction motor faults using a dsp and advanced demodulation techniques," in *Diagnostics for Electric Machines, Power Electronics and Drives (SDEMPED), 2013 9th IEEE International Symposium on*. IEEE, 2013, pp. 69–76.

[77] A. Ordaz-moreno, R. D. J. Romero-troncoso, J. A. Vite-frias, J. R. Rivera-gillen, and A. Garcia-perez, "Automatic Online Diagnosis Algorithm for Broken-Bar Detection on Induction Motors Based on Discrete Wavelet Transform for FPGA Implementation," *IEEE Trans. Ind. Electron.*, vol. 55, no. 5, pp. 2193–2202, 2008.

[78] J. Rangel-Magdaleno, R. Romero-Troncoso, R. A. Osornio-Rios, E. Cabal-Yepez, and L. M. Contreras-Medina, "Novel methodology for online half-broken-bar detection on induction motors," *Instrumentation and Measurement, IEEE Transactions on*, vol. 58, no. 5, pp. 1690–1698, 2009.

[79] R. D. J. Romero-troncoso, R. Saucedo-Gallaga, E. Cabal-Yepez, A. Garcia-Perez, R. A. Osornio-rios, R. Alvarez-Salas, H. Miranda-Vidales, and N. Huber, "FPGA-Based Online Detection of Multiple Combined Faults in Induction Motors Through Information Entropy and Fuzzy Inference," *IEEE Trans. Ind. Electron.*, vol. 58, no. 11, pp. 5263–5270, Nov. 2011.

[80] B. Halder and T. Kailath, "Efficient estimation of closely spaced sinusoidal frequencies using subspace-based methods," *Signal Processing Letters, IEEE*, vol. 4, no. 2, pp. 49–51, 1997.

[81] B. N. Datta, *Numerical Llinear Algebra and Applications*. Siam, 2010.

[82] M. H. Hayes, *Statistical Digital Signal Processing and Modeling*. John Wiley & Sons, 2010.

[83] Q. Zhang, "Probability of Resolution of the MUSIC Algorithm," *IEEE Trans. Signal Process.*, vol. 43, no. 4, pp. 978–987, Apr. 1995.

[84] A. V. Oppenheim, R. W. Schafer, J. R. Buck *et al.*, *Discrete-time Signal Processing*. Pearson Prentice Hall, 2011, vol. 2.

[85] H. A. Toliyat and T. A. Lipo, "Transient Analysis of Cage Induction Machines under Stator, Rotor Bar and End Ring Faults," *Energy Conversion, IEEE Transactions on*, vol. 10, no. 2, pp. 241–247, 1995.

[86] J. Faiz, I. T. Ardekanei, and H. A. Toliyat, "An Evaluation of Inductances of a Squirrel-Cage Induction Motor Under Mixed Eccentric Conditions," *IEEE Trans. Energy Convers.*, vol. 18, no. 2, pp. 252–258, 2003.

[87] J. Faiz and M. Ojaghi, "Unified winding function approach for dynamic simulation of different kinds of eccentricity faults in cage induction machines," *IET Electric Power Applications*, vol. 3, no. 5, p. 461, 2009.

[88] J. Faiz and I. Tabatabaei, "Extension of Winding Function Theory for Nonuniform Air Gap in Electric Machinery," *IEEE Trans. Magn.*, vol. 38, no. 6, pp. 3654–3657, 2002.

[89] A. Routray, A. K. Pradhan, and K. P. Rao, "A Novel Kalman Filter for Frequency Estimation of Distorted Signals in Power Systems," *IEEE Trans. Instrum. Meas.*, vol. 51, no. 3, pp. 469–479, Jun. 2002.

[90] D. Simon, *Optimal state estimation: Kalman, H infinity, and nonlinear approaches*. John Wiley & Sons, 2006.

[91] M. S. Zaky, M. M. Khater, S. S. Shokralla, and H. Yasin, "Wide-Speed-Range Estimation With Online Parameter Identification Schemes of Sensorless Induction Motor Drives," *IEEE Trans. Ind. Electron.*, vol. 56, no. 5, pp. 1699–1707, May 2009.

[92] L. Zhao, J. Huang, H. Liu, B. Li, and W. Kong, "Second-Order Sliding-Mode Observer with Online Parameter Identification for Sensorless Induction Motor Drives," *IEEE Trans. Ind. Informat.*, vol. 61, no. 10, pp. 5280–5289, 2014.

[93] O. Keysan and H. B. Ertan, "Real-time Speed and Position Estimation using Rotor Slot harmonics," *IEEE Trans. Ind. Informat.*, vol. 9, no. 2, pp. 899–908, 2013.

[94] Z. Gao, L. Turner, and R. S. Colby, "Application of Linear-phase Filters in Induction Motor Speed Detection," *IEEE Trans. Ind. Appl.*, vol. 50, no. 6, pp. 1314–1321, 2012.

[95] Z. Gao, L. Turner, R. S. Colby, and B. Leprettre, "A Frequency Demodulation Approach to Induction Motor Speed Detection," *IEEE Trans. Ind. Appl.*, vol. 47, no. 4, pp. 1632–1642, Jul. 2011.

List of Publication

1. A. K. Samanta, A. Naha, D. Basu, A. Routray, and A. K. Deb, "Online Condition Monitoring of Traction Motor," Book chapter in *Handbook of Research on Emerging Innovations in Rail Transportation Engineering*, IGI Global. (accepted)

2. A. Naha, A. K. Samanta, A. Routray, and A. K. Deb, "Determining Autocorrelation Matrix Size and Sampling Frequency for MUSIC Algorithm," *IEEE Signal Process. Lett.*, vol. 22, no. 8, pp. 1016-1020, Aug. 2015.

3. A. Mukherjee, A. Routray, and A. K. Samanta, "Method for On-line Detection of Arcing in Low Voltage Distribution Systems," *IEEE Trans. Power Deliv.*, vol. PP, no. 99, pp. 11, 2015.

4. A. K. Samanta, A. Naha, A. Routray, and A. K. Deb, "A Fast and Accurate Spectral Estimator for Online Detection of Partial Broken Bar in Induction Motors," *IEEE Trans. Ind. Electron.* (Under review)

Author Biography

Anik Kumar Samanta is M.S. (by research) from Advanced Technology Development Centre, Indian Institute of Technology, Kharagpur. He completed his B.Tech. degree in Electronics & Communication Engineering from Dr. B. C. Roy Engg. College, Durgapur. He is also associated with the Center for Railway Research for designing diagnostics of induction motors for the Indian Railways. His research interests include high-resolution spectral estimation, signal based fault diagnosis of induction motors, and real-time and embedded signal processing.